

**Contract No. DTFAC-15-D-00007.
Delivery Order 005 NAPTF Support
Deliverable 4.9.2.5: CC8 Phase 3 Joint Comparison
Traffic Test Report**

Submitted on May 30, 2019

Resubmitted March 17, 2020

Prepared by Dr. Carlos Cary, Dr. Mesbah Ahmed, and Dr. Hao Yin, Horizon Engineering Consulting LLC.

Submitted by General Dynamics Information Technology

GENERAL DYNAMICS
Information Technology

TABLE OF CONTENTS

	Page
1. INTRODUCTION	1
1.1 OBJECTIVE	1
2. DESIGN AND CONSTRUCTION OF TEST SECTION	1
2.1 DESCRIPTION OF TEST SECTION	1
2.2 CONSTRUCTION	5
2.2.1 SUBGRADE (P-152M) PREPARATION	5
2.2.2 SUBBASE (P-154M) CONSTRUCTION	6
2.2.3 LEAN CONCRETE (P-306MR) CONSTRUCTION	6
2.2.4 SURFACE CONCRETE (P-501MR) PAVING	6
2.3 INSTRUMENTATION	7
3. DESCRIPTION OF TESTING METHODS AND EQUIPMENT	10
3.1 TESTING EQUIPMENT	10
3.2 TEST DESCRIPTION	10
3.2.1 ESTIMATION OF INITIAL WHEEL LOAD	10
3.2.2 TEST PROCEDURE	13
3.2.3 MONITORING	19
4. FULL-SCALE TEST	20
4.1 STAGE I TEST	21
4.1.1 RAMP-UP RESPONSE TEST	21
4.1.2 STAGE I TRAFFIC TEST	21
4.2 STAGE II TEST	25
4.2.1 REVISED RAMP-UP RESPONSE TEST	25
4.2.2 STAGE II TRAFFIC TEST	32
5. BEHAVIOR OF TEST SECTION UNDER TRAFFIC	33
5.1 JOINT PERFORMANCE	33
5.1.1 INSTRUMENTATION DATA	33
5.1.2 HWD DEFLECTION	37
5.1.3 JOINT STIFFNESS	38

5.2 PAVEMENT PERFORMANCE	40
5.2.1 DISTRESS MAPPING	40
5.2.2 STRUCTURAL CONDITION INDEX (SCI)	41
5.2.3 CRACK DENSITY (CD)	50
6. PRELIMINARY DATA ANALYSIS	54
6.1 JOINT DETERIORATION	54
6.1.1 IN-PAVEMENT SENSOR DATA	54
6.1.2 HWD DEFLECTION DATA	69
6.2 Slab DETERIORATION	76
6.2.1 RIGID PAVEMENT DISTRESSES	76
6.2.2 DETERIORATION BASED ON HWD DEFLECTION	82
7. ADVANCED DATA ANALYSIS	95
7.1 FAILURE MECHANISM	95
7.2 DESIGN CONSIDERATIONS	101
7.2.1 PAVEMENT DETERIORATION VERSUS JOINT PERFORMANCE	101
7.2.2 JOINT PERFORMANCE INDICATORS	105
8. CONCLUSIONS AND RECOMMENDATIONS	113
8.1 CONCLUSIONS	113
8.1.1 PAVEMENT STRUCTURAL PERFORMANCE	113
8.1.2 RELATION BETWEEN PAVEMENT CONDITION AND JOINT PERFORMANCE	113
8.1.3 DESIGN CONSIDERATIONS	113
8.2 RECOMMENDATIONS	114
9. REFERENCES	114
Appendix A – Summary of Wander Pattern	
Appendix B – Contour of Joint Performance Indicators	
Appendix C – CC8 Phase III Joint Comparison Distress Maps	
Appendix D – CC8 Phase III Joint Comparison Distress Map Written Log	

LIST OF FIGURES

Figure	Page
1 Location Map of CC8 Joint Comparison Test Pavement. (The red hatched area is the overall CC8 test area.)	2
2 General Layout of CC8 Phase II – Joint Comparison Test Pavement	3
3 Slab Groups in CC8 Phase II – Joint Comparison Test Pavement	4
4 CC8 Phase 3 Joint Comparison Test Pavement Cross-Section	5
5 Instrumentation Layout, Plan View	8
6 Instrumentation Layout, Profile View	9
7 D Gear Configuration used in CC8 Phase II Joint Comparison Traffic Test	11
8 FAARFIELD Predictions: (a) 3D, (b) 2D, (c) D	13
9 Wander Pattern for Trafficking	14
10 HWD Test Locations	16
11 Seating Load Wander	17
12 Gear Tracks for Joint Evaluation	19
13 Stage I-Ramp-Up Response Test Results, North Test Item (02/28/2018)	22
14 Stage I-Ramp-Up Response Test Results, South Test Item (02/28/2018)	23
15 Tracks for the Stage II Ramp-Up Response Test	26
16 LT Sensitivity to Wheel Load for D Gear: (a) Transverse Joints, (b) Longitudinal Joint, North Side, (c) Longitudinal Joint, South Side	29
17 LTE Sensitivity to Wheel Load for D Gear: (a) Transverse Joints, (b) Longitudinal Joint, North Side, (c) Longitudinal Joint, South Side	30
18 LT Sensitivity to Wheel Load for 3D Gear: (a) Transverse Joints, (b) Longitudinal Joint, North Side, (c) Longitudinal Joint, South Side	31
19 LTE Sensitivity to Wheel Load for 3D Gear: (a) Transverse Joints, (b) Longitudinal Joint, North Side, (c) Longitudinal Joint, South Side	32
20 Sensor Pair Approach to Determine LT_{σ} and LTE_{σ}	34
21 Geometric Approach to Determine LT_{σ} and LTE_{σ}	35
22 LT_{σ} Levels at 396 Vehicle Passes (March 1, 2018)	36
23 HWD Test Schematic to Determine LTE_{δ}	37
24 LTE_{δ} Levels Prior to Traffic (After Seating Load)	38
25 Schematic of HWD Test for Joint Stiffness Calculation	39
26 Sample Distress Map (portion)	42
27 Sample Log (portion)	43
28 Joint Comparison SCI versus Passes Considering the North and South Sample Units	47
29 Joint Comparison SCI versus Passes Considering Four Sample Units	50
30 Example of Crack Density Calculation for Slab J10N (March 13, 2018)	51
31 Development of CD for Four Subgroups	54
32 LTE_{σ} of Transverse Doweled Joints N 2-3 and S 2-3 Calculated by Sensor Pair Method, and Instrumentation Data for Joint N 2-3: (a) LTE_{σ} of Transverse Doweled Joints N 2-3 and S 2-3, and (b) Strains used for Calculation of LTE_{σ} in Joint N 2-3	56
33 LTE_{σ} of Transverse Joints from Instrumentation Data: (a) Doweled (N 2-3 by Geometric Method and S 2-3 by Sensor Pair Method), and (b) Undoweled (Geometric Method)	58
34 Loaded and Unloaded Strains (EG-N-J-II-18) used to Determine LTE_{σ} in Joint N 4-5	59
35 Change in Slab Temperature	60

36 LT_{σ} of Transverse Joints from Instrumentation Data: (a) Doweled (N 2-3 by Geometric Method and S 2-3 by Sensor Pair Method), and (b) Undoweled (Geometric Method)	61
37 LTE_{σ} of Longitudinal Joints from Instrumentation Data Calculated by Sensor Pair Method: (a) Doweled, and (b) Keyway	63
38 Loaded and Unloaded Strains (Track L2) used to Determine LTE_{σ} of Longitudinal Joints on the North Side: (a) Joint N 2-8, (b) Joint N 5-11	65
39 Loaded and Unloaded Strains (Track L2) used to Determine LTE_{σ} of Longitudinal Joints on the South Side: (a) Joint S 4-10, (b) Joint S 5-11	66
40 LT_{σ} of Longitudinal Joints from Instrumentation Data Calculated by Sensor Pair Method: (a) Doweled, and (b) Keyway	68
41 Change in Deflection-Based LTE_{δ} for Transverse Joints: (a) NW - Doweled, (b) SW - Doweled, (c) NE - Undoweled, (d) SE - Undoweled	70
42 Correlation between LTE_{δ} and k_J for Transverse Joints: (a) North, (b) South	71
43 Correlation between LTE_{δ} and k_J for Transverse Joints: (a) NW - Doweled, (b) SW - Doweled, (c) NE - Undoweled, (d) SE - Undoweled	72
44 Change in Deflection-Based LTE_{δ} of Longitudinal Joints: (a) North-West: Doweled, (b) North-East: Doweled, (c) South-West: Keyway, (d) South-East: Keyway	73
45 Correlation between LTE_{δ} and k_J for Longitudinal Joints: (a) North, (b) South	74
46 Correlation between LTE_{δ} and k_J for Longitudinal Joints: (a) NW - Doweled, (b) NE - Doweled, (c) SW – Sinusoidal Keyed, (d) SE – Sinusoidal Keyed	75
47 Distresses Associated With Major SCI Changes in Slab Groups with Undoweled Contraction Joints: (a) NE, (b) SE	77
48 Distresses Associated With Major SCI Changes in Slab Groups with Doweled Contraction Joints: (a) NW, (b) SW	78
49 Distress Mapping at End of Stage I (D Gear at 65,000 lb. Wheel Load)	80
50 Distress Mapping at End of Stage II (3D Gear at 70,000 lb. Wheel Load)	81
51 Slab Center Deflection Basins, North-West Slab Group	83
52 Slab Center Deflection Basins, North-East Slab Group	84
53 Slab Center Deflection Basins, South-West Slab Group	85
54 Slab Center Deflection Basins, South-East Slab Group	86
55 Change in ISM Over the Course of Traffic: (a) North-West Slab Group,	87
56 Change in ISM Over the Course of Traffic: (a) South-West Slab Group,	88
57 Backcalculated Moduli of Pavement Layers as a Function of Traffic: (a) P-501MR Concrete, (b) P-306MR Base, (c) P-154M Subbase, (d) P-152M Subgrade	90
58 Corner-to-Center Deflection Ratios as a Function of Pass Number: (a) NW, (b) NE, (c) SW, (d) SE	92
59 Example of Void Detection in Corner 2NE of Slab J2N	93
60 Intercept Values for Slab Groups as a Function of Pass Number: (a) NW, (b) SW, (c) NE, (d) SE	94
61 Peak Surface Tensile Strain as a Function of Gear Track Number, Transverse Contraction Joint (March 1, 2018): (a) NW, (b) NE, (c) SW, (d) SE	96
62 Peak Surface Tensile Strain as a Function of Gear Track Number, Longitudinal Construction Joint (March 1, 2018): (a) NW, (b) NE, (c) SW, (d) SE	97
63 Maximum Surface Tensile Strain at Contraction Joints as a Function of Pass Number: (a) NW, (b) SW, (c) NE, (d) SE	99

64 Change in Surface Tensile Strain With Traffic along Construction Joints: (a) N 4-10, NE, (b) N 5-11, NE, (c) S 4-10, SE, (d) S 5-11, SE	100
65 ECS Deflections: (a) NW, (b) SW, (c) NE, (d) SE	101
66 SCI Versus Coverages (unadjusted)	102
67 SCI Versus Coverages (South Traffic Lane, Stage II Data Adjusted to Reference Conditions)	102
68 Comparison of Fatigue Life Among Slab Groups	104
69 Correlation between LTE_{δ} and LTE_{σ} : (a) Wadkar, 2010 (15), (b) CC8 Phase II Joint Comparison Data	106
70 Comparison between Measured and Predicted LTE_{δ} : (a) Contraction Joints Only,	108
71 Loaded and Unloaded Strains used to Determine LT_{σ} of Longitudinal Joint S 5-11	109
72 Stress-based LT_{σ} Predictive Models as Function of Joint Stiffness	110
73 Correlation between LT_{σ} and k_j : (a) Byrum et al., 2011 (5), (b) Proposed from CC8 Phase II Joint Comparison Test	111
74 Trends of LT_{σ} vs. k_j for four joint types: (a) Doweled contraction joint, (b) Undoweled contraction joint, (c) Doweled construction joint, (d) Sinusoidal keyed construction joint	112

LIST OF TABLES

Table	Page
1 Summary of Joint Type Combination	2
2 FAARFIELD Predictions	11
3 Stage I-Traffic Test History	24
4 Wander Pattern for Stage II Ramp-Up Response Test	26
5 Stage II Traffic Test History	33
6 Summary of Slab Modulus for LTE_{σ} and LT_{σ} Calculation	35
7 Structural Condition Index (SCI) Considering the North and South Sample Units	45
8 Structural Condition Index (SCI) Considering Four Sample Units	48
9 Crack Density for All Slabs (North)	52
10 Crack Density for All Slabs (South)	53
11 Calculation Approach for LTE_{σ} and LT_{σ} of Transverse and Longitudinal Joints	57
12 Pavement Structure and Material Properties Used for Backcalculation	89
13 Summary of Maximum Surface Tensile Strains during the First Wander Sequence	98
14 Summary of Fatigue Data for Four Slab Groups	103
15 Regression Constants for Equation 11, 12, and 13	109

LIST OF ACRONYMS

AC	Advisory Circular
ASTM	American Society for Testing Materials
BDF	Bridge Deck Finisher
CBR	California Bearing Ratio
CC2	Construction Cycle 2
CC6	Construction Cycle 6
CC8	Construction Cycle 8
CD	Crack Density
CDF	Cumulative Damage Factor
ECS	Eddy Current Sensors
EG	Embedded Strain Gauge
FAA	Federal Aviation Administration
FAARFIELD	FAA Rigid and Flexible Iterative Elastic Layered Design
FE	Finite Element
HWD	Heavy Weight Deflectometer
ID	Identification
IPRF	Innovative Pavement Research Foundation
ISM	Impact Stiffness Modulus
LT	Load Transfer
LTE	Load Transfer Efficiency
NAPTF	National Airport Pavement Test Facility
NAPTV	National Airport Pavement Test Vehicle
NDG	Nuclear Density Gauge
PCC	Portland Cement Concrete
PCI	Pavement Condition Index
P/C	Pass-to-Coverage
PSPA	Portable Seismic Properties Analyzer
PWL	Percent Within Limit
SCI	Structural Condition Index

1. INTRODUCTION

In Advisory Circular (AC) 150/5320-6F (1), pavement joints are categorized into three types: isolation (Types A, A-1), contraction (Types B, C, D), and construction (Types E, F) joints. Depending upon their design, the function of such joints is to control the stresses caused by expansion, contraction, and warping of the concrete.

Doweled joints, whether construction or contraction joints, depend primarily on the shear strength of the dowel and the bearing stress of the concrete to transfer the load. Their design is usually limited by the bearing strength of the concrete, which governs how loose the dowel becomes after repeated heavy loads. Doweled construction joints are currently the only type of construction joint allowed for airfield pavements with large aircraft operations. In general, the use of dowels play an important role in ensuring good load transfer particularly when the slab contracts at low temperatures and results in a loose joint. Undoweled contraction (dummy) joints depend on aggregate interlock for load transfer. Dummy joints are very sensitive to the crack width opening and tend to perform better with short joint spacings.

Although not required by the Federal Aviation Administration (FAA) standard (1), the use of dowels at all transverse contraction joints (Type C) has become a common practice in the construction of rigid airport pavements. However, there is a lack of evidence demonstrating the benefit of doweled over dummy contraction joints (Type D) in terms of fatigue life.

Previous AC 150/5320-6E (2) eliminated all keyed joints from the schedule of standard joint types due to a history of poor performance. Recently, European contractors have reported the successful application of the sine-wave shaped keyway having three or four smooth shaped waves with approximately 1-2 inches amplitude. This sinusoidal detail is intended to encourage better construction joint face interlock, compared to the rectangular key cross section previously common in the U.S. By eliminating hard corners, the sinusoidal keyway shape also reduces stress risers than cause breakage. However, full-scale test results showing similar performance of sine-wave shaped keyway construction joints were not available until now.

1.1 OBJECTIVE

The objective of Construction Cycle 8 (CC8) Phase 3 Joint Comparison experiment is twofold: a) compare the performance of standard doweled (Type E) to sine-wave shaped keyway longitudinal construction joint and assess the benefits, if any, of one type over the other; b) compare the performance of doweled (Type C) to dummy (Type D) transverse contraction joint and evaluate the benefits, if any, of doweling.

2. DESIGN AND CONSTRUCTION OF TEST SECTION

2.1 DESCRIPTION OF TEST SECTION

The CC8 Joint Comparison test area consists of a 90-foot length of jointed rigid pavement. The test area limits are stations 4+00 and 4+90, as shown in Figure 1. The width of test pavement extends from -30 ft. (north side) to +30 ft. (south side), with an additional 3 ft. of P-154M subbase shoulder on each side. Figure 2 shows the plan view of the test pavement. There are a total of

twenty-four 15×15 ft. slabs, twelve on the north and twelve on the south. These slabs are divided into four distinct groups as indicated by the blue dashed lines in Figure 3. Each group represents a particular combination of longitudinal and transverse joint types, as listed in Table 1. The north side longitudinal joints are Type E with 1-inch diameter dowels at -15 ft. and 0 ft. offsets (along the test pavement centerline). The south side longitudinal joint at offset +15 ft. is the sine-wave shaped keyway joint. The transverse Type C joints were constructed with 1-inch diameter dowels at stations 4+00, 4+15, 4+30, and 4+90. Dummy contraction joints (Type D) were used at stations 4+45, 4+60, and 4+75. Compression seals were used for all joints.

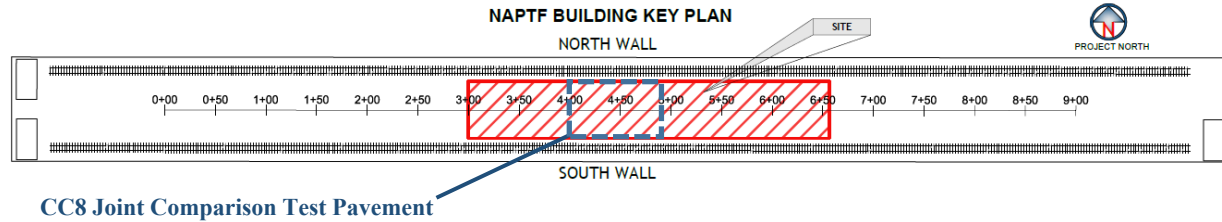


Figure 1. Location Map of CC8 Joint Comparison Test Pavement. (The red hatched area is the overall CC8 test area.)

Table 1. Summary of Joint Type Combination

Slab Group	Joint Type	
	Transverse	Longitudinal
North-West	Contraction Doweled Type C	Construction Doweled Type E
North-East	Contraction Dummy Type D	Construction Doweled Type E
South-West	Contraction Doweled Type C	Construction sine-wave shaped keyway
South-East	Contraction Dummy Type D	Construction sine-wave shaped keyway

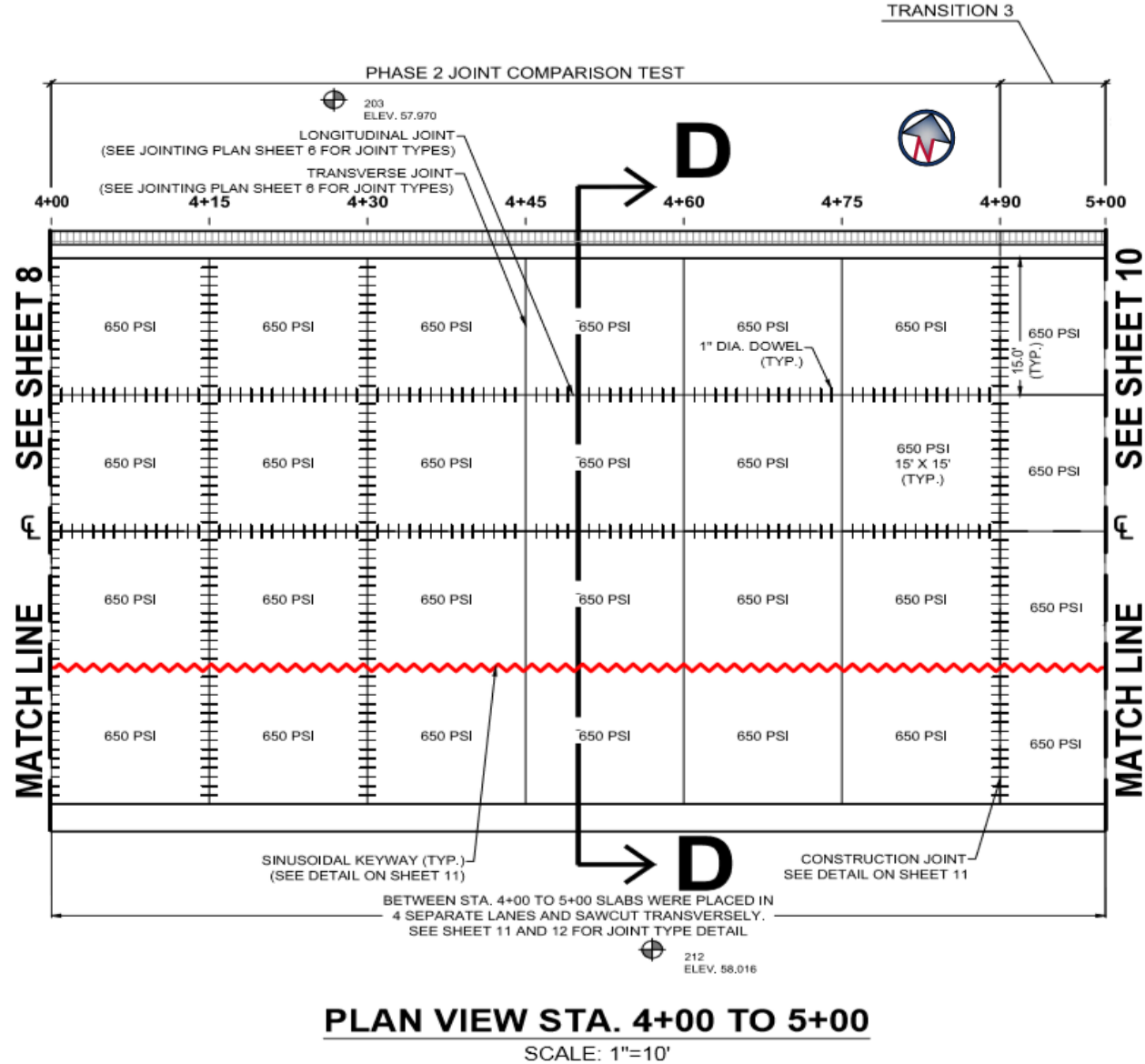
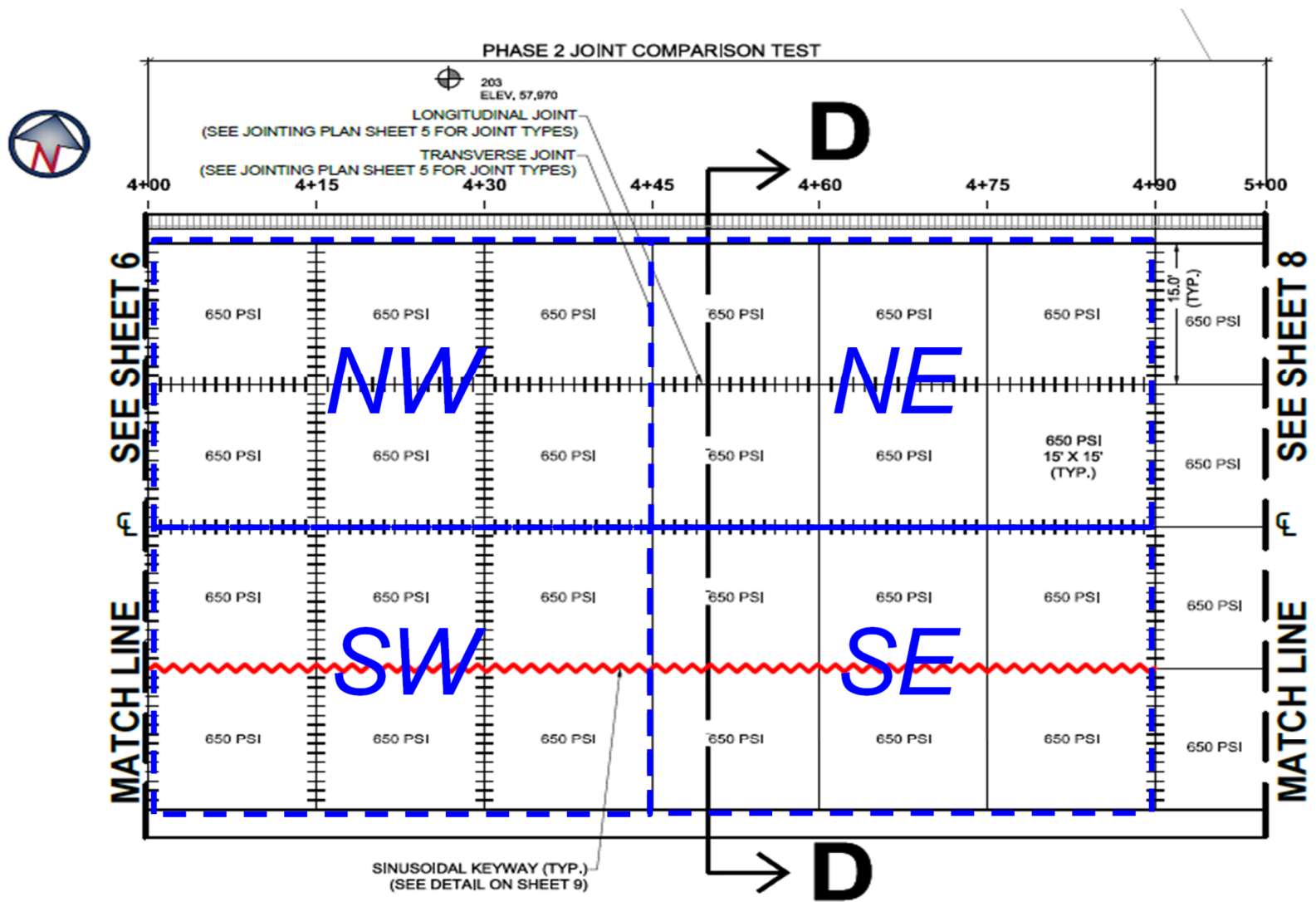


Figure 2. General Layout of CC8 Phase II – Joint Comparison Test Pavement



NW=North-West, NE=North-East, SW=South-West and SE=South-East

Figure 3. Slab Groups in CC8 Phase II – Joint Comparison Test Pavement

2.2 CONSTRUCTION

Figure 4 illustrates the pavement cross-section, consisting of 12 inches P-501MR PCC on 6 inches P-306MR lean concrete base course on 14 inches P-154M granular subbase. The structure is supported on a prepared P-152M clay subgrade with CBR 7-8. A general overview of the construction of the CC8 Joint Comparison test pavement is provided in sub-sections 2.2.1 – 2.2.4.

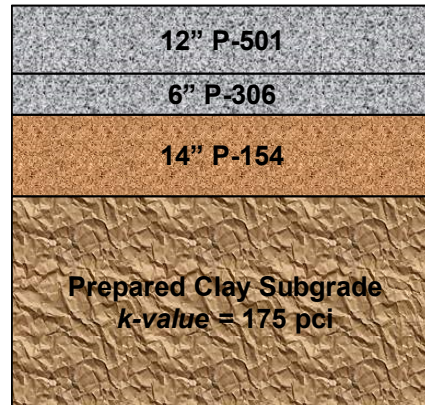


Figure 4. CC8 Phase 3 Joint Comparison Test Pavement Cross-Section

2.2.1 SUBGRADE (P-152M) PREPARATION

The subgrade target CBR range was 7-8 (± 0.5). Following demolition of the Construction Cycle 6 (CC6) pavement, the existing subgrade was tested to see if additional removal of existing DuPont clay was necessary. The procedure included trimming to final grade, tilling to a minimum depth of 8 inches, monitoring and adjusting the moisture content until the target CBR value was achieved. Conditioning of P-152M materials began on December 29, 2016 and was accepted on March 7, 2017.

To achieve the target moisture content, in-situ P-152M was processed regularly using a BOMAG MPH-364 soil stabilizer and Seamax travel mixer, and tested for moisture. Whenever subgrade moisture loss was required, commercial fans were used to circulate airflow across the processed material surface. When additional moisture was required, the material was watered using the National Airport Test Facility's (NAPTF) Bridge Deck Finisher (BDF) with a spray bar attachment. Water was allowed to permeate the subgrade for a minimum of 2 hours before reprocessing. Once a uniform moisture content was achieved, the subgrade was compacted for acceptance testing using earth rollers.

Between stations 4+00 and 4+45, the final CBR subgrade value was 7.6 both north and south of centerline. Between stations 4+45 and 4+90, the final CBR subgrade values were 7.6 (north of centerline) and 7.4 (south of centerline). Plate load tests indicated that the k -value was 154 pci north of centerline and 197 pci south of centerline, for an average k -value of 175 pci.

2.2.2 SUBBASE (P-154M) CONSTRUCTION

The 14-inch P-154M subbase layer was placed in two lifts. Past NAPTF experience suggested a target moisture content lower than optimum (7.6%) to prevent potential drain-down of water into the subgrade. Therefore, a target moisture content of 7% was selected. The spray bar attachment on the BDF was used to add water to the material as needed for moisture control. The first lift was placed on March 7, 2017 and accepted on March 13. The second lift was then placed on March 13 and accepted on March 30. The thicknesses of the first (bottom) and second (top) lift were 8 and 6 inches, respectively.

After placement and conditioning to the target moisture content, the material was compacted to final density. The compaction effort was monitored using a nuclear density gauge (NDG). Compaction continued until little to no change was observed with the NDG results. The final surface lift for each P-154M section was slightly overbuilt and trimmed to achieve the design elevation.

Acceptance and material testing of the P-154M material followed compaction. Between stations 4+00 and 4+45, the sand cone compaction values were 98% (north of centerline) and 96.7% (south of centerline) of the maximum dry density. Between stations 4+45 and 4+90, the sand cone compaction values were 101% (north) and 99.8% (south) of the maximum dry density. The average moisture content between stations 4+00 and 4+45 was 5.3%, and the average moisture content between stations 4+45 and 4+90 was 6.7%. Plate load tests were performed on the top of the subbase layer. The average *k*-values from plate load tests were 154 pci (north) 197 pci (south).

2.2.3 LEAN CONCRETE (P-306MR) CONSTRUCTION

Formwork for the lean concrete base (P-306MR) was completed prior to material placement. Lean concrete was placed in two lanes on two separate days: March 31, 2017 (south side) and April 6, 2017 (north side). Material acceptance testing and characterization were completed on-site by Craig Testing Laboratories, Inc. and the NAPTF NextGen Pavement Materials Laboratory. Common masonry hand tools and a vibratory screed were used by the contractor to complete the P-306MR placement, and instrumentation was monitored and protected during the placement. The surface was floated finish with a smooth trowel. The contractor covered the test area and samples after each placement with burlap and a poly sheet product for curing. The P-306MR laydown was accepted on April 13, 2017. Kerf cuts of 1 and 3 inches in width were made on the P-306MR surface on April 14, 2017. The depth of all kerf cuts was not greater than 1 inch. Instrumentation kerf cut diagrams are available in Construction Cycle 8 As-Built Drawings.

2.2.4 SURFACE CONCRETE (P-501MR) PAVING

Formwork and instrumentation for the concrete surface (P-501MR) were completed prior to material placement. Concrete slabs were placed in 4 lanes. From north to south, lanes 1 and 3 were placed on April 27, 2017 while lanes 2 and 4 were placed on May 2, 2017. Material acceptance testing and characterization were completed onsite by Craig Testing Laboratories, Inc. and the NAPTF NextGen Pavement Materials Laboratory.

The P-501MR material was placed following P-501MR specifications for Construction Cycle 8. However, the contractor was exceptionally permitted not to water the P-306MR layer prior to P-501MR placement. This restriction stemmed from the use of rosin paper as a bond breaker, causing concern that the rosin paper would deteriorate due to watering.

The contractor used common masonry hand tools and a vibratory screed to complete the P-501MR placement. The instrumentation was monitored and protected during this process. The surface was float finished with a smooth trowel. After each placement, the contractor covered the test area and samples with burlap and a polyethylene sheet product for curing. Within 24 hours of placement, the contractor made saw cuts using a Husqvarna Soft-Cut saw. Green cuts to 1½ inches deep were made in the surface, followed by a secondary cut to 3 inches deep. The P-501MR section was accepted after the 28-day flexural strength breaks on May 30, 2017.

2.3 INSTRUMENTATION

Gages were selected for reliability, accuracy, and ease of handling at the construction site. Gage locations are shown in the plan and profile views in Figure 5 and 6 respectively. Figure 6 includes the instrument key for both figures.

The naming convention for the sensors coded information on the sensor type, pavement side, test name, construction phase, and sequential ID. For example; EG-N-J-II-9 refers to an Embedded Strain Gage (EG) installed in the North side (N) of the Joint Comparison Test (J), construction phase II, gage number 9 in sequence. (Construction Phase II was distinct from CC8 Test Phase 3, i.e., the Joint Comparison Test.)

In eight slabs, the vertical movement of the concrete surface (P-501MR) relative to the top surface of the lean concrete base (P-306MR) was monitored by Eddy Current Sensors (ECS) installed at the slab corner. The ECSs are intended to operate both in static mode (to monitor the long-term upward movement of slab corners) and in dynamic mode (to record transient responses to vehicle loads).

Pairs of embedded strain gages (EG) were installed along longitudinal and transverse edges of 16 slabs to measure strain responses near the top (odd numbered gages) and bottom (even numbered gages) of the instrumented slabs. These gages were located along longitudinal and transverse joints in the trafficked area. In the P-501MR layer, a total of 46 EGs were installed prior to paving. Rebar chairs were used to ensure the center of the gauge was set at the proper height, 1 inch above the bottom and 1 inch below the surface.

Thermocouple trees were installed in both the north and south side of the pavement in one slab to monitor temperature gradients. Each tree consists of three thermocouples to measure the temperature at the bottom, middle, and top of the slab. In addition, moisture sensors were driven into the top of subgrade at four locations to monitor changes in moisture content.

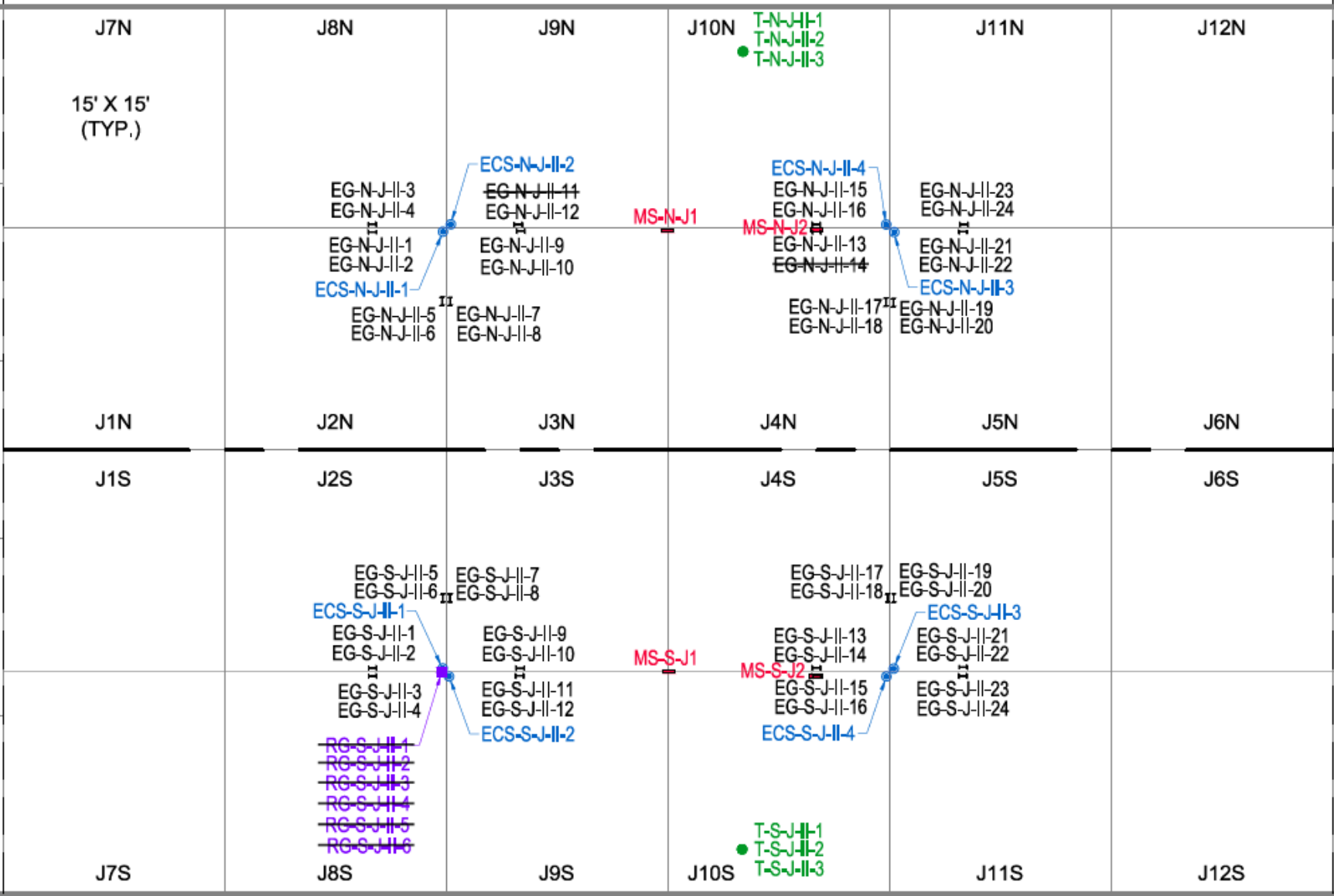
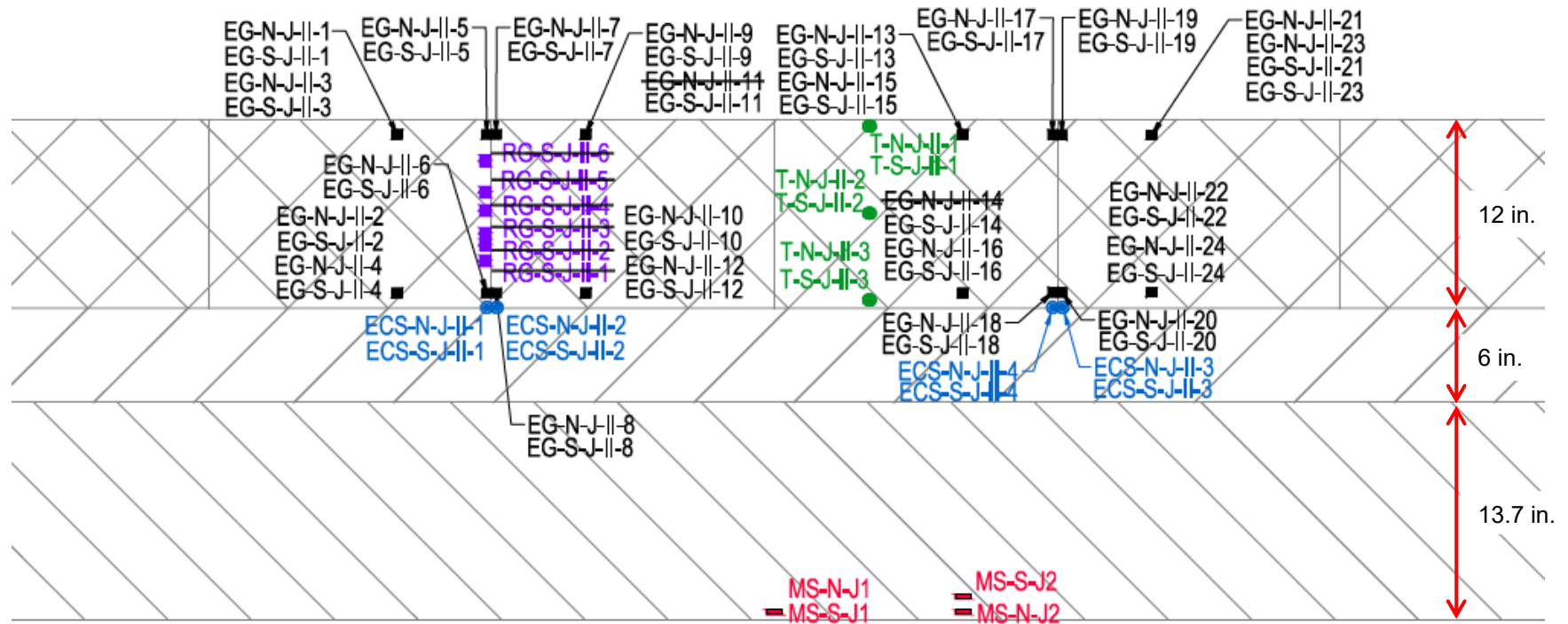


Figure 5. Instrumentation Layout, Plan View



INSTRUMENT KEY		
EG	EG	EMBEDDED STRAIN GAUGE
T	T	THERMOCOUPLE
MS	MS	MOISTURE SENSOR
ECS	ECS	EDDY CURRENT SENSOR
RG	RG	RESISTANCE GAGE

Figure 6. Instrumentation Layout, Profile View

3. DESCRIPTION OF TESTING METHODS AND EQUIPMENT

3.1 TESTING EQUIPMENT

The National Airport Pavement Test Vehicle (NAPTV) can be programmed for controlled aircraft wander simulation and can operate in manual or fully automatic modes. In this study, the vehicle speed was limited to 2.5 mph. The test vehicle is comprised of two carriages that can accommodate up to five load modules spaced 57 inches apart in tandem. Each load module has two wheels with a dual spacing of 54 inches. This allows for configurations of up to 20 wheels with loads up to 75,000 pounds per wheel. In this study, a 2-wheel gear configuration (D) was used on both north and south carriages for the initial full-scale traffic test (Figure 7). The NAPTV simulates aircraft wander by varying the lateral position of the carriages to approximate a normal distribution of aircraft traffic. The wander pattern used for this study consisted of 66 vehicle passes, arranged in 9 discrete tracks (or wander positions).

3.2 TEST DESCRIPTION

3.2.1 ESTIMATION OF INITIAL WHEEL LOAD

The FAA computer program FAARFIELD 1.42 was used to determine stresses under vehicle loads and estimate failure passes. The same pavement structure was used for both north and south test pavements. The following conditions were assumed:

- As-built pavement structure (Figure 4)
- Three gear configurations: 2-wheel gear (D), 4-wheel gear (2D), and 6-wheel gear (3D)
- Range of wheel loads: 47,500 - 67,500 pounds
- Subgrade $k = 175$ pci (average of north and south, Figure 4)
- $R = 710$ psi (average 270-day field-cured beam strength)

Table 2 shows a summary of FAARFIELD predictions at various wheel loads. The computed stress ratios (σ/R) ranged from 0.7 to 0.9. FAARFIELD computes two values of maximum slab stress: the edge stress, assuming the gear positioned at the joint; and the interior stress, assuming the gear positioned at the slab center. Stresses and calculated number of passes to failure are plotted in Figure 8(a), 8(b) and 8(c) for 3D, 2D, and D gears, respectively. The number of passes to failure from FAARFIELD was based on the larger of: (a) 75 percent of the maximum free edge stress, or (b) 95 percent of the maximum interior stress.

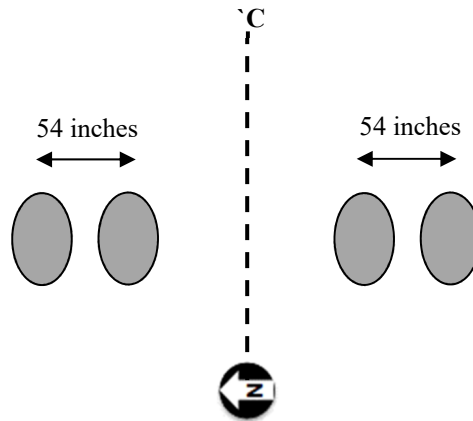
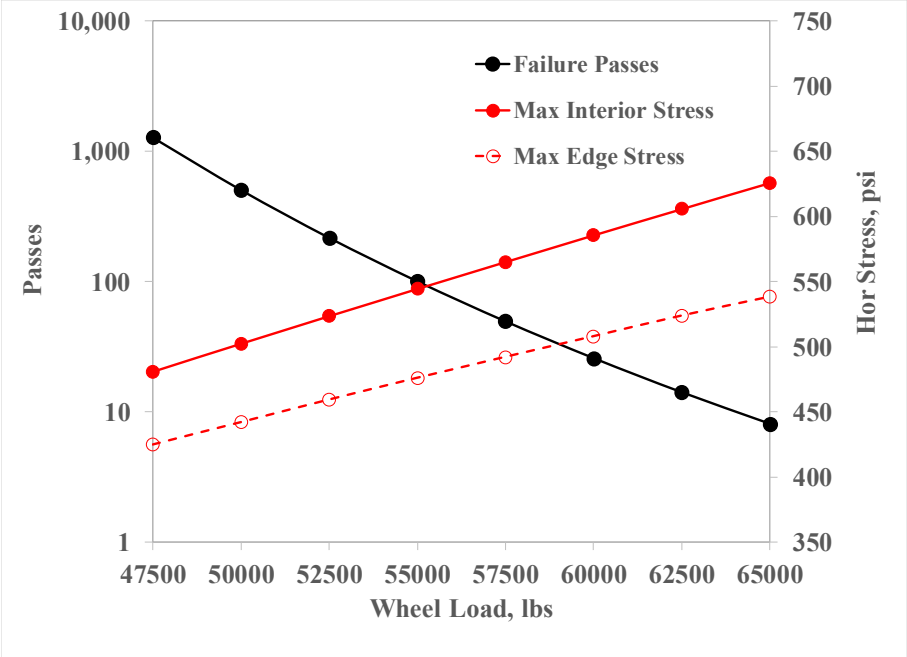


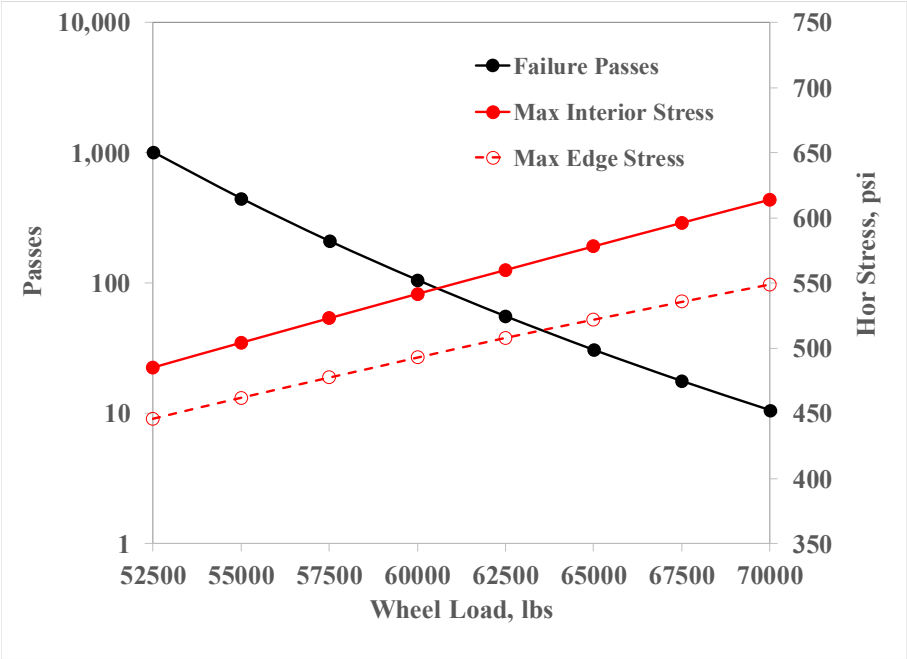
Figure 7. D Gear Configuration used in CC8 Phase II Joint Comparison Traffic Test

Table 2. FAARFIELD Predictions

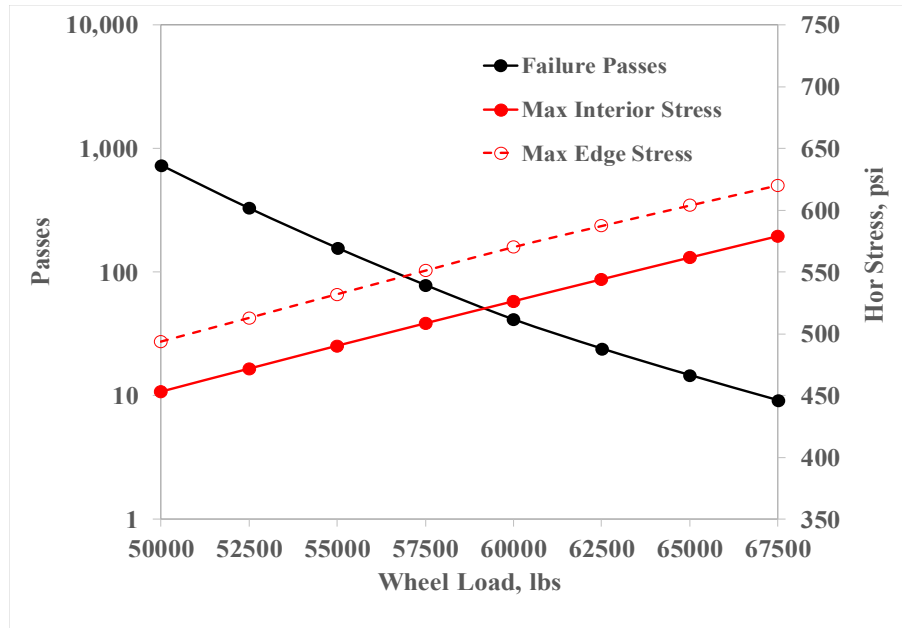
Gear	Wheel Load, lbs.	Max Horizontal Stress, psi		Failure Passes
		Edge	Interior	
3D	47500	425	481	1285
	50000	442	503	508
	52500	459	524	218
	55000	476	545	101
	57500	492	565	50
	60000	508	586	26
	62500	524	606	14
	65000	538	626	8
2D	50000	429	466	2490
	52500	446	485	1016
	55000	462	504	448
	57500	478	523	212
	60000	493	542	106
	62500	508	560	56
	65000	522	578	31
	67500	536	596	18
	70000	549	614	11
D	50000	494	453	734
	52500	513	472	329
	55000	532	490	157
	57500	551	508	79
	60000	570	526	41
	62500	587	544	24
	65000	604	562	15
	67500	620	579	9



(a)



(b)



(c)

Figure 8. FAARFIELD Predictions: (a) 3D, (b) 2D, (c) D

From Table 2:

- The critical value of horizontal stress (edge vs. interior) depends on the gear configuration.
- For the same wheel load, the D gear is most likely to damage joints due to relatively larger edge stresses.

FAARFIELD calculations assumed 1000 passes to failure, with the understanding that the actual pavement life in a traffic test might be greater. There are several reasons for this:

- In FAARFIELD design, failure is defined by the Structural Condition Index (SCI). The failure criterion is $SCI = 80$, corresponding to a condition where 50 percent of slabs in a sampling unit have completed cracks. In practice, however, full-scale tests are anticipated to bring slabs to a full-failure or shattered-slab condition, requiring additional traffic.
- Differences in the as-built versus as-designed structure can cause significant over- or under-prediction of life.
- The FAARFIELD design model contains a number of conservative assumptions that may not be reflected in the as-built structure (i.e., fully unbonded slab-base interface, infinite subgrade depth).

From Figure 8(c), a wheel load of 50,000 pounds, corresponding to a stress ratio $\sigma/R = 0.7$, gives approximately 1000 passes to failure for both north and south lanes. Therefore, 50,000 pounds was chosen as the initial wheel load for the full-scale traffic tests.

3.2.2 TEST PROCEDURE

- General. The vehicle speed was 2.5 mph with a nominal tire pressure of 220 psi.

- b. Wander Pattern. The wander pattern consisted of 66 passes (Table A1 of Appendix A). The 66 passes were arranged in 9 discrete tracks, as shown in Figure 9. Each movement of the NAPTV to the east counted as one pass, and the return to the west along the same track counted as a second pass. For Track 0, the outside tire of each dual pair aligned with the longitudinal joint in the test item. A list of carriage offset positions corresponding to each pass in the wander pattern is in Appendix A, Table A1.

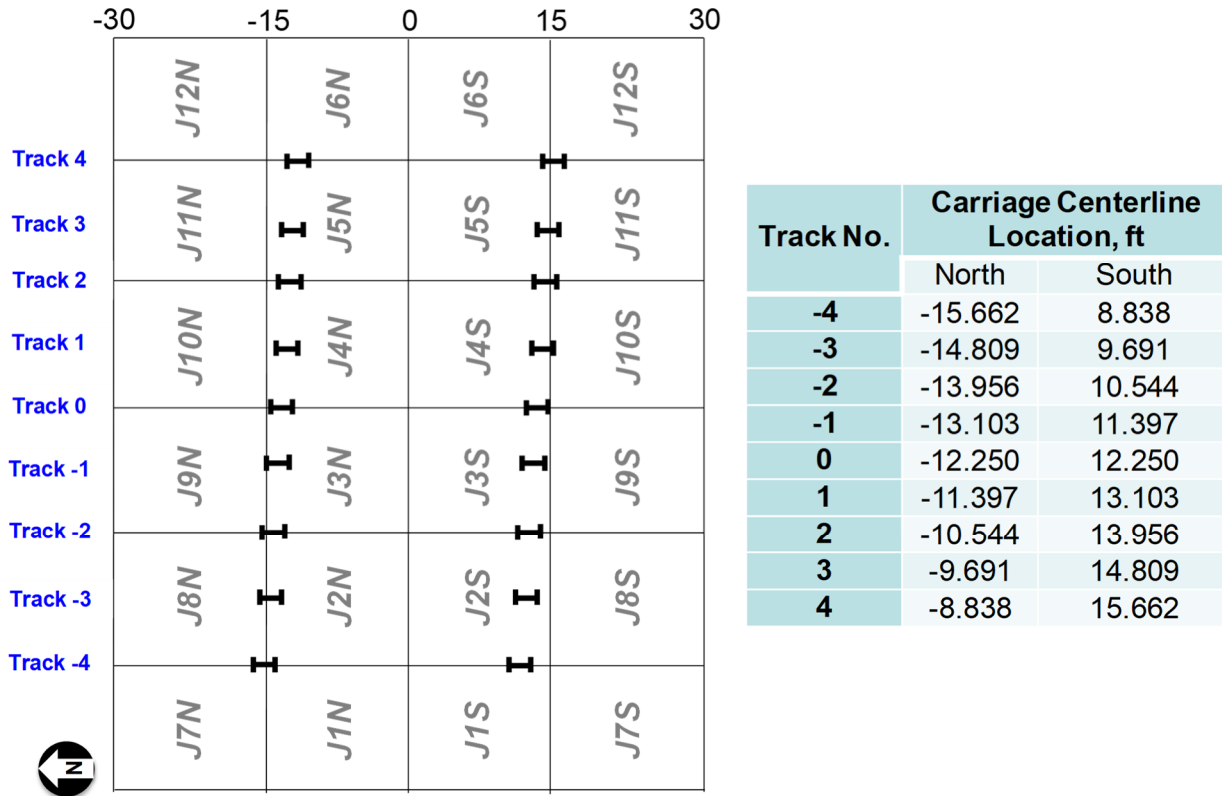
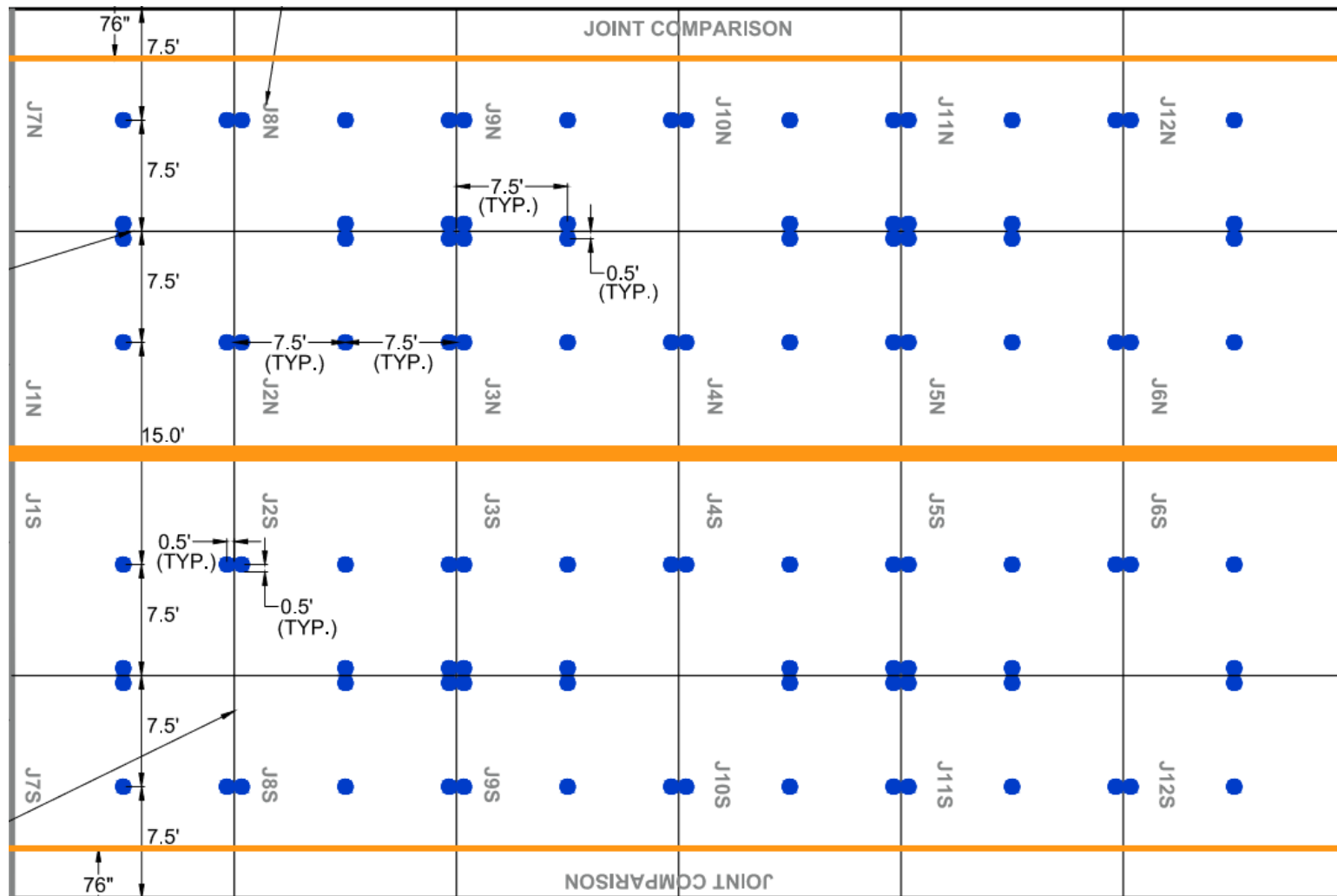


Figure 9. Wander Pattern for Trafficking

- c. Slab Identification. Each slab was labeled with a unique identifier starting with “J” as shown in Figure 9.
- d. HWD Location. HWD test locations were marked at the center of all slabs, slab edges and slab corners as illustrated in Figure 10.
- e. Flexural Strength. During both days of concrete placement, beam specimens were cast and retained for testing. These test specimens were allowed to cure in the NAPTF alongside the test items, and are referred to as “field-cured” beams. Flexural strength tests following ASTM C78 were conducted on the field-cured beams between February 13 and 15, 2018 prior to the application of seating loads (see item f). The age of these field-cured beams ranged from 287 to 294 days. FAARFIELD was then re-run with new field *R* values to refine the calculation of failure passes.

- f. Seating Loads. Seating loads were applied to the test pavement using a two-wheel (D) gear configuration at 10,000 pounds per wheel. The special seating load pattern (Figure 11 and Table A2 in Appendix A) consisted of 21 tracks spaced every 10 inches to cover the entire pavement width (except for areas near shoulders that are out of range of the load carriage). During seating, the vertical movements of the slab were monitored with ECS.
- g. Baseline HWD and PSPA. After the seating load wander, HWD tests were performed at the locations specified in (d). The HWD testing was conducted with a four-drop loading sequence beginning with an approximate 36,000-pound seating load. The subsequent loads were approximately 12,000 pounds, 24,000 pounds, and 36,000 pounds. A Portable Seismic Pavement Analyzer (PSPA) device was used to estimate surface concrete moduli. PSPA measurements were collected from slab centers and ECS-installed corners. The HWD and PSPA measurements were used to backcalculate layer moduli, and as a reference baseline to monitor subsequent slab curling and changes in support conditions.



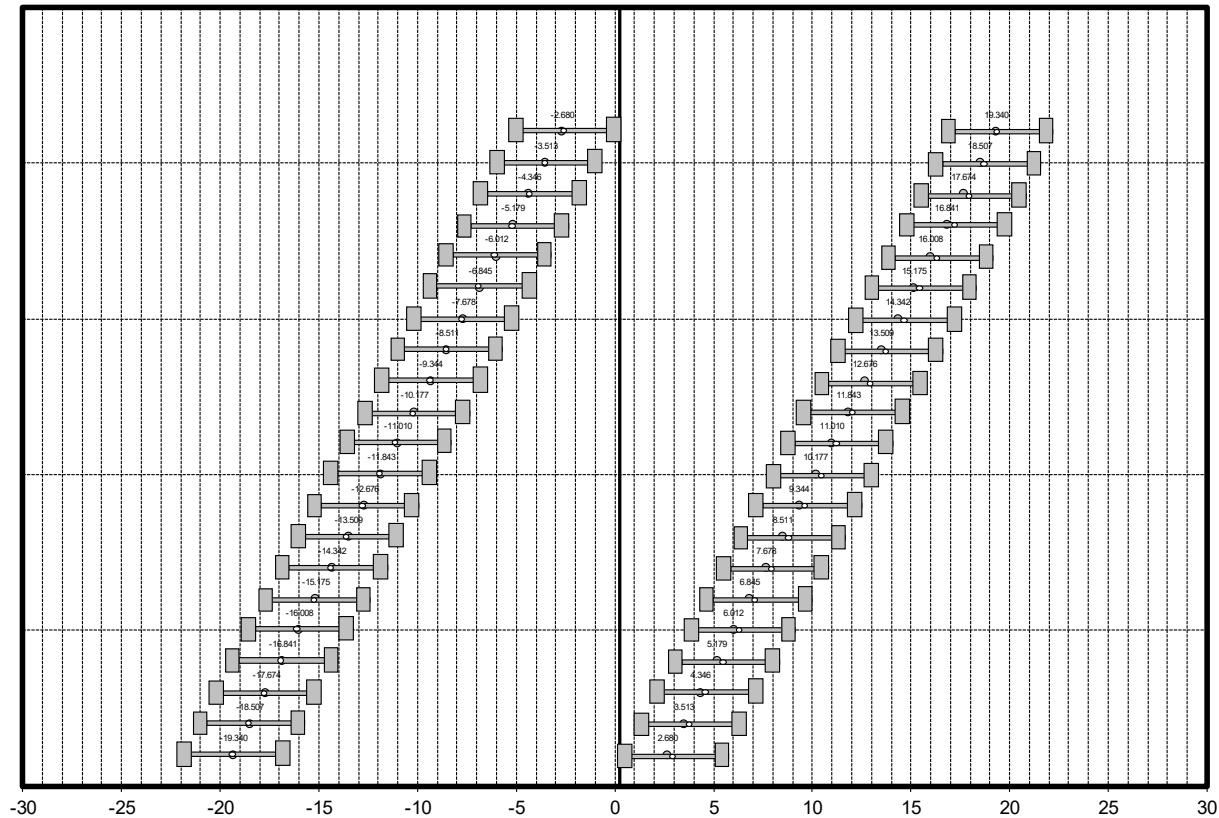


Figure 11. Seating Load Wander

- h. Ramp-up Response Test. The purpose of the ramp-up response test was to ensure all systems were operating properly, and to inform the final decision about the wheel load for the traffic test. Rolling loads were applied to both the north and south test items, using a two-wheel (D) gear configuration and the full 66-pass wander pattern (Figure 9 and Table A1 of Appendix A). The steps were:
- 1) One full traffic wander pattern (66 passes) was applied on both north and south at the initial wheel load of 50,000 pounds. The condition of slabs was monitored to verify that the pavement was not damaged. Baseline sensor readings for dynamic sensors were recorded.
 - 2) The critical tracks for maximum strain gage responses were verified. The maximum strain on the critical track for all EGs was recorded.
 - 3) The maximum strain responses at slab top and bottom in step 2 were extrapolated to the extreme fiber. The extrapolated strains were compared to the FAARFIELD computations for maximum bending strain under wheel load.
 - 4) The wheel load was increased in increments of 2,500 pounds. Only the critical tracks were trafficked in both directions (west to east, and east to west). At each load increment, step 3 was repeated until either the peak slab top or bottom tensile strain was 90% of the FAARFIELD prediction.

i. Traffic Test.

- 1) Traffic was applied to both the north and south traffic lanes using the D gear configuration. The wheel load determined in part (h) was used for the traffic test. As initially conceived, the plan was to continue traffic until the condition survey showed SCI in the single digits on both traffic lanes. If a single digit SCI was attained on either north or south, traffic would stop on that side, but continue on the other side until the SCI was less than 10. However, during the traffic phase, the original test termination criteria were modified to consider joint load transfer efficiency in addition to SCI, as explained in Section 4.
- 2) Joint Evaluation.
 - After every 10 wander patterns (about 1 day of traffic), six additional passes were executed to collect EG readings for joint evaluation. During these additional passes, the NAPTIV traveled at a speed of 2.5 mph on both traffic lanes (north and south). The loading gear configuration (D) and wheel load were the same as in Step (1). The NAPTIV was positioned in such a way the outer wheel of the carriage modules tracked directly above specific EGs of interest. The 6 additional passes consisted of one forward (west to east) and one return (east to west) pass on each of three tracks designated T1, L1 and L2. Track T1 activated transverse EGs, as illustrated in Figure 12. Track L1 activated longitudinal EGs on the inner slabs. Track L2 activated longitudinal EGs on the outer slabs. Except for track L1, these lateral gear positions did not coincide with the standard wander tracks in Fig. 9. Track L1 corresponds to a wander track 0. (During the first stage of trafficking, the position of Track L2 was initially set incorrectly and was adjusted as indicated in Figure 12.)
 - At the end of each week of traffic (about 40 wanders), HWD measurements were conducted at the longitudinal and transverse joints as shown in Figure 10.

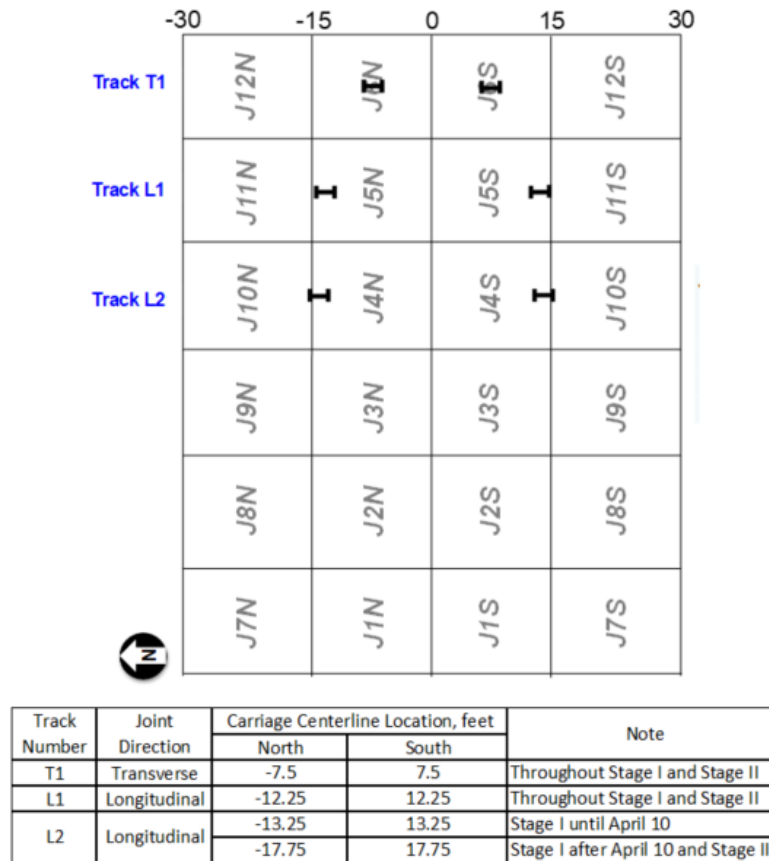


Figure 12. Gear Tracks for Joint Evaluation

3.2.3 MONITORING

- a. **Dynamic Responses.** EG and ECS responses were triggered by vehicle movements under load and sampled at 20 Hz. During traffic tests, strain gages were carefully monitored for unusual responses possibly indicating rupture or crack advancement. The raw data files were processed and stored in a database for subsequent data analysis.
- b. **Static Responses.** Temperature and moisture data were collected hourly.
- c. **Pavement Condition.**
 - 1) **Manual Distress Survey.** Distress surveys were conducted on a daily basis for 100 percent of the slabs in accordance with ASTM D5340. In addition, the test pavement was inspected informally after each wander and when the appearance of any new distress was noted. The visual surveys were augmented with wire brushes, chalk markings, flashlights, and other tools as needed to ascertain the presence and pattern of very fine cracks. Cumulative plots of crack mapping were prepared and submitted to the FAA. On these plots, the distresses were color-coded to separate dates/passes of distress survey on which new distresses were observed.

- 2) SCI Calculation. After each distress survey, pavement inspections were updated in an FAA PAVEAIR database and the SCI was calculated.
- 3) HWD and PSPA testing were conducted on a weekly basis to detect pavement deterioration and any changes in support condition over time. These measurements were taken at the blue dots as illustrated in Figure 10. Both ECS data and the edge-to-center deflection ratios were expected to provide information on separation of the PCC slabs from the lean concrete base (“lift-off”).

4. FULL-SCALE TEST

The full-scale traffic test was conducted in two stages. In both stages, a ramp-up response test was conducted to identify appropriate load levels and gear configurations, followed by traffic to a predetermined failure condition. For the Joint Comparison phase of CC8, a modified failure criterion was developed based on joint performance. Failure of a test group occurs when the average deflection-based load transfer efficiency of either contraction (transverse) or construction (longitudinal) joints is at 60% or below. Failure in terms of load transfer efficiency of joints was anticipated to occur after attaining the design structural failure condition of SCI=80.

The Stage I traffic test commenced on March 1, 2018. The traffic history is shown in table 3. Both NAPTF carriages were configured with a D gear at a wheel load of 65,000 pounds. The total number of vehicle passes under load was 42,702 (647 wander patterns). Longitudinal joints showed a gradual decrease in performance indicators over the first 38,346 vehicle passes, but stabilized thereafter. In addition to joint performance, the pavement structural condition was monitored throughout the traffic test by the SCI. After 17,292 vehicle passes, the SCI values of both the north and south side reached minimum values of 14 and 34, respectively. Similar to longitudinal joint performance indicators, the pavement condition remained constant thereafter. With no further evidence of joint performance degradation or pavement deterioration, Stage I concluded on August 9, 2018. At termination of Stage I, the joint failure criteria was met for longitudinal construction joints on both north and south traffic lanes.

The Stage II traffic test commenced on October 29, 2018 and concluded on November 8, 2018. Stage II subjected the damaged south test items (including the S-shaped keyway joint) to 3D gear loads and heavier wheel loads. Sensitivity of joint load transfer to wheel load levels was investigated earlier using data collected from the Stage I ramp-up response test. However, little sensitivity was actually observed in those data due to the elastic behavior of undamaged slabs prior to the occurrence of traffic-induced damage. Therefore, a revised ramp-up response test was conducted as part of Stage II using both D and 3D gears, with wheel loads ranging from 50,000 to 70,000 pounds. Following the Stage II-ramp-up response test, traffic was resumed on the south side only using a 3D gear configuration with a wheel load of 70,000 pounds. The failure criterion was also revised. Failure would be determined by either of the following conditions: stress-based Load Transfer Efficiency (LTE_{σ}) at longitudinal joint (S 4-10) = 60% or stress-based Load Transfer (LT_{σ}) at longitudinal joint (S 4-10) = 25%. Based on these new joint performance criteria, traffic was halted after 3,036 additional passes (46 additional wander patterns), for a total of 45,738 vehicle passes applied to the south pavement.

4.1 STAGE I TEST

4.1.1 RAMP-UP RESPONSE TEST

The ramp-up response test in preparation for the CC8 Phase 3 Joint Comparison traffic test was conducted on February 28, 2018. The pavement was trafficked with a full wander pattern at a wheel load of 50,000 pounds and the response of the EGs was monitored. Upon completion of the wander pattern, the strain data were processed and analyzed. For each pass, the maximum strain response was determined for all EGs. The test identified the following longitudinal gages as having the maximum tensile peak strain responses over the entire wander:

North Traffic Lane (top of slab): EG-N-J-II-13 (Critical wander position: Track 0)

North Traffic Lane (bottom of slab): EG-N-J-II-12 (Critical wander position: Track -1)

South Traffic Lane (top of slab): EG-S-J-II-21 (Critical wander position: Track 0)

South Traffic Lane (bottom of slab): EG-S-J-II-4 (Critical wander position: Track 1)

For both north and south, the maximum tensile strain response of in EGs at the bottom of the concrete slab was greater than the maximum tensile strain at the top.

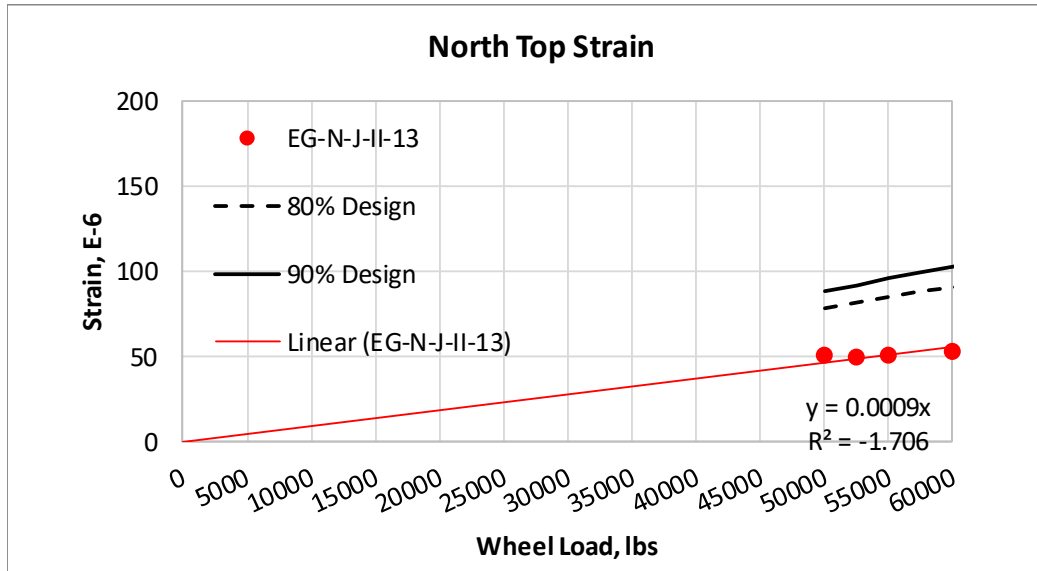
Subsequent wheel load increments (52,500, 55,000, 60,000, and 65,000 pounds) trafficked only two vehicle passes (west to east and east to west) on each critical wander position. The maximum strain responses in the monitored EGs were extrapolated linearly to estimate the maximum strains at both the top and bottom extreme fibers. Next, the FAARFIELD horizontal strains were obtained for each wheel load level. These strains defined the envelope for maximum allowable responses during the ramp-up test. Figure 11 and Figure 12 compare allowable response envelopes at 80% and 90% of the computed FAARFIELD strain to the extrapolated maximum tensile strains at the extreme fiber for both the north and south test item.

In Figure 13 and Figure 14, regardless of wheel load magnitude, the extrapolated tensile strains at the top extreme fiber were well below the 80% envelope on both sides of the pavement. In contrast, the tensile strains at the bottom extreme fiber fell on or slightly below the 80% envelope on the north side, and below the 80% line on the south side. Since the extrapolated tensile strains never exceeded the 80% envelope up for wheel loads up to 65,000 pounds, 65,000 pounds was selected as the starting load for the traffic test.

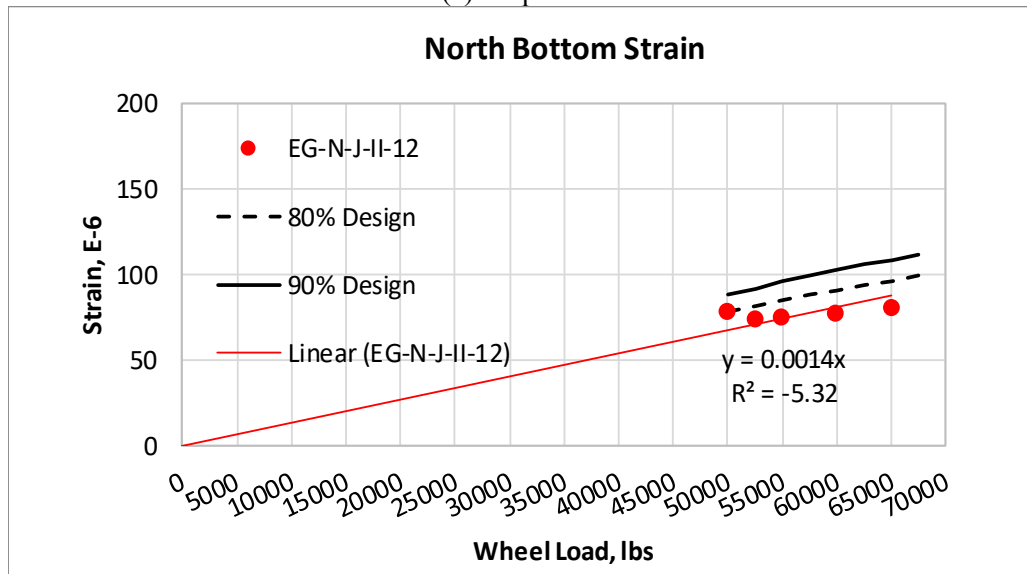
4.1.2 STAGE I TRAFFIC TEST

The traffic test started on March 1, 2018. Both carriages (north and south) had a D configuration (figure 7). Target wheel loads were 65,000 pounds at 220 psi nominal tire pressure. Vehicle speed was 2.5 mph. After 17,292 vehicle passes, SCI values on the north and south test items were 14 and 34 respectively. From that point on, the pavement condition remained the same until the end of the test. Monitoring data from longitudinal joints showed a steady deterioration in performance measures under traffic for the first 38,346 passes, followed by stabilization. With no indicators of further degradation or pavement deterioration, the traffic test was terminated on August 9, 2018 after a total of 42,702 vehicle passes.

Table 3 is a summary of Stage I traffic.

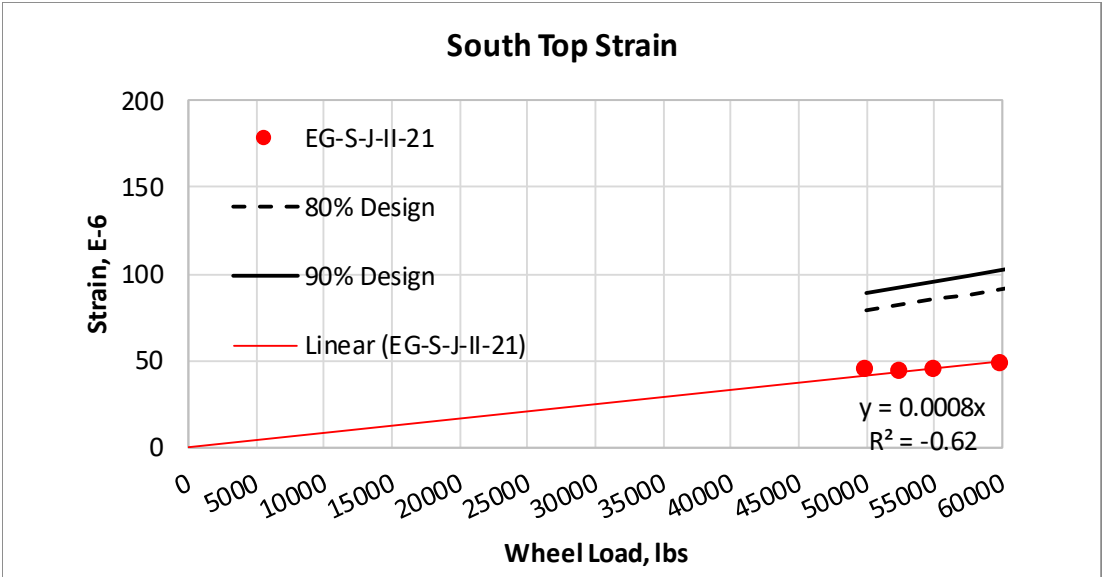


(a) Top Strain

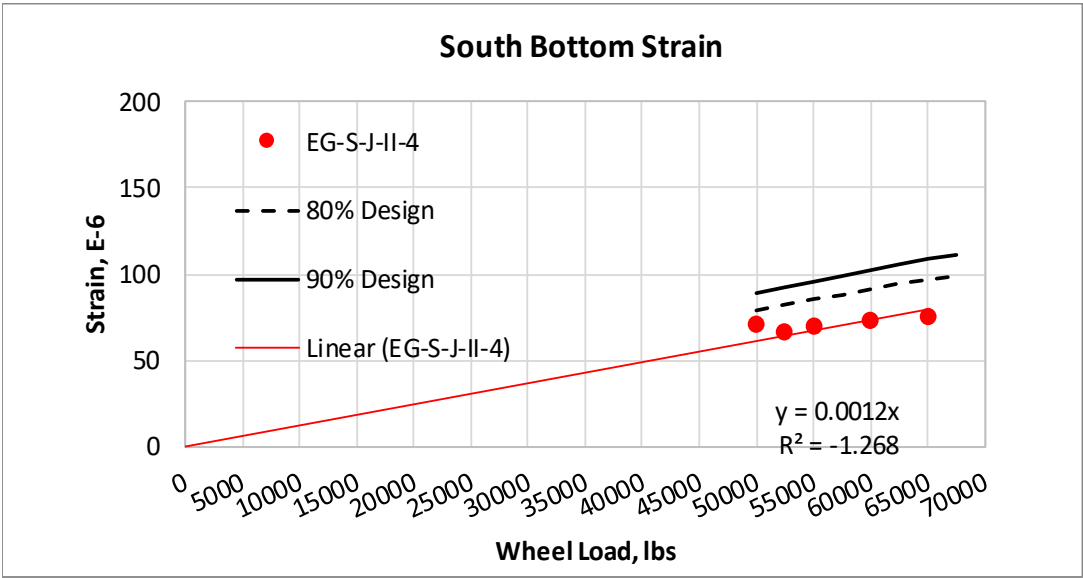


(b) Bottom Strain

Figure 13. Stage I-Ramp-Up Response Test Results, North Test Item (02/28/2018)



(a) Top Strain



(b) Bottom Strain

Figure 14. Stage I-Ramp-Up Response Test Results, South Test Item (02/28/2018)

Table 3. Stage I-Traffic Test History

Day No	Date	Number of Passes	Number of Wanders	Cumulative Passes	Day No	Date	Number of Passes	Number of Wanders	Cumulative Passes
1	3/1/2018	396	6.0	396	38	5/17/2018	594	9.0	21912
2	3/2/2018	594	9.0	990	39	5/21/2018	594	9.0	22506
3	3/5/2018	594	9.0	1584	40	5/22/2018	594	9.0	23100
4	3/6/2018	594	9.0	2178	41	5/23/2018	594	9.0	23694
5	3/7/2018	528	8.0	2706	42	5/24/2018	594	9.0	24288
6	3/8/2018	594	9.0	3300	43	5/26/2018	594	9.0	24882
7	3/12/2018	594	9.0	3894	44	5/30/2018	594	9.0	25476
8	3/13/2018	594	9.0	4488	45	5/31/2018	594	9.0	26070
9	3/14/2018	594	9.0	5082	46	6/4/2018	594	9.0	26664
10	3/15/2018	594	9.0	5676	47	6/5/2018	594	9.0	27258
11	3/19/2018	594	9.0	6270	48	6/6/2018	594	9.0	27852
12	3/20/2018	594	9.0	6864	49	6/7/2018	594	9.0	28446
13	3/22/2018	396	6.0	7260	50	6/11/2018	594	9.0	29040
14	3/26/2018	594	9.0	7854	51	6/12/2018	594	9.0	29634
15	3/27/2018	594	9.0	8448	52	6/13/2018	594	9.0	30228
16	3/28/2018	594	9.0	9042	53	6/14/2018	594	9.0	30822
17	3/29/2018	594	9.0	9636	54	6/18/2018	594	9.0	31416
18	4/2/2018	528	8.0	10164	55	6/19/2018	594	9.0	32010
19	4/3/2018	594	9.0	10758	56	6/20/2018	594	9.0	32604
20	4/4/2018	594	9.0	11352	57	6/21/2018	528	8.0	33132
21	4/5/2018	594	9.0	11946	58	6/25/2018	594	9.0	33726
22	4/9/2018	594	9.0	12540	59	6/26/2018	594	9.0	34320
23	4/10/2018	594	9.0	13134	60	6/27/2018	594	9.0	34914
24	4/19/2018	594	9.0	13728	61	6/28/2018	594	9.0	35508
25	4/23/2018	594	9.0	14322	62	7/2/2018	458	6.9 ¹	35966
26	4/24/2018	594	9.0	14916	63	7/23/2018	598	9.1 ¹	36564
27	4/25/2018	594	9.0	15510	64	7/24/2018	594	9.0	37158
28	4/26/2018	594	9.0	16104	65	7/25/2018	594	9.0	37752
29	4/30/2018	594	9.0	16698	66	7/26/2018	594	9.0	38346
30	5/1/2018	594	9.0	17292	67	7/30/2018	594	9.0	38940
31	5/2/2018	594	9.0	17886	68	7/31/2018	594	9.0	39534
32	5/3/2018	462	7.0	18348	69	8/1/2018	594	9.0	40128
33	5/7/2018	594	9.0	18942	70	8/2/2018	594	9.0	40722
34	5/8/2018	594	9.0	19536	71	8/6/2018	594	9.0	41316
35	5/9/2018	594	9.0	20130	72	8/7/2018	594	9.0	41910
36	5/14/2018	594	9.0	20724	73	8/8/2018	594	9.0	42504
37	5/16/2018	594	9.0	21318	74	8/9/2018	198	3.0	42702

¹The vehicle was stopped after completing 458 passes due to damage found in the power lines used by the NAPT. The partial wander was completed on July 23 after repairs were finished on the vehicle power rails.

4.2 STAGE II TEST

4.2.1 REVISED RAMP-UP RESPONSE TEST

Prior to resuming the traffic test, the FAA conducted a second ramp-up load response test. This was necessary to determine the level of increased load to accelerate joint deterioration. Analysis of data collected during the Stage I ramp-up test (4.1.1) showed little sensitivity of joint performance indicators to the change in wheel load. It was surmised that this lack of sensitivity was due to the undamaged condition of slabs, and therefore a test of the damaged slabs might show increased sensitivity to varying wheel loads.

Two sets of moving load tests were conducted on October 15 and 16. These were to evaluate the joint performance under D and 3D gear configurations, respectively. The wander pattern consisted of 30 vehicle passes applied along three tracks: T1, L1, and L2 in Figure 15. Track T1 activated transverse joint sensors, while tracks L1 and L2 activated longitudinal joint sensors. On each track, the initial 50,000-pound wheel load was increased in 5,000 pounds increments up to 70,000 pounds (

Table 4). The same wheel load was used for D and 3D tests. All tests were conducted at a vehicle speed of 2.5 mph with nominal tire pressure of 220 psi.

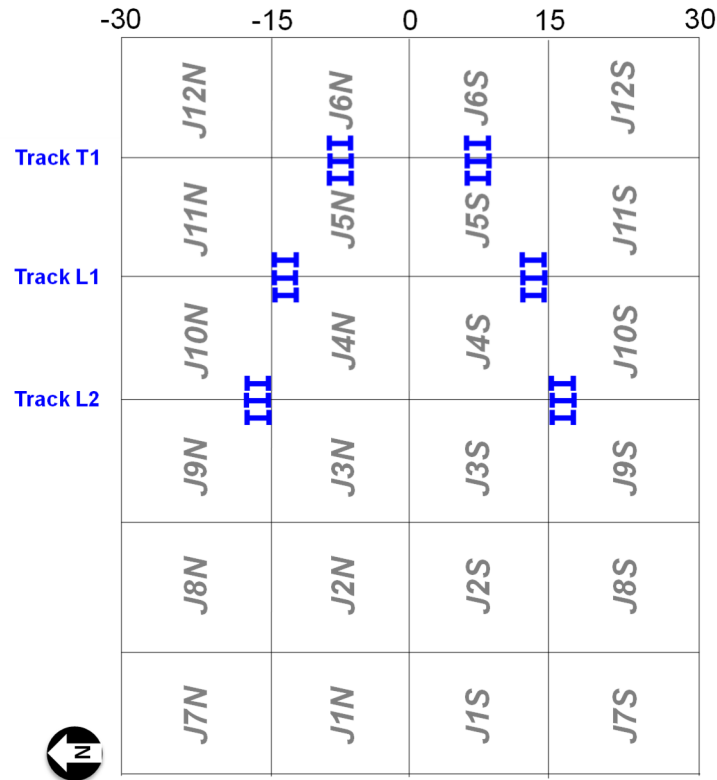


Figure 15. Tracks for the Stage II Ramp-Up Response Test

Table 4. Wander Pattern for Stage II Ramp-Up Response Test

Pass Sequence No.	Direction	Track	Carriage Centerline Location, ft.		Wheel Load, lb.
			North	South	
1	W to E	T1	-7.750	7.750	50000
2	E to W	T1	-7.750	7.750	50000
3	W to E	T1	-7.750	7.750	55000
4	E to W	T1	-7.750	7.750	55000
5	W to E	T1	-7.750	7.750	60000
6	E to W	T1	-7.750	7.750	60000
7	W to E	T1	-7.750	7.750	65000
8	E to W	T1	-7.750	7.750	65000
9	W to E	T1	-7.750	7.750	70000
10	E to W	T1	-7.750	7.750	70000
11	W to E	L1	-12.250	12.250	50000
12	E to W	L1	-12.250	12.250	50000

13	W to E	L1	-12.250	12.250	55000
14	E to W	L1	-12.250	12.250	55000
15	W to E	L1	-12.250	12.250	60000
16	E to W	L1	-12.250	12.250	60000
17	W to E	L1	-12.250	12.250	65000
18	E to W	L1	-12.250	12.250	65000
19	W to E	L1	-12.250	12.250	70000
20	E to W	L1	-12.250	12.250	70000
21	W to E	L2	-17.750	17.750	50000
22	E to W	L2	-17.750	17.750	50000
23	W to E	L2	-17.750	17.750	55000
24	E to W	L2	-17.750	17.750	55000
25	W to E	L2	-17.750	17.750	60000
26	E to W	L2	-17.750	17.750	60000
27	W to E	L2	-17.750	17.750	65000
28	E to W	L2	-17.750	17.750	65000
29	W to E	L2	-17.750	17.750	70000
30	E to W	L2	-17.750	17.750	70000

Joint performance was evaluated from two variables: stress-based load transfer (LT_σ) and stress-based load transfer efficiency (LTE_σ). For the case of a wheel load acting on only one side of a joint, they are calculated as follows:

$$LT_\sigma(\%) = \frac{\sigma_U}{\sigma_L + \sigma_U} \times 100 = \frac{\varepsilon_U E_U}{\varepsilon_L E_L + \varepsilon_U E_U} \times 100 \quad (1)$$

$$LTE_\sigma(\%) = \frac{\sigma_U}{\sigma_L} \times 100 = \frac{\varepsilon_U E_U}{\varepsilon_L E_L} \times 100 \quad (2)$$

where;

- σ_L = peak stress in the loaded slab;
- σ_U = simultaneous stress in the unloaded slab;
- ε_L = peak strain in the loaded slab;
- ε_U = simultaneous strain in the unloaded slab;
- E_L = elastic modulus of loaded slab; and
- E_U = elastic modulus of unloaded slab.

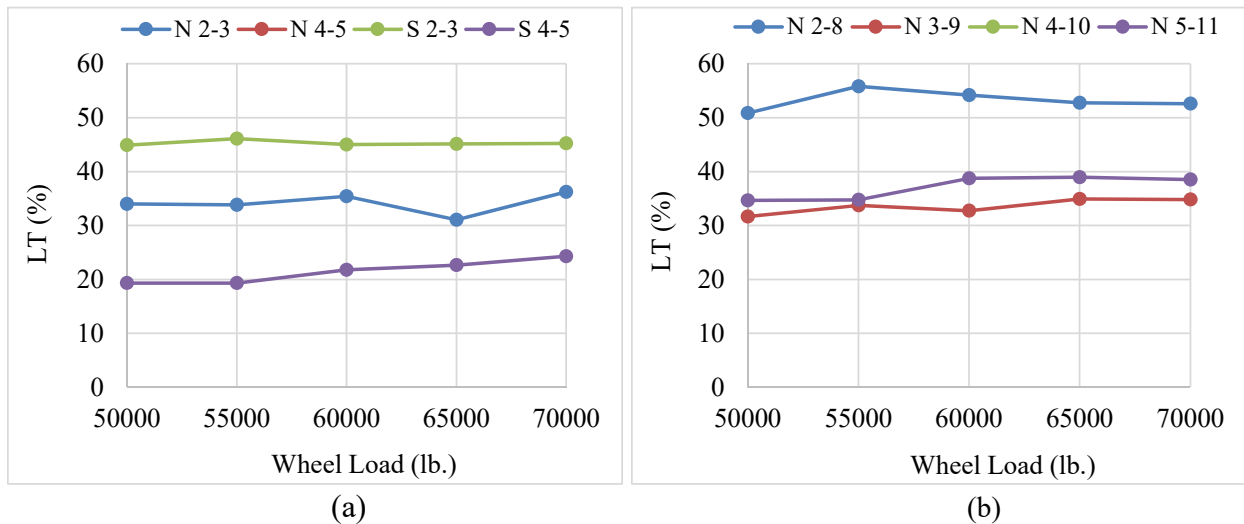
Figure 16(a) through (c) show how LT_σ varies with increasing wheel loads for the D gear configuration, for transverse and longitudinal joints. Figures 16(a) and (b) show no little or no sensitivity of LT_σ to increased wheel loads for transverse joints or for doweled longitudinal joints. However, figure 16(c) shows an increase in LT_σ between 4% and 10% for the sinusoidal longitudinal joint.

Figure 17(a) through (c) show the LTE_{σ} variation with increasing wheel load for the D gear configuration. Similar to LT_{σ} , both transverse joints and the doweled longitudinal joint on the north side did not show evidence of sensitivity to load. However, the sinusoidal longitudinal joint on the south side showed a positive correlation between LTE_{σ} and increasing wheel load. In this case, the LTE_{σ} increased between 9% and 26%.

Figures 18(a) through (c) show how LT_{σ} varies with increasing wheel load for the 3D gear configuration. Figures 18(a) and 18(b) show no sensitivity to increasing wheel loads for transverse joints or doweled longitudinal joints. In figure 18(c), sinusoidal longitudinal joints on the south side showed a consistent increase in LT with increasing wheel load. The value of LT_{σ} increased between 8% and 14% as the wheel load increased from 50,000 to 70,000 pounds.

Figures 19(a) through (c) show the LTE_{σ} variation with increasing wheel load for the 3D gear configuration. Similar to figures 16-18, transverse joints and longitudinal joints on the north side did not show evidence that LTE_{σ} is sensitive to load. Doweled longitudinal joints on the north side showed only a slight increase in LTE_{σ} with increasing load. For sinusoidal longitudinal joints on the south side, LTE_{σ} increased between 19% and 35% as the wheel load increased from 50,000 to 70,000 pounds.

Only the sinusoidal longitudinal joints in the south test items consistently showed increasing load transfer with increasing wheel load. Furthermore, the sensitivity of both LT_{σ} and LTE_{σ} to increasing wheel load with the 3D gear was higher than with the D gear. To maximize load transfer through the longitudinal joints, the traffic test was resumed using a 3D gear configuration at 70,000 pounds per wheel, but only on the south test items.



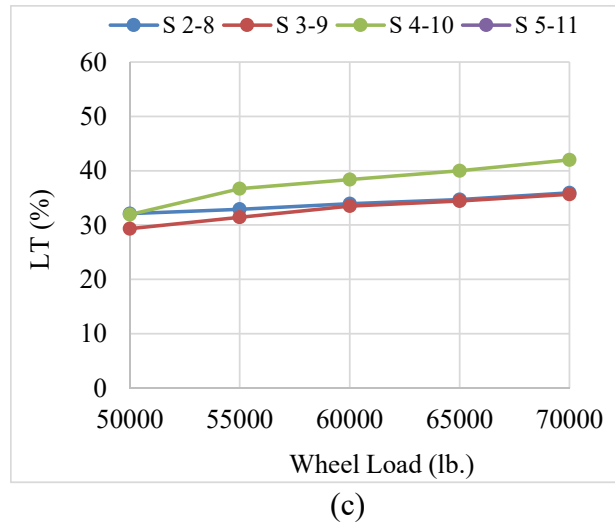


Figure 16. LT Sensitivity to Wheel Load for D Gear: (a) Transverse Joints, (b) Longitudinal Joint, North Side, (c) Longitudinal Joint, South Side

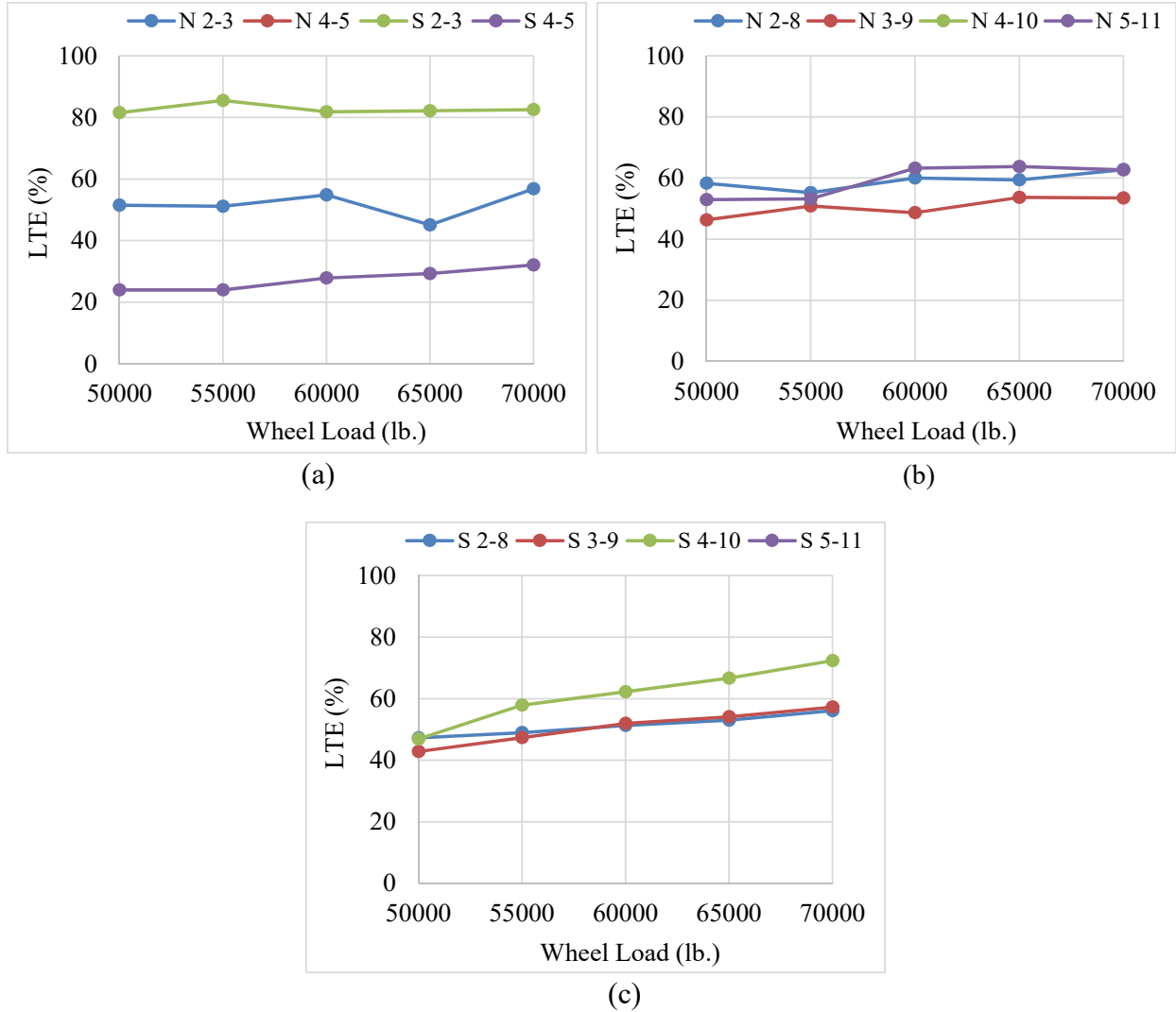


Figure 17. LTE Sensitivity to Wheel Load for D Gear: (a) Transverse Joints, (b) Longitudinal Joint, North Side, (c) Longitudinal Joint, South Side

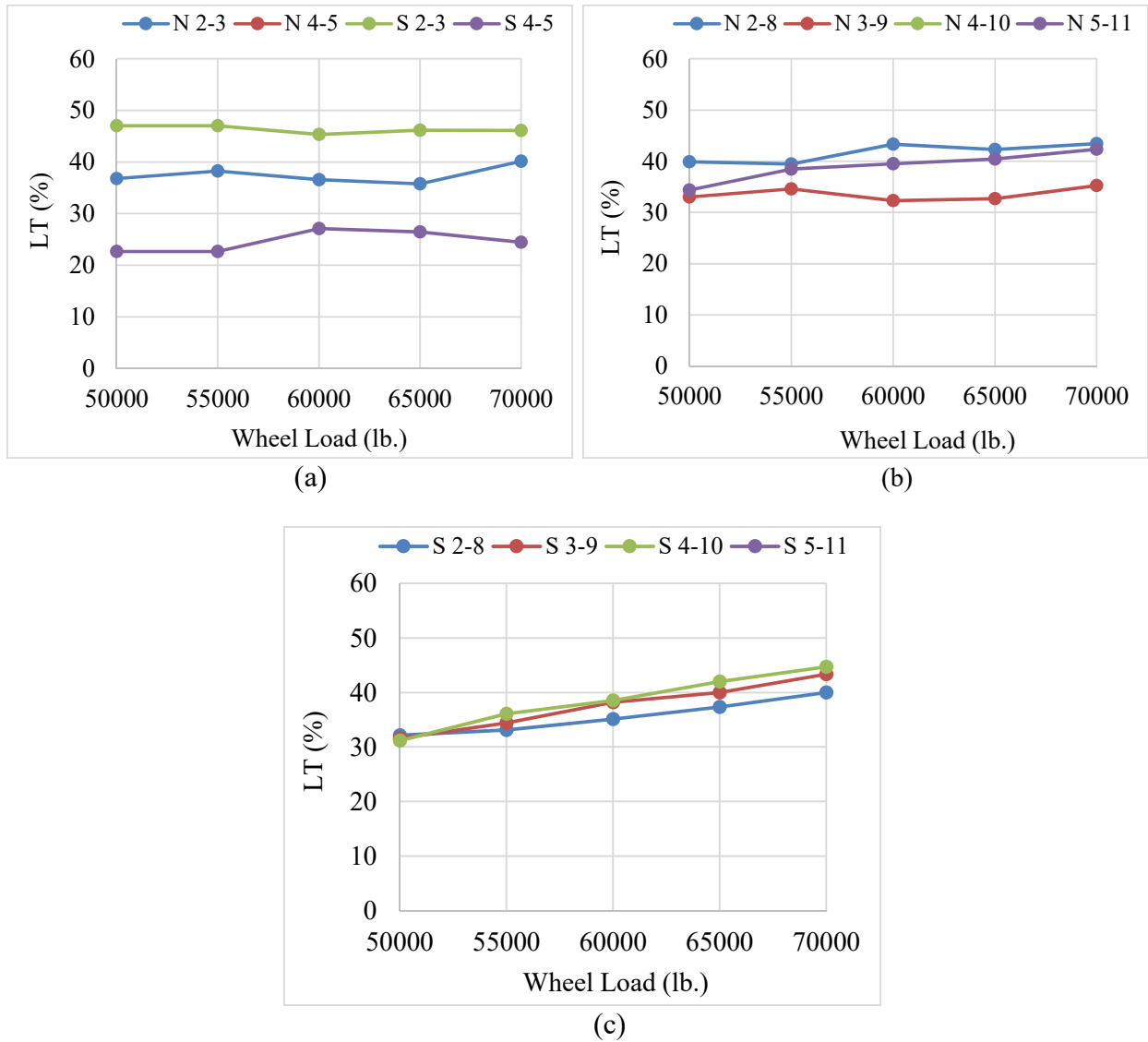


Figure 18. LT Sensitivity to Wheel Load for 3D Gear: (a) Transverse Joints, (b) Longitudinal Joint, North Side, (c) Longitudinal Joint, South Side

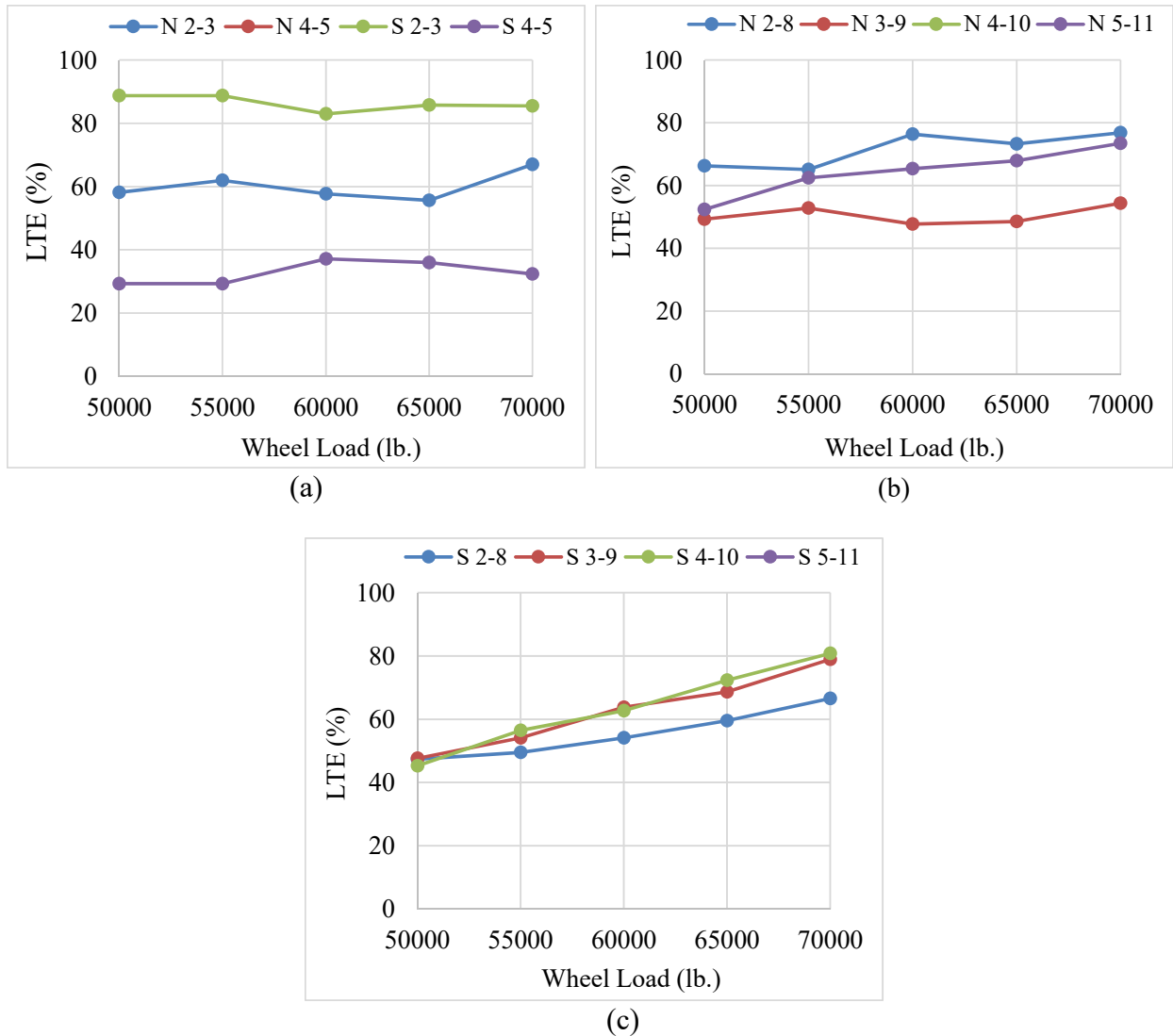


Figure 19. LTE Sensitivity to Wheel Load for 3D Gear: (a) Transverse Joints, (b) Longitudinal Joint, North Side, (c) Longitudinal Joint, South Side

4.2.2 STAGE II TRAFFIC TEST

The second stage of the traffic test was conducted using the NAPTV with a 3D gear configuration on the south traffic lane only. Wheel loads were of 70,000 pounds at a nominal tire pressure of 220 psi, and the vehicle speed was 2.5 mph. The same 66-position wander pattern used in Stage I was repeated in Stage II (Appendix A, Table A1). Traffic was continued until a revised failure condition was satisfied: either (a) $LTE_{\sigma} < 60\%$ at longitudinal joint *S 4-10*, or (b) $LT_{\sigma} < 25\%$ at longitudinal joint *S 4-10*.

After every 10 wander patterns (about 1 day of continuous traffic), an additional six passes were executed with the NAPTV, again on the south test item only. These additional passes used the same 70,000 lbs. per-wheel 3D gear configuration, but on tracks T1, L1 and L2 in figure 15. In addition, at the end of each week of traffic (about 40 wander patterns), HWD tests were conducted

at the longitudinal and transverse joints. Data from these additional vehicle passes and HWD tests were used to quantify joint load transfer at various stages of traffic.

The Stage II traffic test began on October 29, 2018 and ended on November 8, 2018. Before traffic resumed on October 29, 42,702 vehicle passes already had been applied in Stage I. During Stage II, an additional 3,036 passes were applied to the south test pavement. During Stage II, the SCI of the south test pavement dropped from 34 to 12. The final LTE_{σ} and LT_{σ} values for longitudinal joint *S 4-10* were 4.3% and 4.1% respectively, well below the set failure criterion. Table 5 summarizes Stage II traffic. The “Day Number” column in table 5 continues the count of traffic days from Stage I.

Table 5. Stage II Traffic Test History

Day Number	Date	Number of Passes	Number of Wander Patterns	Cumulative Passes
75	10/29/2018	136	2.1 ¹	42838
76	11/1/2018	524	7.9 ¹	43362
77	11/5/2018	594	9.0	43956
78	11/6/2018	594	9.0	44550
79	11/7/2018	594	9.0	45144
80	11/8/2018	594	9.0	45738

¹Traffic was stopped after 136 passes due to a hydraulic leak. The partial wander was completed on November 1.

5. BEHAVIOR OF TEST SECTION UNDER TRAFFIC

5.1 JOINT PERFORMANCE

Performance comparisons between joint types are based primarily on changes in LTE_{σ} and joint stiffness (k_j) over the course of traffic. This section discusses the method of calculating these variables using strain gage and HWD data.

5.1.1 INSTRUMENTATION DATA

Embedded strain gage data were used to calculate LTE_{σ} . As indicated in Section 3.2.2(i), longitudinal and transverse joints were evaluated after every 10 wander patterns (about 1 day of traffic) throughout the course of both Stage I and Stage II. Six additional passes at the end of each day of traffic were applied to the pavement with the NAPTIV positioned in such a way that the outer wheel of the carriage modules tracked directly above specific EGs of interest. Data from EGs installed at the bottom of slabs were used to determine both stress-based Load Transfer (LT_{σ}) and stress-based Load Transfer Efficiency (LTE_{σ}) using Equations 1 and 2 (Section 4.2.1), respectively. These two equations are conveniently recalled as follows:

$$LT_{\sigma}(\%) = \frac{\sigma_U}{\sigma_L + \sigma_U} \times 100 = \frac{\varepsilon_U E_U}{\varepsilon_L E_L + \varepsilon_U E_U} \times 100 \quad (1)$$

$$LTE_{\sigma}(\%) = \frac{\sigma_U}{\sigma_L} \times 100 = \frac{\varepsilon_U E_U}{\varepsilon_L E_L} \times 100 \quad (2)$$

where;

- σ_L = peak stress in the loaded slab;
- σ_U = simultaneous stress in the unloaded slab;
- ε_L = peak strain in the loaded slab;
- ε_U = simultaneous strain in the unloaded slab;
- E_L = elastic modulus of loaded slab; and
- E_U = elastic modulus of unloaded slab.

Two different approaches to make use of the available EG data were followed (3). The first one is the “sensor pair” approach. Considered as the default method, the “Sensor Pair” approach was applied whenever a pair of EGs installed at the bottom of slabs, one on each side of the joint under evaluation, produced usable data. For this case, the principle to determine both loaded and unloaded strains is illustrated in Figure 20. The Sensor Pair approach was used to obtain LT_σ and LTE_σ for both longitudinal and transverse joints.

The second approach is the “geometric” approach. This method was used when one of the EGs (on either side of the joint under evaluation) was unreliable or failed. The geometric computation is illustrated in Figure 21. Because the geometric approach depends on identifying an “inflection point” as the wheel crosses the joint, it is only applicable to transverse joints. The modulus of the unloaded slab is used to estimate stress in both loaded and unloaded slabs.

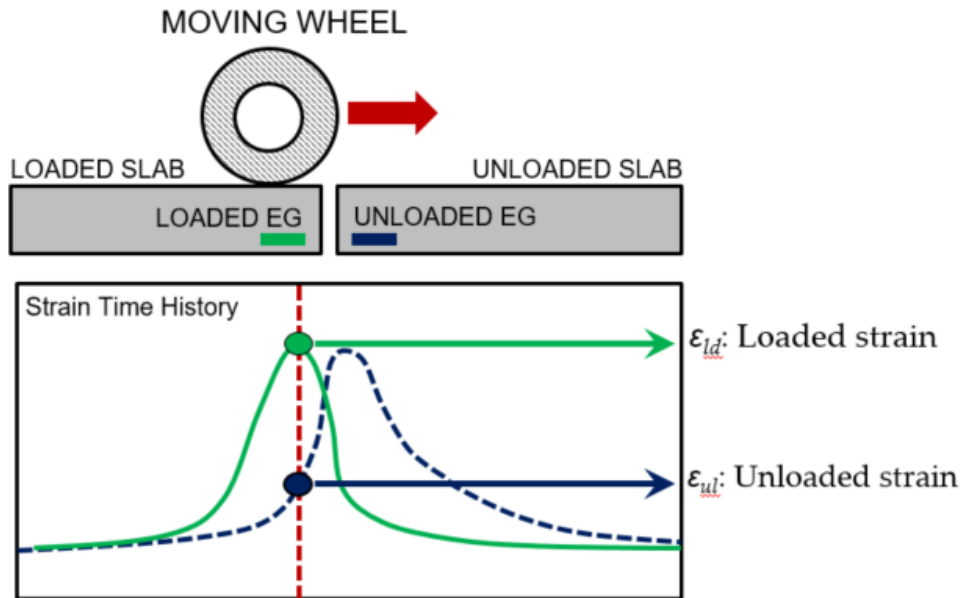


Figure 20. Sensor Pair Approach to Determine LT_σ and LTE_σ

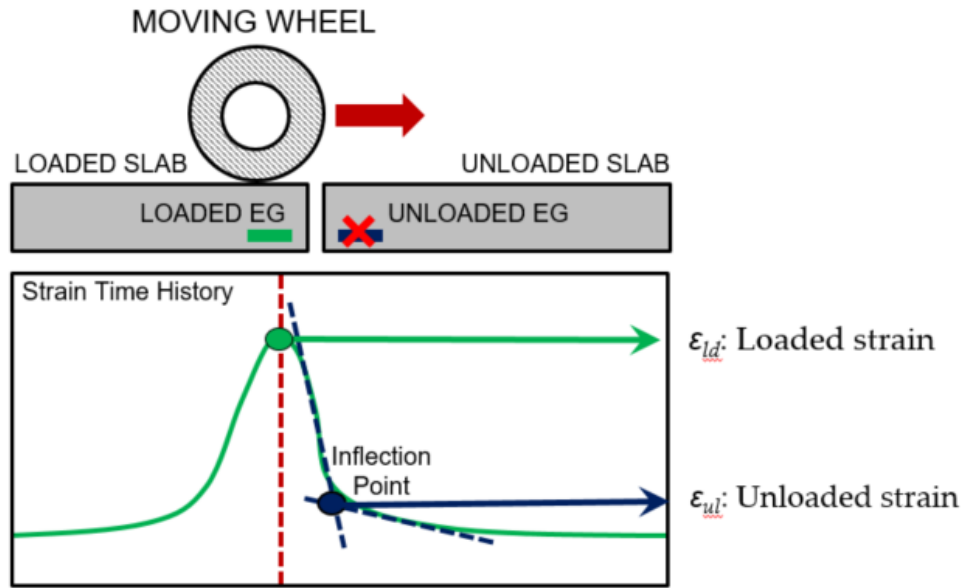


Figure 21. Geometric Approach to Determine LT_{σ} and LTE_{σ}

Elastic moduli of concrete used to determine LTE_{σ} and LT_{σ} were obtained from measurements at the center of slabs using the PSPA seismic device. Table 6 summarizes the moduli of slabs where EGs were installed along joints. Data in Table 6 are organized by slab group and lane.

Table 6. Summary of Slab Modulus for LTE_{σ} and LT_{σ} Calculation

Slab ID	Group	Lane	E (ksi)	Slab ID	Group	Lane	E (ksi)
J2N	North-West	Inner	4543.3	J2S	South-West	Inner	4930.0
J3N	North-West	Inner	4279.0	J3S	South-West	Inner	5218.3
J4N	North-East	Inner	4722.2	J4S	South-East	Inner	4810.0
J5N	North-East	Inner	4531.1	J5S	South-East	Inner	4583.3
J8N	North-West	Outer	4561.8	J8S	South-West	Outer	4732.2
J9N	North-West	Outer	4760.0	J9S	South-West	Outer	4434.3
J10N	North-East	Outer	4835.6	J10S	South-East	Outer	4297.8
J11N	North-East	Outer	4908.3	J11S	South-East	Outer	4381.1

For monitoring purposes, daily color-coded plots showing the evolution of LT_{σ} over the entire pavement area were generated. Figure 22 is an example of such a plot. It shows the initial LT_{σ} distribution at the end of the first day of trafficking on March 1, 2018 (i.e., pass # 396). Three color codes were used:

- (a) Adequate: Green ($LT_{\sigma} > 25$); and
- (b) Inadequate: Red ($LT_{\sigma} < 25$).

As of March 1, most of the transverse and longitudinal joints had LT_{σ} in excess of 25%. The undoweled transverse joints at station 4+60 were the clear exception. After the first day of trafficking, these undoweled transverse joints were in “Inadequate” condition since the LT_{σ} values were below 25%. The complete set of LT_{σ} color plots can be found in appendix B.

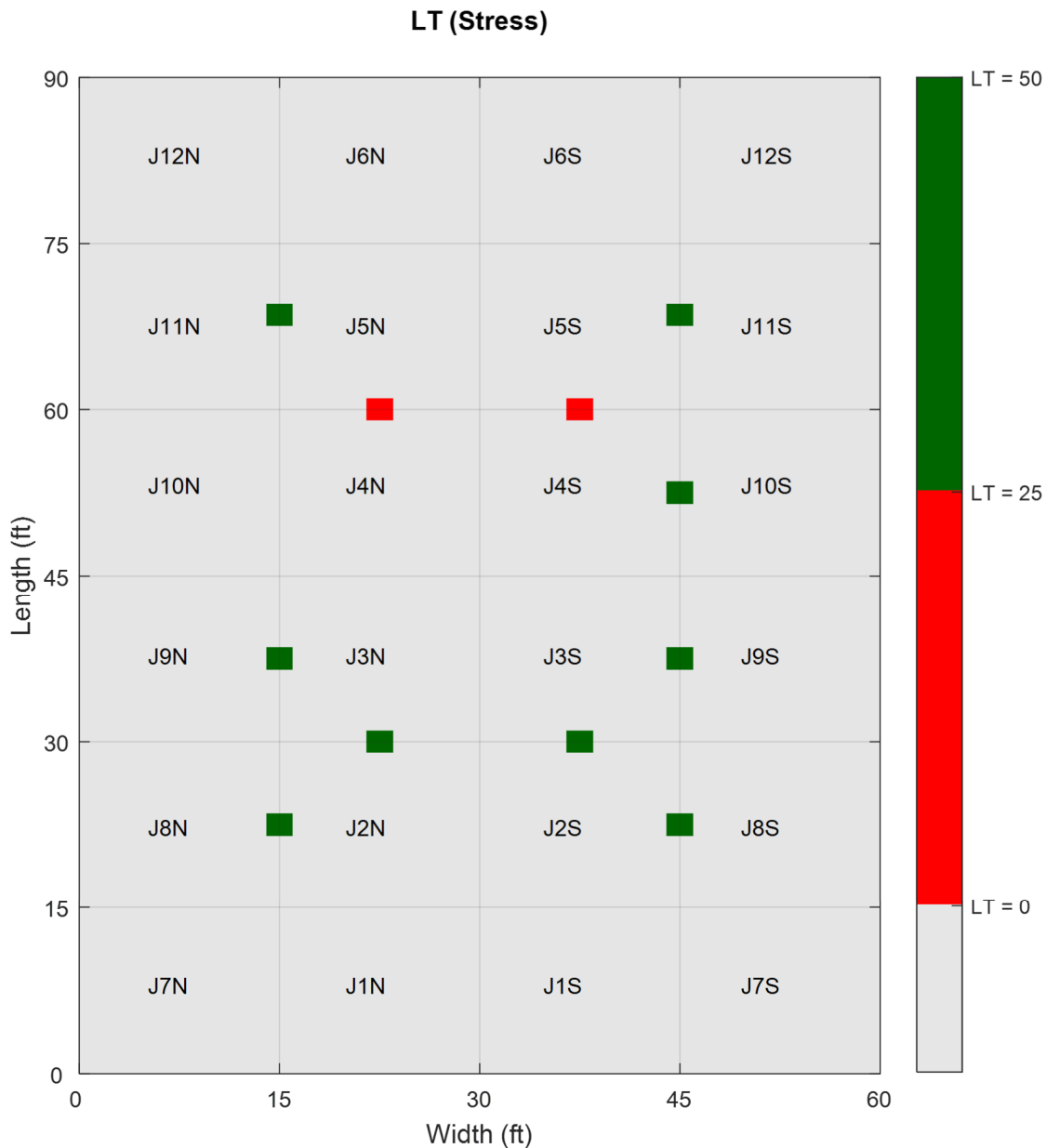


Figure 22. LT_{σ} Levels at 396 Vehicle Passes (March 1, 2018)

5.1.2 HWD DEFLECTION

There are 10 transverse joints (5 on the north lane and 5 on the south lane) and 2 longitudinal joints in the joint comparison test area. HWD tests were conducted along these joints to determine the deflection-based load transfer efficiency (LTE_δ), as illustrated in Figure 23. The measurement was conducted at the slab edge, midway between joints. Deflections are for the maximum (36,000 lb.) drop load. The LTE_δ was calculated as:

$$LTE_\delta(\%) = \frac{\delta_{ul}}{\delta_{ld}} \times 100 \quad (3)$$

Where:

δ_{ld} = deflection of the loaded slab (measured under the HWD load plate); and

δ_{ul} = deflection of the unloaded, or free, slab (measured 12 in. from the load plate center).

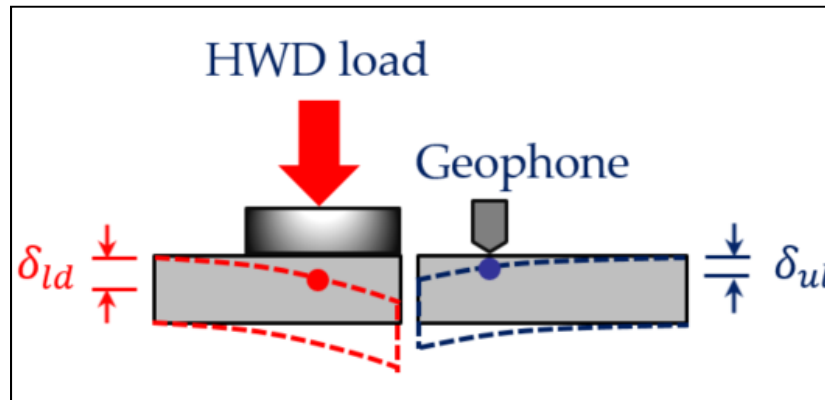


Figure 23. HWD Test Schematic to Determine LTE_δ

HWD tests were repeated weekly. During Stage II, HWD deflections were monitored on the south test items only.

For monitoring purposes, color-coded plots showing the evolution of LTE_δ were generated. Figure 24 is an example of such a plot. It shows the initial LTE_δ distribution (just after the initial seating loads). Four color codes were used arbitrarily:

- (a) Excellent: Blue ($LTE_\delta > 90$);
- (b) Good: Green ($LTE_\delta = 89$ to 70);
- (c) Fair: Yellow ($LTE_\delta = 69$ to 50); and
- (d) Poor: Red ($LTE_\delta < 50$).

Most of the joints were either “Good” or “Excellent” prior to traffic. The exceptions were the transverse undoweled contraction (dummy) joints at station 4+60, as was the case with the initial assessment of LT_σ (see 5.1.1). The LTE_δ color plots were updated weekly. A complete set of LTE_δ color plots is in appendix B.

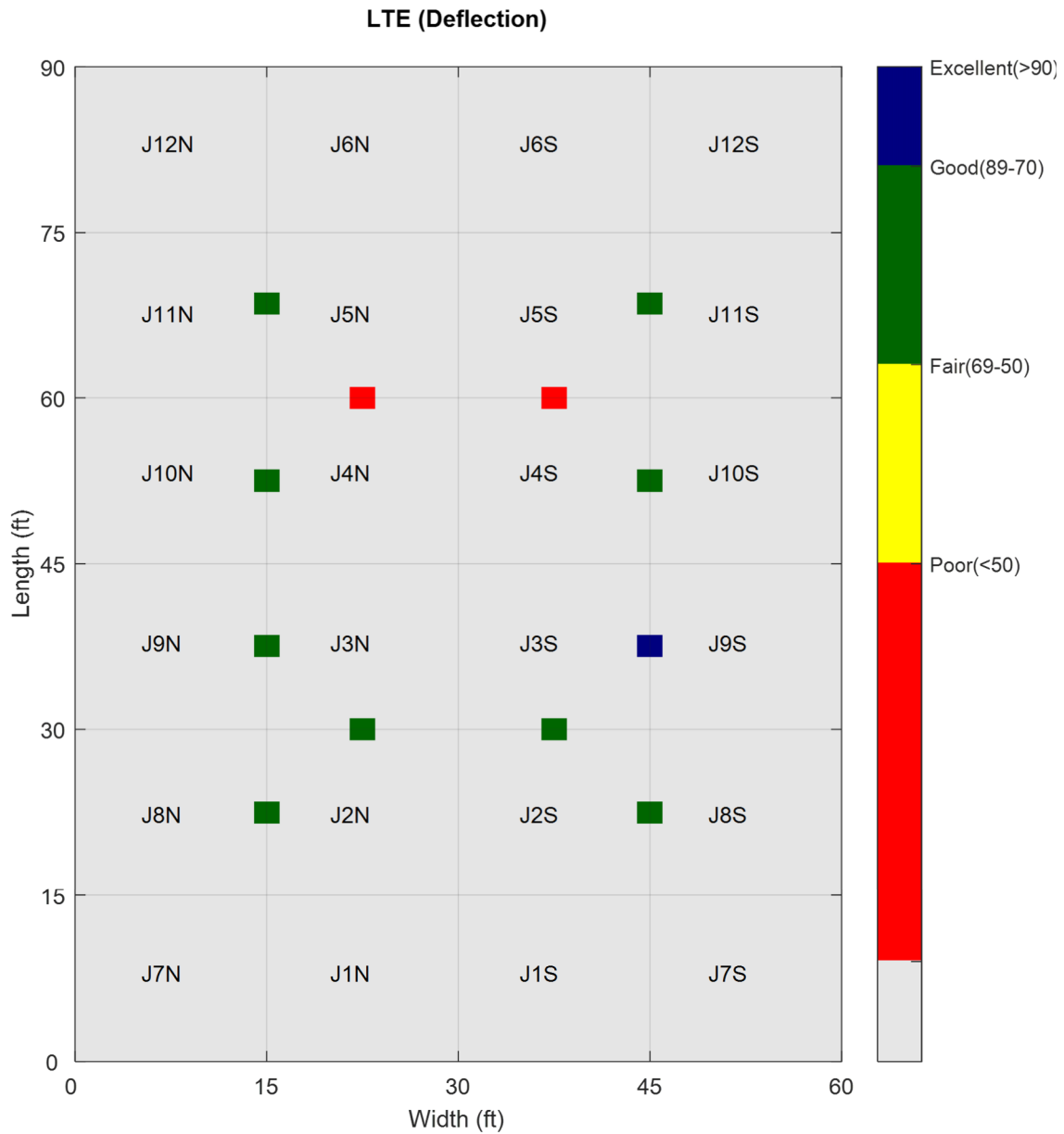


Figure 24. LTE_{δ} Levels Prior to Traffic (After Seating Load)

5.1.3 JOINT STIFFNESS

Deflection data from HWD testing were used to calculate joint stiffness following the method of Byrum et al. (2011). Figure 25 shows the schematic of an HWD setup with the load plate positioned at the slab edge such that the center of the plate and the second geophone are equidistant from the joint. The second geophone is 12 inches from the load plate center and the last geophone is 72 inches from the load plate center (66 inches from the joint opening). The vertical shear displacement is simply the difference between the deflections on the two sides of the joint. In this

setup, D_{-6} designates for deflections measured at the center of the load plate, and D_6 and D_{66} refer to the deflections at the second and last geophones, respectively.

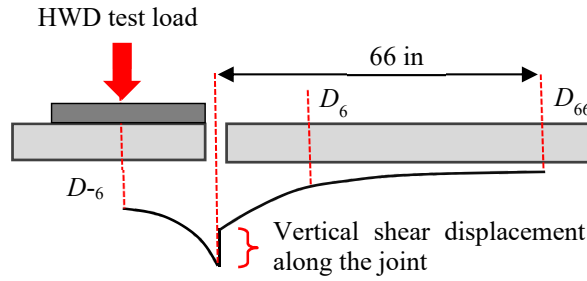


Figure 25. Schematic of HWD Test for Joint Stiffness Calculation

Equation (4), proposed by Byrum et al. in 2011, was used to determine the joint stiffness (k_J) based on the HWD deflections (4):

$$k_J = P(LTE_\delta) / [(1 + LTE_\delta)(D_{-6} - D_6)(1 + i\%) \Omega(66 + 60D_{66}/(D_6 - D_{66}))] \quad (4)$$

where, LTE_δ is the deflection-based LTE , $i\%$ is the percentage increase factor for projecting the sensor readings out to the joint line, and Ω is an unknown function that converts an assumed simplified linearly approximated shear area into the true shear area. In this study, the value of Ω was set equal to 1.0.

LTE_δ values can be used to estimate the joint stiffness using the following relationships (5, 6):

$$LTE_\delta = \frac{1}{1 + \log^{-1} \left[\frac{0.214 - 0.183 \left(\frac{\varepsilon}{\ell} \right) - \log(f)}{1.18} \right]} \quad (5)$$

$$\log(f) = \left[0.434829 \left(\frac{\varepsilon}{\ell} \right) - 1.23556 \right] \log \left(\frac{1}{LTE_\delta} - 1 \right) + 0.295205 \quad (6)$$

$$LTE_\delta = \frac{100\%}{1 + 1.2 \left(\frac{AGG_{tot}}{k\ell} \right)^{-0.849}} \quad (7)$$

$$LTE_\delta = 100 \left(1 - \left\{ 1 - \frac{1}{1 + \log^{-1} \left[\left(0.214 - 0.183 \frac{a}{\ell} - \log \left(\frac{AGG_{tot}}{k\ell} \right) - R \right) / 1.18 \right]} \right\} \right) \quad (8)$$

where:

$$f = q_0 / k\ell;$$

q_0 = joint stiffness, lb./in./in.;

ε = wheel load radius, in.;

ℓ = pavement radius of relative stiffness, in.;

k = the modulus of subgrade reaction, pci;
 AGG_{tot} = total joint stiffness, lb./in./in.; and
 R = residual dowel action factor.

Equations (5) and (6) assume “two infinite slabs connected by one infinitely long joint.” Equation (5) was referred to by Byrum et al. (4) as the “ LTE_{δ} regression for the Skarlatos/Ioannides Solution,” and was originally presented by Ioannides and Hammons (1996). As implemented, the known variables in this expression are plate radius, slab thickness, slab modulus, and measured joint stiffnesses k_j . The unknown variable is the modulus of subgrade reaction k , which can be obtained through matrix regression (4):

$$[Measured\ LTE_{\delta}] = [Skarlatos/Ioannides\ LTE_{\delta}\ as\ f(best - fit\ k\ell)] + [error] \quad (9)$$

A second form, expressed in Equation (6), was referred to by Byrum et al. as the “ $\log(f)$ regression for the Skarlatos/Ioannides solution.” Similar to the first form, it is used to find a best-fit k -value from matrix regression, given known values of slab thickness and modulus, and measured joint stiffnesses k_j (4):

$$\left[\log \left\{ \frac{(FWD\ stiffness)}{(best - fit\ k\ell)} \right\} \right] = [Skarlatos/Ioannides\ \log(f)] + [error] \quad (10)$$

Equation (7) was proposed by Croveti in 1994 (6) to compute joint stiffness directly from LTE_{δ} when other variables such as slab modulus, modulus of subgrade reaction, etc., are known.

There is no difference between total joint stiffness and joint stiffness. In equation (7) Croveti (1994) named ‘Total Joint Stiffness, AGG_{tot} ’, instead of ‘joint stiffness’. Later, Zollinger proposed a modified form of equation (using AGG_{tot}) to account for steel and crack-face bending moment transfer effects in addition to aggregate-interlock (Equation (8)).

In this study, calculated values from Equation (4) were considered as measured stiffness values, while values obtained from Equations (5) to (7) were considered as predicted only for the advanced analysis in Section 7.2.2.2.

5.2 PAVEMENT PERFORMANCE

5.2.1 DISTRESS MAPPING

Daily distress surveys were conducted in accordance with ASTM D5340 (7). Distresses were outlined with chalk and measured using a tape measure. Surveys recorded changes to existing distresses and any new distresses. Visual distress surveys were documented in two ways: a scale map and a written log. The distress map shows all distresses to scale and keys each distress to a wander sequence number, station number, and slab ID. Figure 26 shows a small part of the distress map. Distresses are numbered for reference to the written log. The wander width is delimited by the greyed out area. The full length of the map is best viewed by scrolling on a computer screen due to the long aspect ratio of the test pavement. Appendix C contains all CC8 Phase 3 distress maps.

The written log records all the distress information chronologically. Figure 27 is a screenshot of part of the log. The log includes the date, pass number, type of distress, distress number (which can be cross-referenced to the distress map), the location of the distress, and any relevant notes. The notes may indicate changes to existing distresses, severity levels, merging of multiple previously identified distresses, etc. Appendix D contains the complete log.

Some minor surface cracks on the north side that were observed prior to the start of the traffic test were recorded in the baseline distress survey. Some of these cracks were directly above embedded concrete strain gages (EGs). Over the course of the traffic test, more isolated, tight surface cracks appeared on the north pavement. These isolated cracks tended to develop in a random pattern in the interiors of slabs and did not appear to be load-related. In general, the north test item developed more structural distress, developed distresses earlier, and failed earlier than the south test item. On both north and south test items, corner breaks were the dominant structural distress.

5.2.2 STRUCTURAL CONDITION INDEX (SCI)

Regular pavement condition monitoring was a key element of the joint comparison traffic test. The structural condition of the test pavement was quantified by means of the SCI. SCI is a modification of the Pavement Condition Index (PCI) for airports (rigid) method following ASTM D 5340 (7). Like PCI, SCI is based on visual inspection of the pavement surface and identification of standard distresses. However, in the SCI only distresses related to structural loading are counted, while environmental and construction/material-related distresses are disregarded. In the field, pavements are divided into “sample units,” and a subset of sample units is then randomly selected for inspection. Due to the small size of the test area, the south and north side were initially considered to constitute two separate sample units, and 100% of the slabs in each unit (i.e.; twelve slabs) were inspected for the survey.

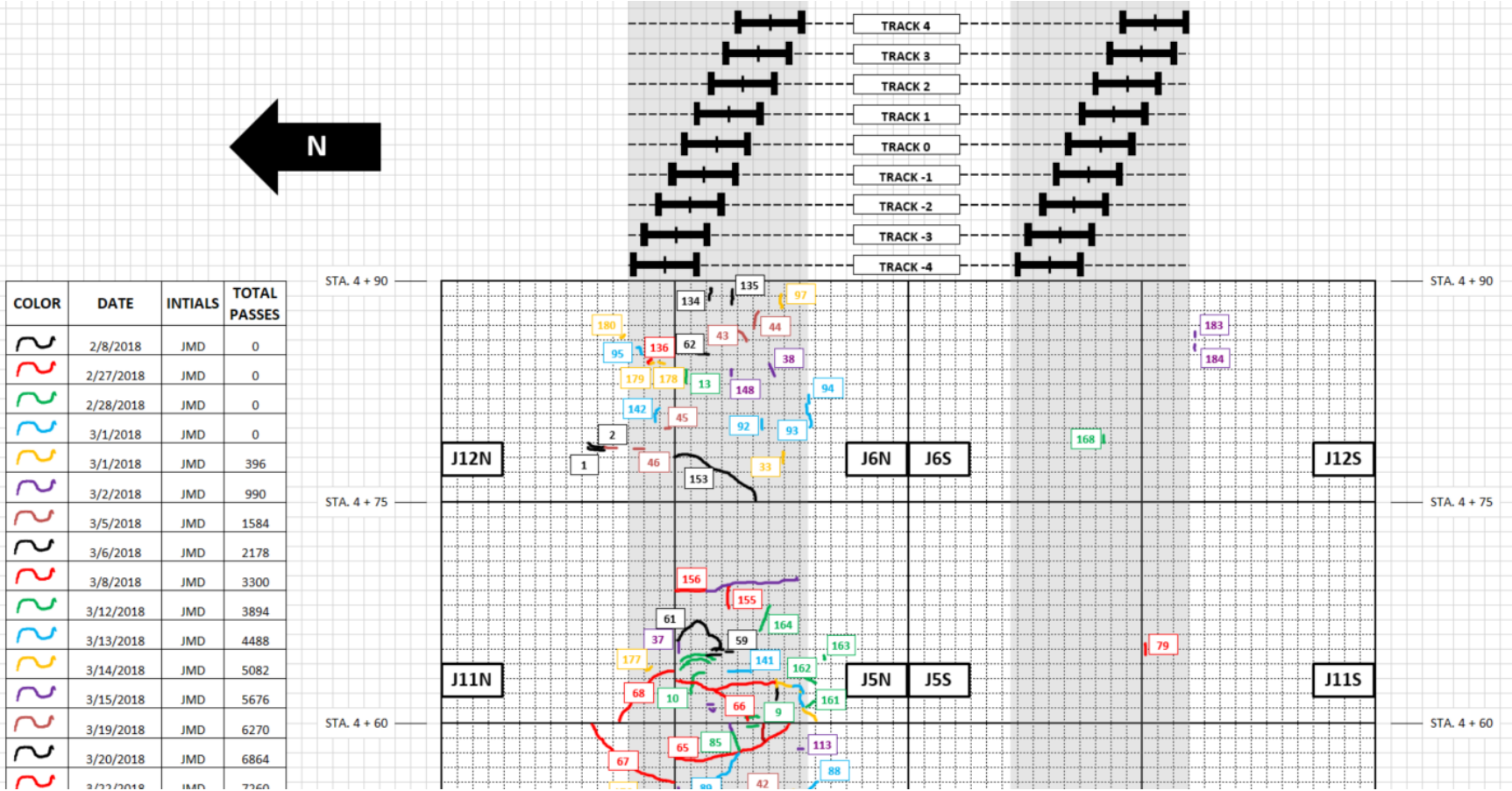


Figure 26. Sample Distress Map (portion)

DATE	TOTAL PASSES		DAILY PASSES	DISTRESS							NOTES	
	NORTH	SOUTH		DESCRIPTION	NO.	LOCATION						
						X AXIS (in.)			Y AXIS (in.)			SLAB
					WEST	MIDDLE	EAST	INITIAL	END			
2/8/2018	0	0	0	Shrinkage Crack	1		43		55	68	J12N	Pre-seating loads.
2/8/2018	0	0	0	Shrinkage Crack	2		45		55	68	J12N	Pre-seating loads.
2/27/2018	0	0	0	Shrinkage Crack	3	13		19	111	120	J1N	Post seating loads.
2/28/2018	0	0	0	Shrinkage Crack	4		11		41	47	J1N	Post 50 kips initial ramp-up loads.
2/28/2018	0	0	0	Shrinkage Crack	5		29		31	49	J1N	Post 50 kips initial ramp-up loads.
2/28/2018	0	0	0	Shrinkage Crack	6	49		58	170	170	J2N	Post 50 kips initial ramp-up loads.
2/28/2018	0	0	0	Shrinkage Crack	7	156		170	122	122	J3N	Post 50 kips initial ramp-up loads.
2/28/2018	0	0	0	Shrinkage Crack	8		177		116	124	J4N	Post 50 kips initial ramp-up loads. Over embedded sensor.
2/28/2018	0	0	0	Shrinkage Crack	9		3		115	125	J5N	Post 50 kips initial ramp-up loads. Over embedded sensor.
2/28/2018	0	0	0	Shrinkage Crack	10	24		41	157	168	J5N	Post 50 kips initial ramp-up loads.
2/28/2018	0	0	0	Shrinkage Crack	11	44		50	155	176	J5N	Post 50 kips initial ramp-up loads.
2/28/2018	0	0	0	Shrinkage Crack	12	49		54	149	176	J5N	Post 50 kips initial ramp-up loads.
2/28/2018	0	0	0	Shrinkage Crack	13	96		108	170	170	J5N	Post 50 kips initial ramp-up loads.
3/1/2018	0	0	0	Shrinkage Crack	14	152		157	160	163	J1N	Post all ramp-up loads.
3/1/2018	0	0	0	Shrinkage Crack	15	118		147	149	149	J2N	Post all ramp-up loads.

Figure 27. Sample Log (portion)

Because some surface cracks appeared prior to the start of traffic testing (see 5.2.1), two parallel sets of SCI values were calculated. The first set, designated “standard SCI,” considered pre-existing cracks. The second set, designated “corrected SCI,” excluded these cracks. Table 7 presents both sets of SCI estimates, considering each test lane (north and south) as an independent sample unit. The number of passes and wander patterns completed are given as cumulative values. After 74 days, traffic was terminated on the north side. Thus, data from day 75 to 80 in Table 7 correspond to the south side only. Due to the consideration of pre-existing cracks, the “standard SCI” values in Table 7 are initially lower than the “corrected SCI.” However, as expected, both sets of SCI values eventually converge. For the north test item, the convergence occurred after only three days of traffic whereas for the south test item, it occurred after six days of traffic.

Figure 28 shows the drop in SCI for both test pavements over the course of trafficking. Evidently, the north pavement deteriorated at a faster rate than did the south. The number of vehicle passes required to achieve similar levels of deterioration at the end of traffic was 45,738 for the south, but only 16,698 for the north.

The slabs were divided into 4 subgroups, as illustrated in Figure 3 (see section 2.1). The four subgroups (North-West, South-West, North-East, and South-East) each represented a different combination of longitudinal and transverse joint types. Considering the likelihood of different deterioration trends in these four subgroups, “corrected SCI” values were calculated treating each subgroup as a separate sample unit. Table 8 lists “corrected SCI” broken out by subgroup. Figure 29 shows the drop in SCI for the four subgroups over the course of trafficking. Figure 29 confirms that the North-East subgroup (undoweled transverse and doweled longitudinal joints, exhibited the poorest performance among the four subgroups, reaching the failure point (SCI=80) at approximately 3,000 passes. By contrast, the South-East subgroup (undoweled transverse and sinewave shaped longitudinal keyway joints) exhibited the best performance, requiring more than 16,000 passes to reach an SCI value below 80. After dropping to 79, the SCI of the South-East subgroup remained constant throughout the rest of Traffic Test-Stage I. The North-West and South-West subgroups exhibited apparently similar performance. However, the narrow transition at the west end of the test area may have affected the performance of these two subgroups.

Table 7. Structural Condition Index (SCI) Considering the North and South Sample Units

Day No	Date	Passes	Wanders	Traffic Stage	Standard SCI		Corrected SCI	
					North	South	North	South
0	3/1/2018	0	0	I	91	98	100	100
1	3/1/2018	396	6	I	91	97	93	98
2	3/2/2018	990	15	I	91	97	92	98
3	3/5/2018	1584	24	I	91	97	91	98
4	3/6/2018	2178	33	I	91	97	91	98
5	3/7/2018	2706	41	I	91	97	91	98
6	3/8/2018	3300	50	I	73	88	73	88
7	3/12/2018	3894	59	I	61	82	61	82
8	3/13/2018	4488	68	I	56	82	56	82
9	3/14/2018	5082	77	I	51	76	51	76
10	3/15/2018	5676	86	I	51	74	51	74
11	3/19/2018	6270	95	I	51	74	51	74
12	3/20/2018	6864	104	I	51	74	51	74
13	3/22/2018	7260	110	I	51	74	51	74
14	3/26/2018	7854	119	I	39	74	39	74
15	3/27/2018	8448	128	I	28	74	28	74
16	3/28/2018	9042	137	I	28	69	28	69
17	3/29/2018	9636	146	I	26	69	26	69
18	4/2/2018	10164	154	I	26	69	26	69
19	4/3/2018	10758	163	I	22	69	22	69
20	4/4/2018	11352	172	I	22	59	22	59
21	4/5/2018	11946	181	I	22	50	22	50
22	4/9/2018	12540	190	I	22	37	22	37
23	4/10/2018	13134	199	I	22	37	22	37
24	4/19/2018	13728	208	I	18	37	18	37
25	4/23/2018	14322	217	I	18	37	18	37
26	4/24/2018	14916	226	I	18	37	18	37
27	4/25/2018	15510	235	I	18	37	18	37
28	4/26/2018	16104	244	I	18	37	18	37
29	4/30/2018	16698	253	I	14	37	14	37
30	5/1/2018	17292	262	I	14	34	14	34
31	5/2/2018	17886	271	I	14	34	14	34
32	5/3/2018	18348	278	I	14	34	14	34
33	5/7/2018	18942	287	I	14	34	14	34
34	5/8/2018	19536	296	I	14	34	14	34
35	5/9/2018	20130	305	I	14	34	14	34
36	5/14/2018	20724	314	I	14	34	14	34
37	5/16/2018	21318	323	I	14	34	14	34
38	5/17/2018	21912	332	I	14	34	14	34
39	5/21/2018	22506	341	I	14	34	14	34
40	5/22/2018	23100	350	I	14	34	14	34
41	5/23/2018	23694	359	I	14	34	14	34
42	5/24/2018	24288	368	I	14	34	14	34

Day No	Date	Passes	Wanders	Traffic Stage	Standard SCI		Corrected SCI	
					North	South	North	South
43	5/29/2018	24882	377	I	14	34	14	34
44	5/30/2018	25476	386	I	14	34	14	34
45	5/31/2018	26070	395	I	14	34	14	34
46	6/4/2018	26664	404	I	14	34	14	34
47	6/5/2018	27258	413	I	14	34	14	34
48	6/6/2018	27852	422	I	14	34	14	34
49	6/7/2018	28446	431	I	14	34	14	34
50	6/11/2018	29040	440	I	14	34	14	34
51	6/12/2018	29634	449	I	14	34	14	34
52	6/13/2018	30228	458	I	14	34	14	34
53	6/14/2018	30822	467	I	14	34	14	34
54	6/18/2018	31416	476	I	14	34	14	34
55	6/19/2018	32010	485	I	14	34	14	34
56	6/20/2018	32604	494	I	14	34	14	34
57	6/21/2018	33132	502	I	14	34	14	34
58	6/25/2018	33726	511	I	14	34	14	34
59	6/26/2018	34320	520	I	14	34	14	34
60	6/27/2018	34914	529	I	14	34	14	34
61	6/28/2018	35508	538	I	14	34	14	34
62	7/2/2018	35966	545	I	14	34	14	34
63	7/23/2018	36564	554	I	14	34	14	34
64	7/24/2018	37158	563	I	14	34	14	34
65	7/25/2018	37752	572	I	14	34	14	34
66	7/26/2018	38346	581	I	14	34	14	34
67	7/30/2018	38940	590	I	14	34	14	34
68	7/31/2018	39534	599	I	14	34	14	34
69	8/1/2018	40128	608	I	14	34	14	34
70	8/2/2018	40722	617	I	14	34	14	34
71	8/6/2018	41316	626	I	14	34	14	34
72	8/7/2018	41910	635	I	14	34	14	34
73	8/8/2018	42504	644	I	14	34	14	34
74	8/9/2018	42702	647	I	14	34	14	34
75	10/29/2018	42712	647	II		34		34
75	10/29/2018	42838	649	II		34		34
76	11/1/2018	43362	657	II		24		24
77	11/5/2018	43956	666	II		18		18
78	11/6/2018	44550	675	II		17		17
79	11/7/2018	45144	684	II		14		14
80	11/8/2018	45738	693	II		12		12

**Traffic on the north side was terminated after 74 days. Number of passes and wanders from that point on correspond to the south side only*

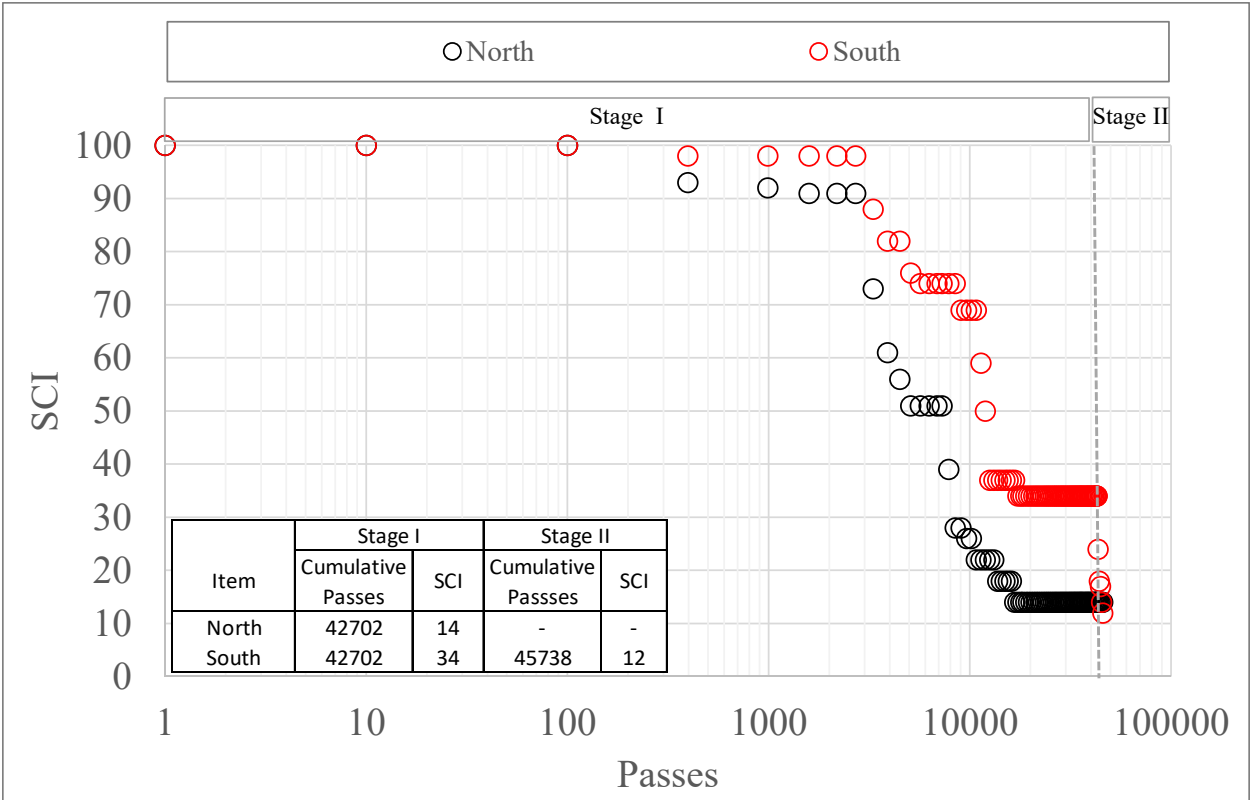


Figure 28. Joint Comparison SCI versus Passes Considering the North and South Sample Units

Table 8. Structural Condition Index (SCI) Considering Four Sample Units

Day No	Date	Passes	Wanders	Traffic Stage	Corrected SCI Modified by Slab Group			
					North-West	South-West	North-East	South-East
0	3/1/2018	0	0	I	100	100	100	100
1	3/1/2018	396	6	I	92	100	95	97
2	3/2/2018	990	15	I	92	100	92	97
3	3/5/2018	1584	24	I	92	100	90	97
4	3/6/2018	2178	33	I	92	100	90	97
5	3/7/2018	2706	41	I	92	100	90	97
6	3/8/2018	3300	50	I	92	82	60	92
7	3/12/2018	3894	59	I	92	82	45	92
8	3/13/2018	4488	68	I	92	82	36	92
9	3/14/2018	5082	77	I	82	66	36	92
10	3/15/2018	5676	86	I	82	61	36	92
11	3/19/2018	6270	95	I	68	61	36	92
12	3/20/2018	6864	104	I	68	61	36	92
13	3/22/2018	7260	110	I	68	61	36	92
14	3/26/2018	7854	119	I	51	61	36	92
15	3/27/2018	8448	128	I	24	61	36	92
16	3/28/2018	9042	137	I	24	56	36	92
17	3/29/2018	9636	146	I	21	56	36	92
18	4/2/2018	10164	154	I	21	56	36	92
19	4/3/2018	10758	163	I	21	56	31	92
20	4/4/2018	11352	172	I	21	40	31	92
21	4/5/2018	11946	181	I	21	29	31	90
22	4/9/2018	12540	190	I	21	13	31	90
23	4/10/2018	13134	199	I	21	13	31	90
24	4/19/2018	13728	208	I	16	13	31	87
25	4/23/2018	14322	217	I	16	13	31	87
26	4/24/2018	14916	226	I	16	13	31	87
27	4/25/2018	15510	235	I	16	13	31	87
28	4/26/2018	16104	244	I	16	13	31	87
29	4/30/2018	16698	253	I	16	13	19	87
30	5/1/2018	17292	262	I	16	13	19	79
31	5/2/2018	17886	271	I	16	13	19	79
32	5/3/2018	18348	278	I	16	13	19	79
33	5/7/2018	18942	287	I	16	13	19	79
34	5/8/2018	19536	296	I	16	13	19	79
35	5/9/2018	20130	305	I	16	13	19	79
36	5/14/2018	20724	314	I	16	13	19	79
37	5/16/2018	21318	323	I	16	13	16	79
38	5/17/2018	21912	332	I	16	13	16	79
39	5/21/2018	22506	341	I	16	13	16	79
40	5/22/2018	23100	350	I	16	13	16	79
41	5/23/2018	23694	359	I	16	13	16	79
42	5/24/2018	24288	368	I	16	13	16	79

Day No	Date	Passes	Wanders	Traffic Stage	Corrected SCI Modified by Slab Group			
					North-West	South-West	North-East	South-East
43	5/29/2018	24882	377	I	16	13	16	79
44	5/30/2018	25476	386	I	16	13	16	79
45	5/31/2018	26070	395	I	16	13	16	79
46	6/4/2018	26664	404	I	16	13	16	79
47	6/5/2018	27258	413	I	16	13	16	79
48	6/6/2018	27852	422	I	16	13	16	79
49	6/7/2018	28446	431	I	16	13	16	79
50	6/11/2018	29040	440	I	16	13	16	79
51	6/12/2018	29634	449	I	16	13	16	79
52	6/13/2018	30228	458	I	16	13	16	79
53	6/14/2018	30822	467	I	16	13	16	79
54	6/18/2018	31416	476	I	16	13	16	79
55	6/19/2018	32010	485	I	16	13	16	79
56	6/20/2018	32604	494	I	16	13	16	79
57	6/21/2018	33132	502	I	16	13	16	79
58	6/25/2018	33726	511	I	16	13	16	79
59	6/26/2018	34320	520	I	16	13	16	79
60	6/27/2018	34914	529	I	16	13	16	79
61	6/28/2018	35508	538	I	16	13	16	79
62	7/2/2018	35966	545	I	16	13	16	79
63	7/23/2018	36564	554	I	16	13	16	79
64	7/24/2018	37158	563	I	16	13	16	79
65	7/25/2018	37752	572	I	16	13	16	79
66	7/26/2018	38346	581	I	16	13	16	79
67	7/30/2018	38940	590	I	16	13	16	79
68	7/31/2018	39534	599	I	16	13	16	79
69	8/1/2018	40128	608	I	16	13	16	79
70	8/2/2018	40722	617	I	16	13	16	79
71	8/6/2018	41316	626	I	16	13	16	79
72	8/7/2018	41910	635	I	16	13	16	79
73	8/8/2018	42504	644	I	16	13	16	79
74	8/9/2018	42702	647	I	16	13	16	79
75	10/29/2018	42712	647	II		13		79
75	10/29/2018	42838	649	II		13		79
76	11/1/2018	43362	657	II		9		64
77	11/5/2018	43956	666	II		3		57
78	11/6/2018	44550	675	II		3		52
79	11/7/2018	45144	684	II		2		52
80	11/8/2018	45738	693	II		2		41

**Traffic on the north side was terminated after 74 days. Number of passes and wanders from that point on correspond to the south side only*

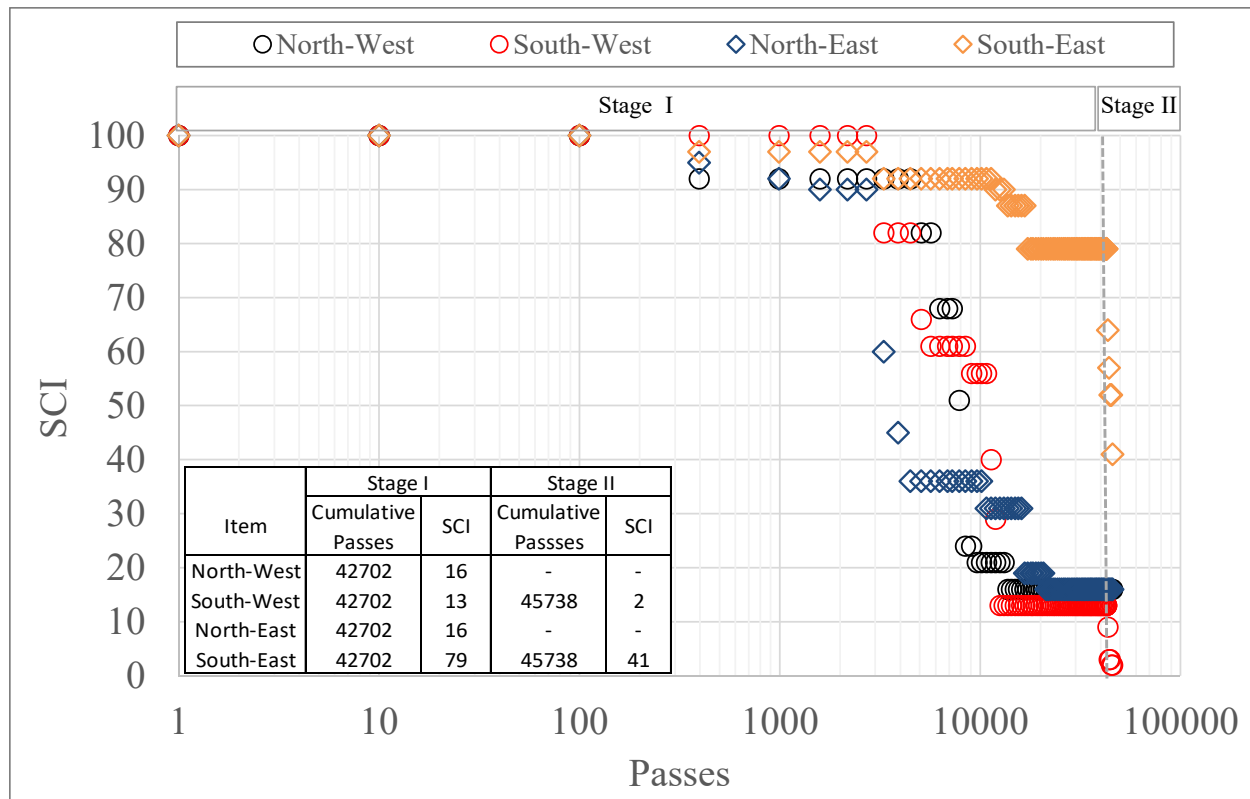


Figure 29. Joint Comparison SCI versus Passes Considering Four Sample Units

5.2.3 CRACK DENSITY (CD)

The crack density parameter (CD) was used in addition to the SCI, to quantify the performance of the pavement (8, 9). The procedure for computing CD was:

1. Using the scale distress map, subdivide each slab into 225 discrete units, each with an area of one square foot (i.e., 15×15 squares).
2. By counting squares, determine CD as the percent of discrete squares in which any amount of cracking was observed. Figure 30 illustrates a corner break on slab J10N (red) that extends over ten discrete units (green). Hence, the CD for slab J10N was estimated as $(10/225) \times 100 = 4.4\%$.

The accuracy of crack density calculations increases with the number of discrete units per slab. The Construction Cycle 4 (CC4) data analysis settled on 100 discrete units as a reasonable compromise between accuracy and time efficiency when the slab size was 12.5×12.5 ft. (10, 11). To improve on that level of accuracy for the larger slab size (15×15 ft.) of CC8, the number of divisions was increased to $15 \times 15 = 225$. Table 9 (for north slabs) and Table 10 (for south slabs) list the computed CD values. Table 10 includes CD values from both Stage I and Stage II.

Estimates of average CD for each of the four subgroups in Figure 3 (North-West, South-West, North-East, and South-East) were calculated. Figure 31 shows the growth in average CD for each subgroup over the course of traffic. The performance ranking was: SE (best), SW, NW, NE. These

rankings were consistent with the SCI (Figure 29). However, CD data captured a much clearer separation between slab groups than SCI data. The SW subgroup showed better performance in terms of CD than the NW subgroup.

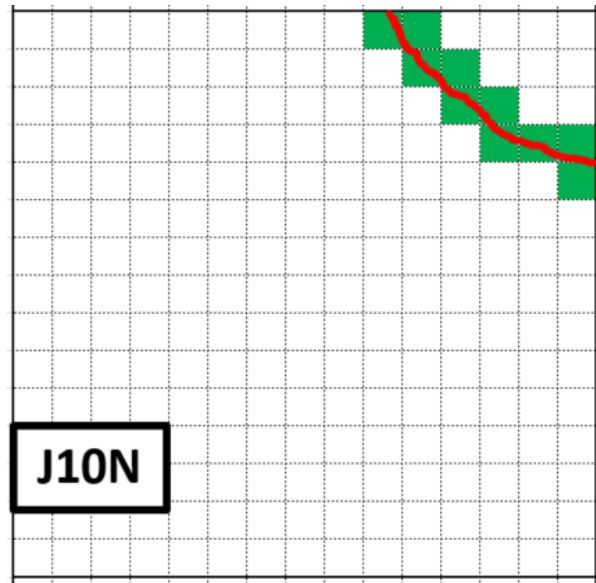


Figure 30. Example of Crack Density Calculation for Slab J10N (March 13, 2018)

Table 9. Crack Density for All Slabs (North)

Date	Pass#	Wander	SCI	CD*	CD per Slab											
					J1	J2	J3	J4	J5	J6	J7	J8	J9	J10	J11	J12
3/1/18	0	0	100	0.0	0	0	0	0	0	0	0	0	0	0	0	0
3/1/18	396	6	93	2.0	4	4	7	3	4	1	0	0	0	0	0	1
3/2/18	990	15	92	2.2	4	4	8	3	4	2	0	0	0	0	0	1
3/6/18	2178	33	91	3.4	7	4	9	7	8	4	0	0	0	0	0	3
3/8/18	3300	50	73	4.3	7	4	9	11	9	4	0	0	0	3	3	3
3/12/18	3894	59	61	4.6	7	4	11	12	9	4	0	0	0	3	3	3
3/13/18	4488	68	56	5.3	7	4	11	16	11	6	0	0	0	3	3	3
3/14/18	5082	77	51	5.6	7	4	11	16	11	7	2	0	0	3	3	3
3/15/18	5676	86	51	6.0	8	5	12	18	11	7	2	0	0	3	3	3
3/19/18	6270	95	51	6.5	8	9	12	18	11	7	3	0	0	5	3	3
3/20/18	6864	104	51	6.8	8	9	14	18	11	9	3	0	0	5	3	3
3/26/18	7854	119	39	7.0	8	9	15	18	11	9	3	0	0	5	3	4
3/27/18	8448	128	28	7.1	8	9	15	18	12	9	3	0	0	5	3	4
3/28/18	9042	137	28	7.1	8	9	15	18	12	9	3	0	0	5	3	4
3/29/18	9636	146	26	7.1	8	9	15	18	12	9	3	0	0	5	3	4
4/2/18	10164	154	26	7.4	10	9	16	18	12	9	3	0	0	5	3	4
4/3/18	10758	163	22	7.7	10	9	16	18	12	13	3	0	0	5	3	4
4/4/18	11352	172	22	8.0	10	9	17	18	14	13	3	0	0	5	3	4
4/5/18	11946	181	22	8.3	10	10	17	18	16	13	3	0	0	5	3	4
4/9/18	12540	190	22	8.3	11	10	17	18	16	13	3	0	0	5	3	4
4/10/18	13134	199	22	8.5	11	10	17	19	16	13	3	0	0	5	3	5
4/19/18	13728	208	18	8.5	11	10	17	19	16	13	3	0	0	5	3	5
4/23/18	14322	217	18	8.5	11	10	17	19	16	13	3	0	0	5	3	5
4/26/18	16104	244	18	8.6	11	10	17	19	16	13	4	0	0	5	3	5
4/30/18	16698	253	14	8.7	11	10	17	19	16	13	4	0	0	6	3	5
5/1/18	17792	270	14	8.7	11	10	17	19	16	13	4	0	0	6	3	5
5/7/18	18942	287	14	8.7	11	10	17	19	16	13	4	0	0	6	3	5
5/9/18	20130	305	14	8.7	11	10	18	19	16	13	4	0	0	6	3	5
6/21/18	33132	502	14	8.8	11	10	18	19	16	13	4	1	0	6	3	5
6/25/18	33726	511	14	8.8	11	10	18	19	16	13	4	1	0	6	3	5
6/26/18	34320	520	14	8.8	11	10	18	19	16	13	4	1	0	6	3	5
6/27/18	34914	529	14	8.8	11	10	18	19	16	13	4	1	0	6	3	5
6/28/18	35508	538	14	8.8	11	10	18	19	16	13	4	1	0	6	3	5
7/2/18	35966	544.9	14	8.8	11	10	18	19	16	13	4	1	0	6	3	5
7/23/18	36564	554	14	8.8	11	10	18	19	16	13	4	1	0	6	3	5
7/24/18	37158	563	14	8.8	11	10	18	19	16	13	4	1	0	6	3	5
7/25/18	37752	572	14	8.8	11	10	18	19	16	13	4	1	0	6	3	5
7/26/18	38346	581	14	8.8	11	10	18	19	16	13	4	1	0	6	3	5
7/30/18	38940	590	14	8.8	11	10	18	19	16	13	4	1	0	6	3	5
7/31/18	39534	599	14	8.8	11	10	18	19	16	13	4	1	0	6	3	5
8/1/18	40128	608	14	8.8	11	10	18	19	16	13	4	1	0	6	3	5
8/2/18	40722	617	14	8.8	11	10	18	19	16	13	4	1	0	6	3	5
8/6/18	41316	626	14	8.8	11	10	18	19	16	13	4	1	0	6	3	5
8/7/18	41910	635	14	8.8	11	10	18	19	16	13	4	1	0	6	3	5
8/8/18	42504	644	14	8.8	11	10	18	19	16	13	4	1	0	6	3	5
8/9/18	42702	647	14	8.8	11	10	18	19	16	13	4	1	0	6	3	5

*CD average of all slabs on the north side

Table 10. Crack Density for All Slabs (South)

Date	Pass #	Wander	SCI	CD*	CD per Slab											
					J1	J2	J3	J4	J5	J6	J7	J8	J9	J10	J11	J12
3/1/18	0	0	100	0.0	0	0	0	0	0	0	0	0	0	0	0	0
3/1/18	396	6	98	0.1	1	0	0	0	0	0	0	0	0	0	0	0
3/2/18	990	15	98	0.1	1	0	0	0	0	0	0	0	0	0	0	0
3/6/18	2178	33	98	0.2	1	0	0	0	0	0	0	0	0	1	0	0
3/8/18	3300	50	88	0.7	4	0	0	0	0	0	3	0	0	1	1	0
3/12/18	3894	59	82	1.1	8	0	0	0	0	0	3	0	0	1	1	0
3/13/18	4488	68	82	1.1	8	0	0	0	0	0	3	0	0	1	1	0
3/14/18	5082	77	76	1.3	8	1	1	0	0	0	3	0	0	1	1	0
3/15/18	5676	86	74	1.4	8	1	1	0	0	0	4	0	0	1	1	0
3/19/18	6270	95	74	1.4	8	1	1	0	0	0	4	0	0	1	1	0
3/20/18	6864	104	74	1.4	8	1	1	0	0	0	4	0	0	1	1	0
3/26/18	7854	119	74	1.4	8	1	1	0	0	0	4	0	0	1	1	0
3/27/18	8448	128	74	1.5	8	1	2	0	0	0	4	0	0	1	1	0
3/28/18	9042	137	69	1.7	11	1	2	0	0	0	4	0	0	1	1	0
3/29/18	9636	146	69	1.7	11	1	2	0	0	0	4	0	0	1	1	0
4/2/18	10164	154	69	1.7	12	1	2	0	0	0	4	0	0	1	1	0
4/3/18	10758	163	69	1.7	12	1	2	0	0	0	4	0	0	1	1	0
4/4/18	11352	172	59	1.9	12	2	2	0	0	0	4	0	0	1	1	0
4/5/18	11946	181	50	2.1	12	2	2	0	0	0	4	0	0	3	1	0
4/9/18	12540	190	37	2.2	13	2	2	0	0	0	4	0	0	3	1	0
4/10/18	13134	199	37	2.2	13	2	2	0	0	0	4	0	0	3	1	0
4/19/18	13728	208	37	2.3	13	2	2	0	0	0	5	0	0	3	1	1
4/23/18	14322	217	37	2.4	13	2	2	0	0	0	6	0	0	3	1	1
4/26/18	16104	244	37	2.4	13	2	2	0	0	0	6	0	0	3	1	1
4/30/18	16698	253	37	2.4	13	2	2	0	0	0	6	0	0	3	1	1
5/1/18	17792	270	34	2.6	13	2	2	0	0	0	6	0	0	3	4	1
5/7/18	18942	287	34	2.7	13	2	2	1	0	0	6	0	0	3	4	1
5/9/18	20130	305	34	2.9	13	3	2	1	0	0	6	0	1	3	4	1
6/21/18	33132	502	34	2.9	13	3	2	1	0	0	6	0	1	3	4	1
6/25/18	33726	511	34	2.9	13	3	2	1	0	0	6	0	1	3	4	1
6/26/18	34320	520	34	2.9	13	3	2	1	0	0	6	0	1	3	4	1
6/27/18	34914	529	34	2.9	13	3	2	1	0	0	6	0	1	3	4	1
6/28/18	35508	538	34	2.9	13	3	2	1	0	0	6	0	1	3	4	1
7/2/18	35966	544.9	34	2.9	13	3	2	1	0	0	6	0	1	3	4	1
7/23/18	36564	554	34	2.9	13	3	2	1	0	0	6	0	1	3	4	1
7/24/18	37158	563	34	2.9	13	3	2	1	0	0	6	0	1	3	4	1
7/25/18	37752	572	34	2.9	13	3	2	1	0	0	6	0	1	3	4	1
7/26/18	38346	581	34	2.9	13	3	2	1	0	0	6	0	1	3	4	1
7/30/18	38940	590	34	2.9	13	3	2	1	0	0	6	0	1	3	4	1
7/31/18	39534	599	34	2.9	13	3	2	1	0	0	6	0	1	3	4	1
8/1/18	40128	608	34	2.9	13	3	2	1	0	0	6	0	1	3	4	1
8/2/18	40722	617	34	2.9	13	3	2	1	0	0	6	0	1	3	4	1
8/6/18	41316	626	34	2.9	13	3	2	1	0	0	6	0	1	3	4	1
8/7/18	41910	635	34	2.9	13	3	2	1	0	0	6	0	1	3	4	1
8/8/18	42504	644	34	2.9	13	3	2	1	0	0	6	0	1	3	4	1
8/9/18	42702	647	34	2.9	13	3	2	1	0	0	6	0	1	3	4	1
11/1/18	43362	657	24	3.6	13	3	3	1	1	0	8	0	1	6	4	3
11/5/18	43956	666	18	3.9	13	3	3	1	1	4	8	0	1	6	4	3
11/6/18	44550	675	17	4.8	15	3	3	8	1	4	8	0	1	6	6	3
11/7/18	45144	684	14	6.2	15	3	3	13	1	4	13	0	4	9	6	3
11/8/18	45738	693	12	6.4	18	3	3	13	1	4	13	0	4	9	6	3

*CD average of all slabs on the south side

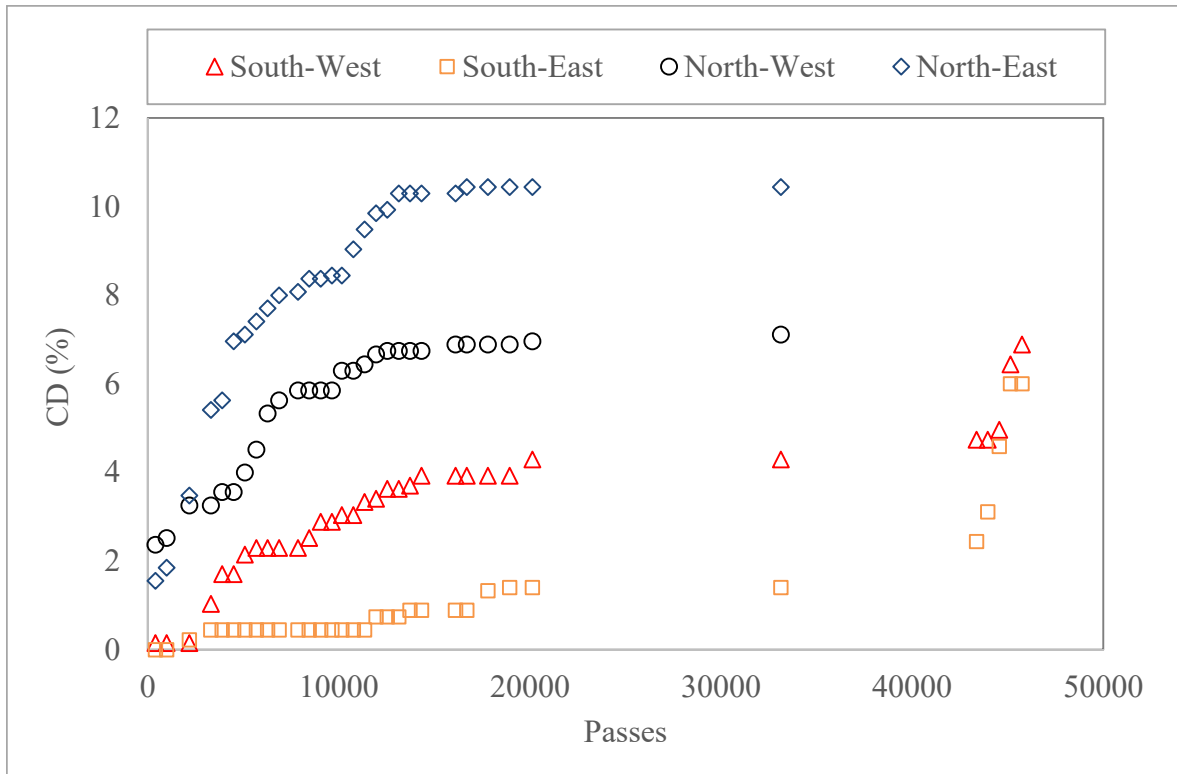


Figure 31. Development of CD for Four Subgroups

6. PRELIMINARY DATA ANALYSIS

6.1 JOINT DETERIORATION

Section 5.1 covered methods for evaluating joint performance, based on changes in LTE and joint stiffness (k_j). The data used are from two sources: in-pavement sensors and HWD deflection measurements. The following sections make use of those methods to analyze the deterioration of both transverse and longitudinal joints over the course of traffic.

6.1.1 IN-PAVEMENT SENSOR DATA

6.1.1.1 TRANSVERSE JOINTS

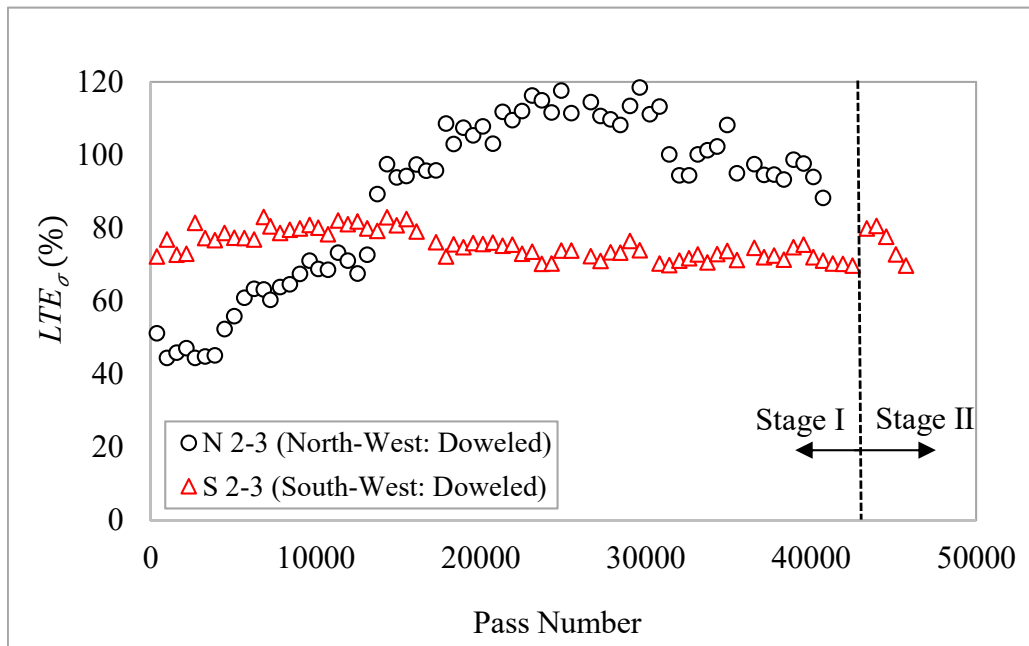
Stress-based Load Transfer Efficiency (LTE_σ)

Values of LTE_σ were calculated for transverse joints in the four subgroups. All data used correspond to track T1 (Figure 12) in the “east-to-west” travel direction. Figure 32(a) shows the trends for LTE_σ across doweled transverse contraction joints (NW and SW slab subgroups). Initially, all LTE_σ values were determined using the “Sensor Pair” approach (Section 5.1.1, Figure 20). From Figure 32(a), LTE_σ for joint S 2-3 (SW subgroup) varied in the range of 70-83%. For the NW subgroup, LTE_σ across joint N 2-3 exhibited a sudden increase after pass number 3,894,

and eventually apparently exceeded 100%. Rather than being indication of a healthy joint, LTE_{σ} values exceeding 100% indicate damage to either the sensor or its surrounding media.

Figure 32(b) plots the values of peak strains used to calculate LTE_{σ} across joint N 2-3. After 3,894 passes, the strains in the loaded slab J3N dropped by approximately 10 microstrains. However, in the unloaded slab J2N, the strain remained nearly constant. With additional traffic, peak strains in the loaded slab continued to decrease, which led to a gradual increase in LTE_{σ} to 72.7%. After pass 14,322, the recorded values of peak strain on opposite sides of the joint became nearly equal, resulting in apparent LTE_{σ} values approaching 100%. Between passes 17,889 and 34,914, the LTE_{σ} across joint N 2-3 frequently exceeded 100% (i.e., the strain measured in the unloaded slab exceeded that of the loaded slab). These anomalous strain readings may be associated with localized damage observed near the vicinity of EG-N-J-II-6 in the unloaded slab. Considering these observations and the apparent unreliability of EG-N-J-II-6, it was decided to use the “Geometric” (Single Sensor) approach for calculating LTE_{σ} across joint N 2-3. Table 11 summarizes the methods ultimately used to calculate both LTE_{σ} and LT_{σ} for each transverse joint.

Figure 33(a) and (b) plot LTE_{σ} as a function of pass number for doweled and undoweled transverse contraction joints, respectively. The LTE_{σ} values for joint N 2-3 have been recalculated using the geometric method. In Stage I, LTE_{σ} for doweled joints did not exhibit significant change with traffic. In Stage II, only the south test pavement received 3D loads. At the start of Stage II, the LTE_{σ} for joint S 2-3 increased by 10%, then decreased rapidly with Stage II traffic.



(a)

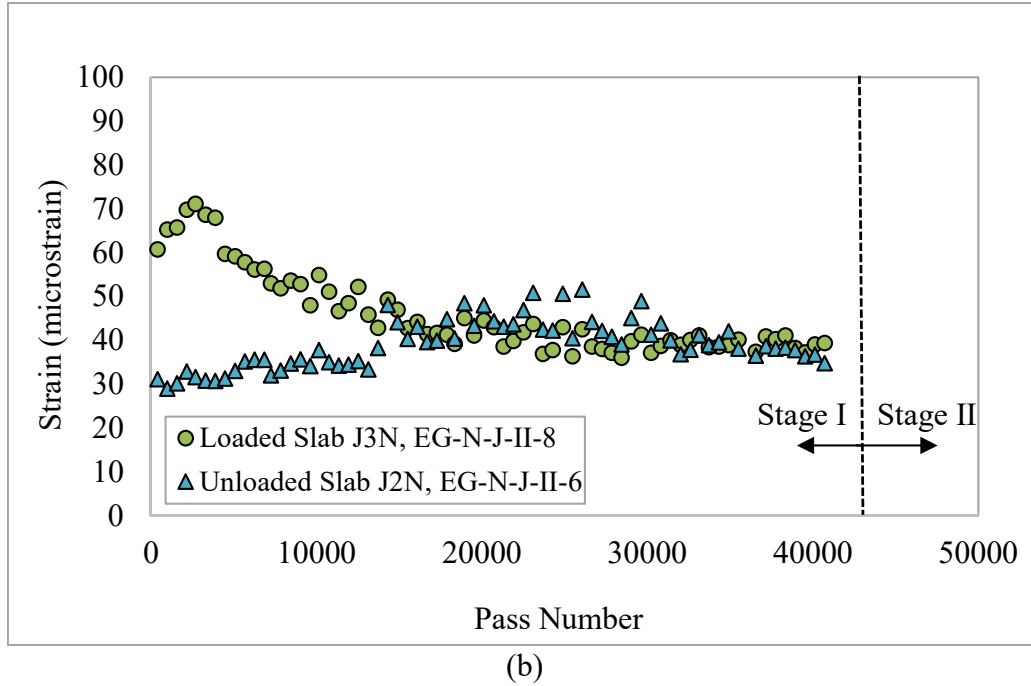


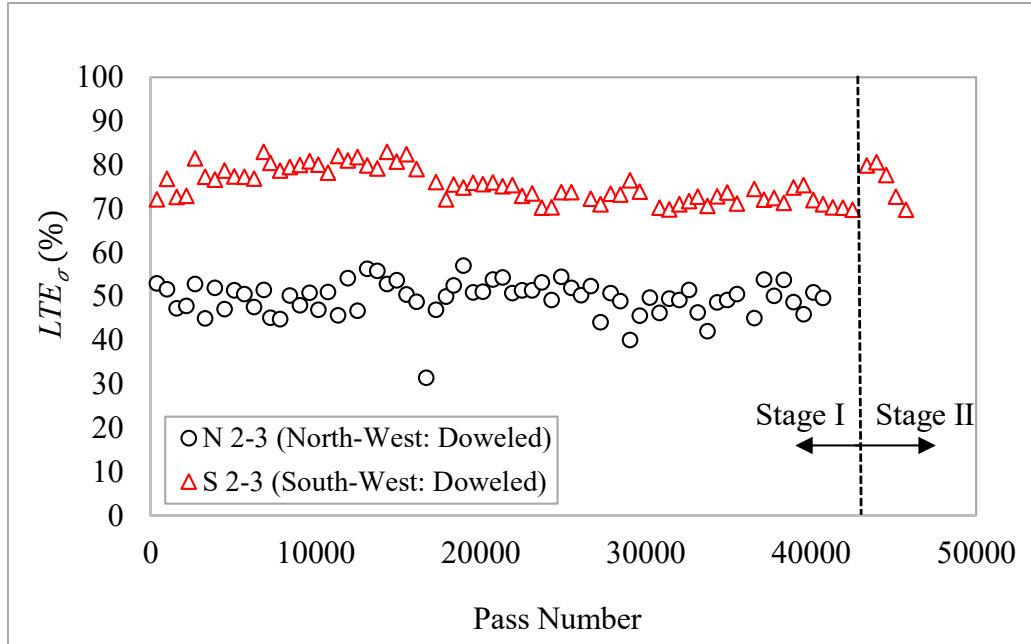
Figure 32. LTE_{σ} of Transverse Doweled Joints N 2-3 and S 2-3 Calculated by Sensor Pair Method, and Instrumentation Data for Joint N 2-3: (a) LTE_{σ} of Transverse Doweled Joints N 2-3 and S 2-3, and (b) Strains used for Calculation of LTE_{σ} in Joint N 2-3

Table 11. Calculation Approach for LTE_{σ} and LT_{σ} of Transverse and Longitudinal Joints

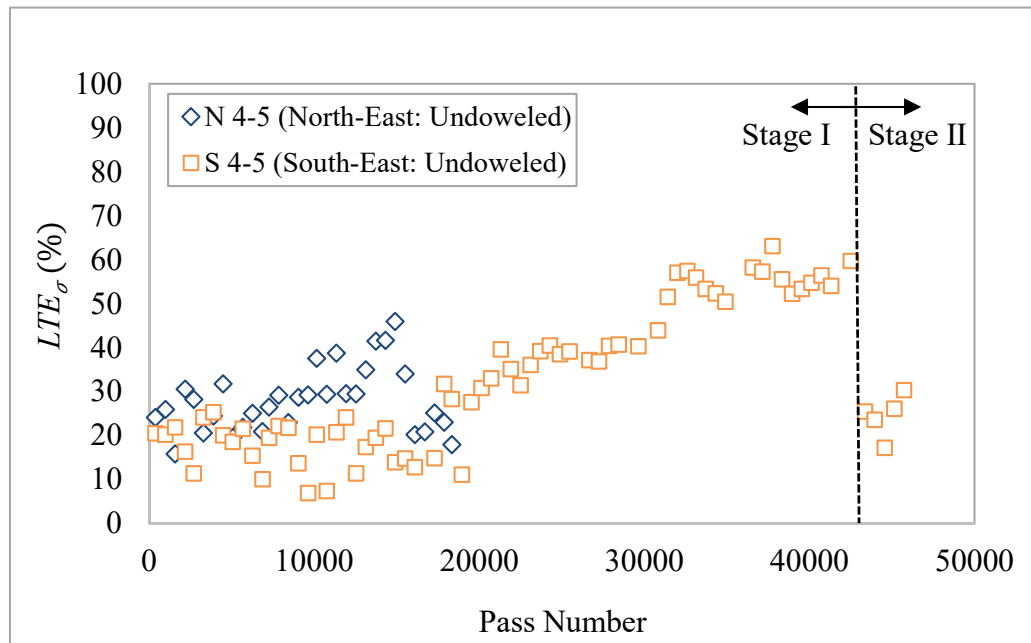
Slab Group	Transverse Joints				Longitudinal Joints			
	Joint ID	Loaded Slab	Unloaded Slab	Calculation Approach	Joint ID	Loaded Slab	Unloaded Slab	Calculation Approach
North-West	N 2-3	J3N	J2N	Geometric ¹	N 2-8 N 3-9	J8N J9N	J2N J3N	Sensor Pair Sensor Pair
North-East	N 4-5	J5N	J4N	Geometric	N 4-10 N 5-11	J10N J11N	J4N J5N	NA ² Sensor Pair
South-West	S 2-3	J3S	J2S	Sensor Pair	S 2-8 S 3-9	J8S J9S	J2S J3S	Sensor Pair Sensor Pair
South-East	S 4-5	J5S	J4S	Geometric	S 4-10 S 5-11	J10S J11S	J4S J5S	Sensor Pair Sensor Pair

¹ For joint N 2-3, the “Sensor Pair” approach was initially used. However, due to poor quality data from the bottom EG, it was ultimately decided to adopt the “Geometric” approach.

² For joint N 4-10, EG-N-J-II-14 in the unloaded Slab J4N was inactive and therefore, load transfer estimates were not possible.



(a)



(b)

Figure 33. LTE_{σ} of Transverse Joints from Instrumentation Data: (a) Doweled (N 2-3 by Geometric Method and S 2-3 by Sensor Pair Method), and (b) Undoweled (Geometric Method)

Figure 33b) shows the change in LTE_{σ} for undoweled contraction joints N 4-5 and S 4-5. The geometric method was used for N 4-5, with EG-N-J-II-18 data because EG-N-J-II-20 in slab J5N was not functional. No LTE_{σ} values for N 4-5 were calculated after pass 18,348, because at that point EG-N-J-II-18 also began showing signs of failure, with “unloaded” strain readings intermittently close to zero (Figure 34). After about 10,000 passes, N 4-5 exhibited a steady increase in apparent LTE_{σ} , followed by a sudden drop after pass number 14,916. This behavior was attributed to the increase in the severity of a corner break on slabs J4N and J5N. The corner break was first observed after 3,000 passes (March 8, 2018).

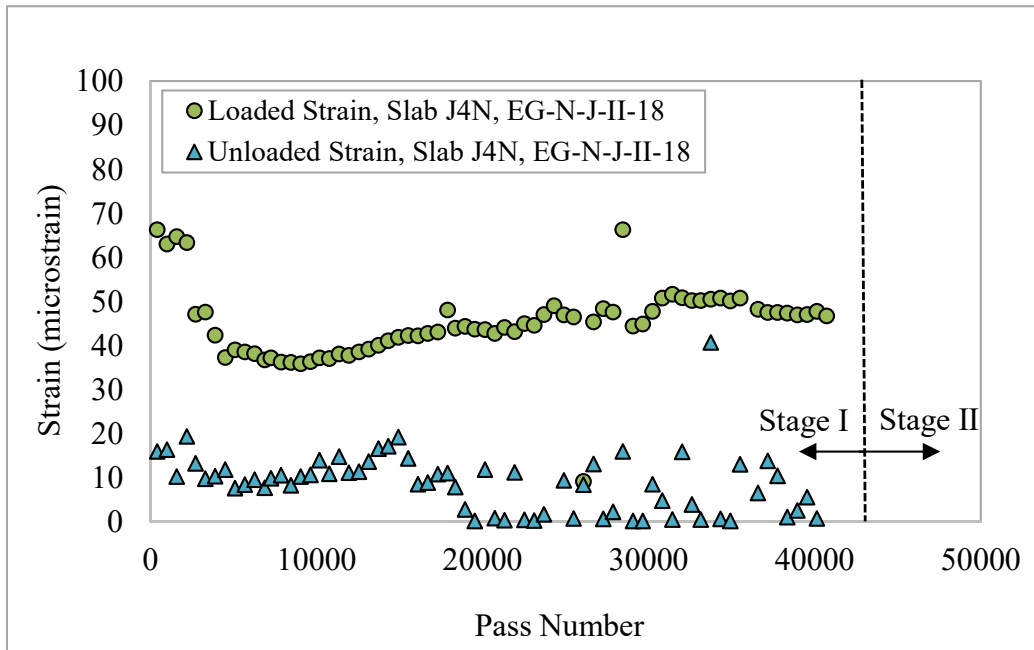


Figure 34. Loaded and Unloaded Strains (EG-N-J-II-18) used to Determine LTE_{σ} in Joint N 4-5

In Figure 33(b), LTE_{σ} for S 4-5 gradually increased to about 60% after pass number 19,536. This increase is attributed to thermal effects and corresponds to increasing slab temperature (Figure 35). Similarly, the approximately 30% drop in LTE_{σ} for S 4-5 at the start of Stage II is associated with temperature decrease.

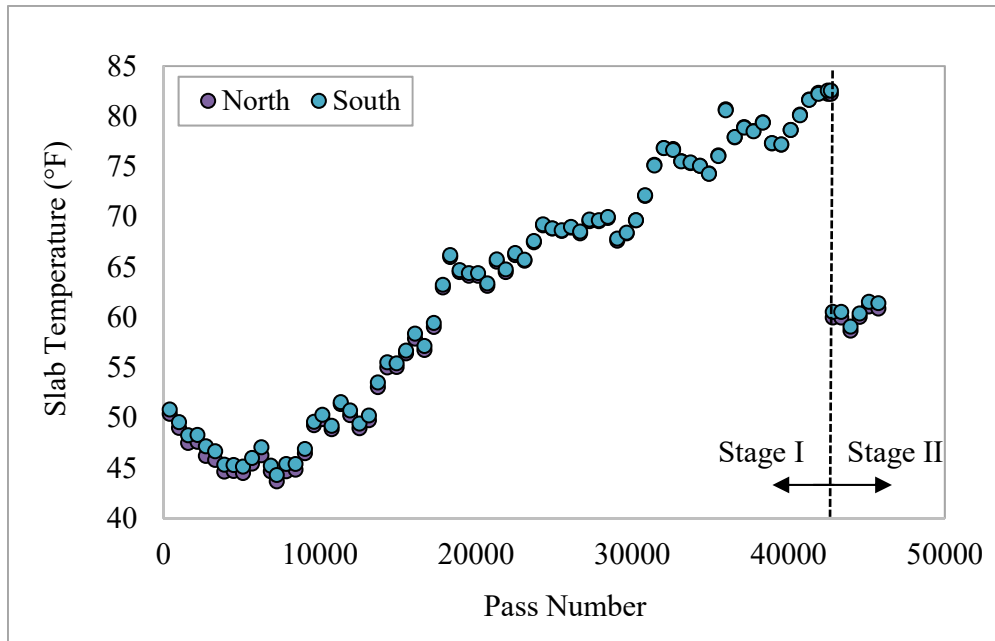
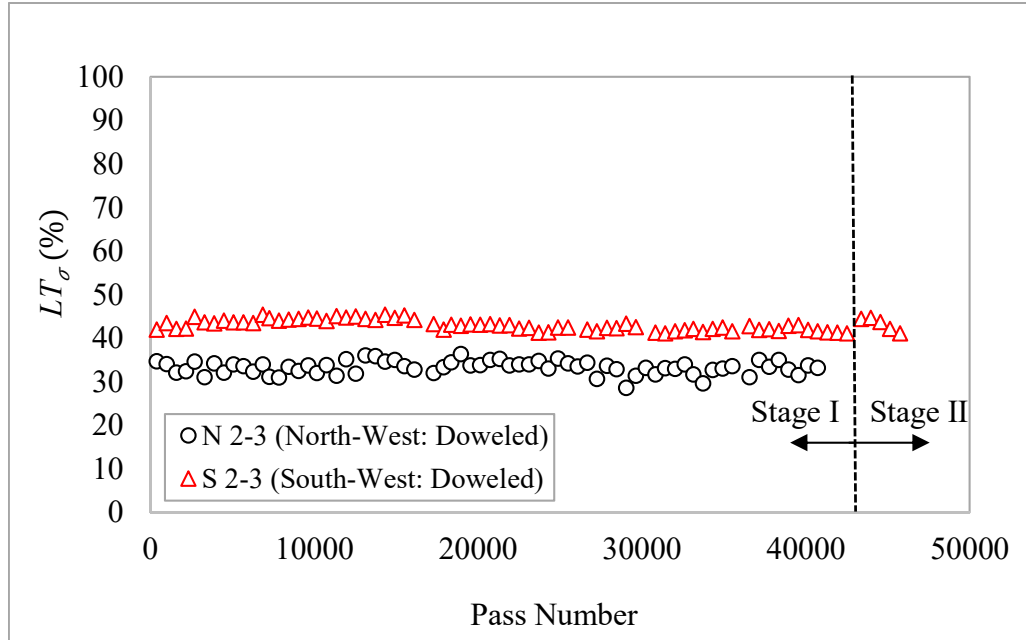


Figure 35. Change in Slab Temperature

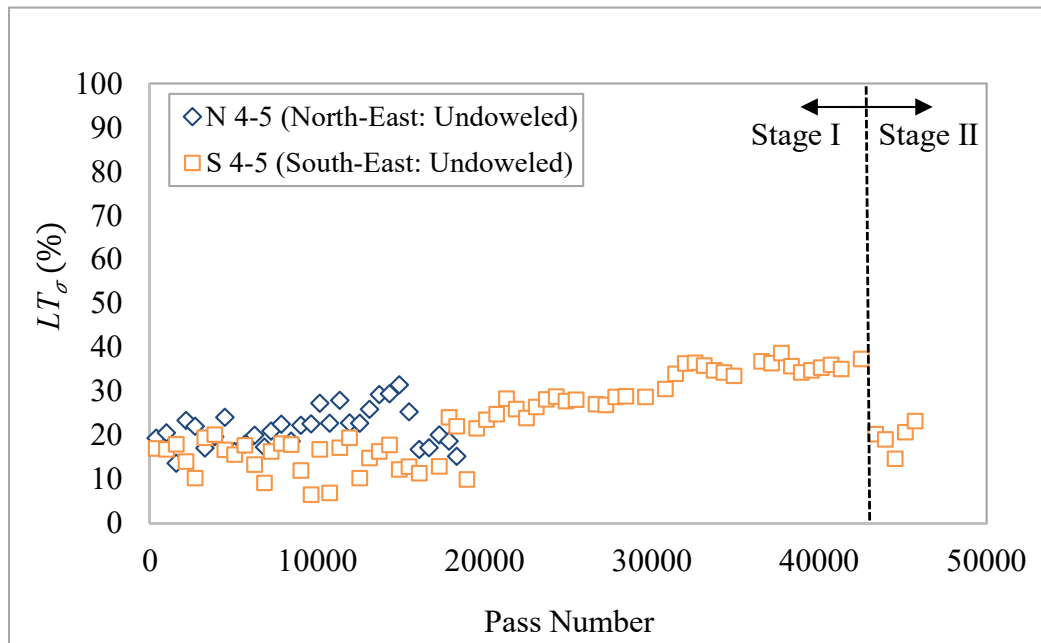
Stress-based Load Transfer (LT_σ)

FAARFIELD assumes that 25% of the edge stress is transferred across a joint from the loaded to the unloaded slab. However, the actual stress transfer mechanism is more complicated. Stress-based load transfer (LT_σ) was calculated daily during trafficking to evaluate stress transfer in the four slab subgroups. Initially, every attempt was made to calculate LT_σ for each transverse joint using the sensor pair method. However, this was not always possible for the reasons discussed in the previous subsection with respect to LTE_σ . For each joint, the method followed to calculate LT_σ was consistent with the LTE_σ calculation (see table 11).

Figure 36(a) and (b) plot LT_σ as a function of pass number for doweled and undoweled transverse contraction joints, respectively. In Figure 36(a), LT_σ for doweled joints is above 25% for both the NW and SW slab groups. For both groups, no significant degradation was observed over the course of the test. After the start of Stage II, LT_σ on the SW group increased by approximately 5%, then gradually decreased with Stage II traffic to a final value of 40%.



(a)



(b)

Figure 36. LT_{σ} of Transverse Joints from Instrumentation Data: (a) Doweled (N 2-3 by Geometric Method and S 2-3 by Sensor Pair Method), and (b) Undoweled (Geometric Method)

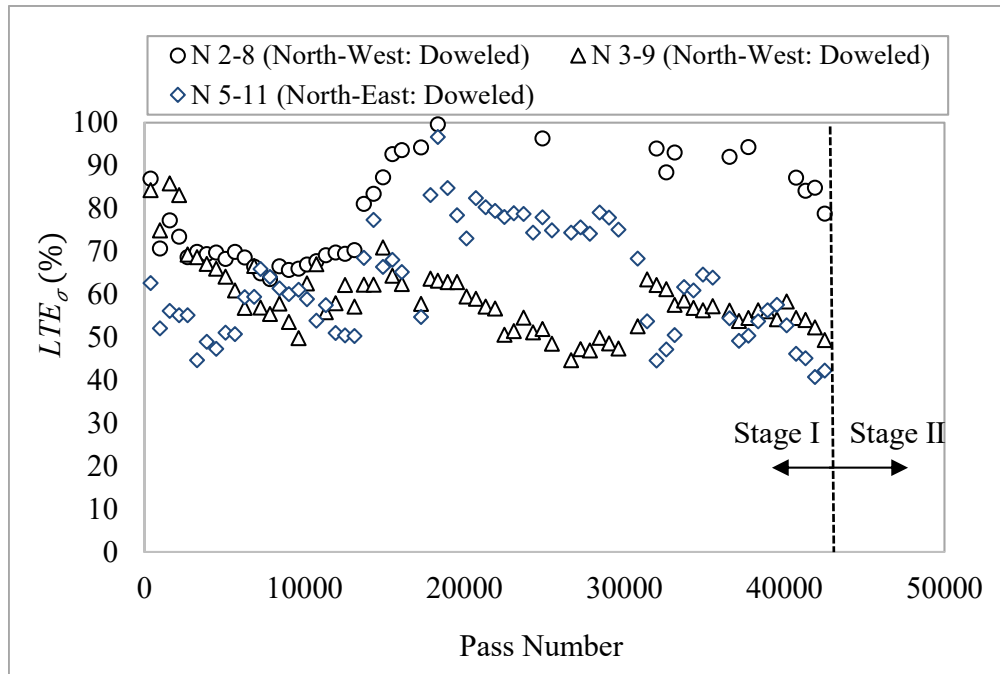
Figure 36(b) shows the change in LT_σ for undoweled contraction joints N 4-5 and S 4-5. In general, LT_σ values for undoweled joints were lower than for doweled joints. At the start of the test, LT_σ values for both N 4-5 and S 4-5 were below 25%. No LT_σ values were calculated for joint N 4-5 beyond pass 18,348, as discussed in the previous subsection. After approximately 19,000 passes, LT_σ for joint S 4-5 began to increase, corresponding to the increasing slab temperature (Figure 35). Similarly, the drop of approximately 20% in LT_σ for S 4-5 at the start of Stage II corresponds to the drop in slab temperature.

6.1.1.2 LONGITUDINAL JOINTS

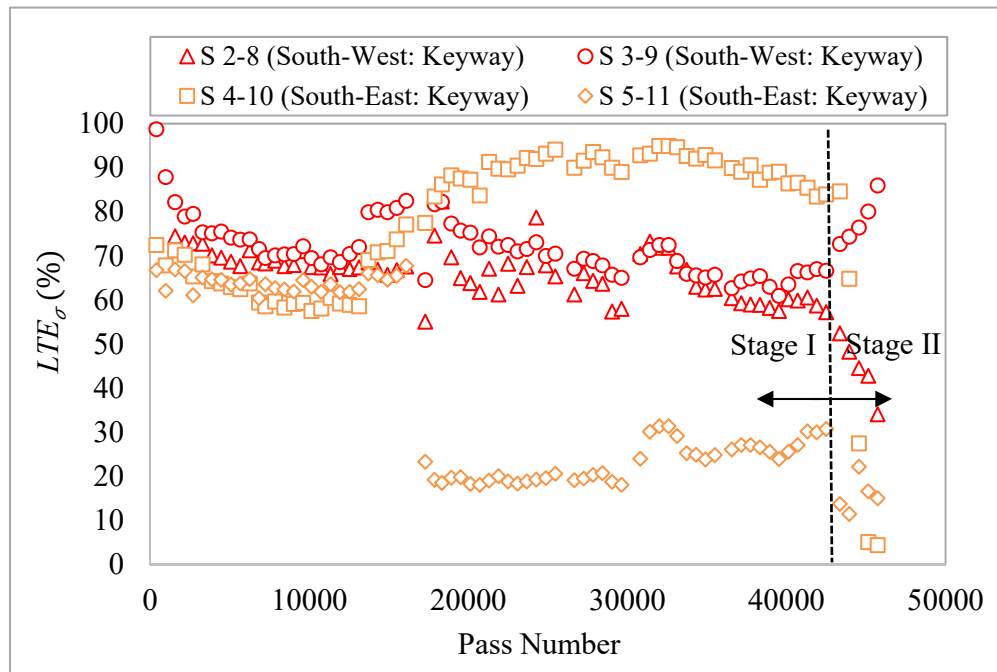
Stress-based Load Transfer Efficiency (LTE_σ)

Values of LTE_σ for longitudinal joints were calculated daily during the traffic phase. Figure 37(a) and (b) plot LTE_σ as a function of passes for doweled (NW and NE subgroups) and keyed (SW and SE subgroups) longitudinal joints, respectively. From Figure 37(a), the initial LTE_σ for joints N 2-8 and N 3-9 was approximately 85%, and slightly over 60% for joint N 5-11. Joint N 4-10 was instrumented, however the LTE_σ could not be determined due to EG-N-J-II-14 malfunctioning. For longitudinal joints (unlike transverse joints) both sides of the joint must have functioning strain gages; the geometric approach for computing LTE_σ from a single gage response cannot be used for longitudinal joints.

Initially, track L2 was such that only the outside tire was on the outside slab edge (Figure 12). After pass number 13,134, the position of track L2 was corrected to ensure that both wheels loaded the outside slab. Figure 37(a) shows decreasing LTE_σ for doweled longitudinal joints in the early stages of traffic. In the later stages of traffic, the observed trends were inconsistent. At the end of Stage I, joints N 3-9 and N 5-11 had similar LTE_σ values of approximately 45%, but the apparent LTE_σ for N 2-8 was much higher.



(a)



(b)

Figure 37. LTE_{σ} of Longitudinal Joints from Instrumentation Data Calculated by Sensor Pair Method: (a) Doweled, and (b) Keyway

From Figure 37(b), the LTE_{σ} for keyed longitudinal joints was approximately 70% in the early stages of traffic. Initially, joint S 3-9 exhibited 100% LTE_{σ} , but shook down within the first several hundred passes. Similar to the doweled construction joints, the keyed joints exhibited an increase in apparent LTE_{σ} following the position adjustment of track L2. The sudden drop in LTE_{σ} for joint S 5-11 is associated with a corner break on slab J11S after pass 16,104.

Plots of the underlying strains are useful to help explain the inconsistencies observed in LTE_{σ} trends. Figure 38(a) and (b) show strain trends for gear track L2, for doweled joints on the north test item. Figure 38(a) shows a gradual decrease in strain on both loaded and unloaded slabs for longitudinal joint N 2-8, after initial shakedown. The change in track L2 manifests as a drop in EG-N-J-II-4 strain after pass 13,134, corresponding to an increase in LTE_{σ} for joint N 2-8, as seen in Figure 37(a). The strain in the unloaded slab did not exhibit a similar drop. During traffic, shrinkage cracks were the only surface distresses observed in slab J2N. No surface distresses were observed on slab J8N during traffic. Figure 38(b) shows the changes in strains on both loaded and unloaded slabs for longitudinal joint N 5-11 (track L2). Both strains decrease steadily with traffic up to pass 3,300. At pass 3,300, corner breaks appeared on slabs J5N and J11N. Thus, in this case there was a correspondence between observed surface distress and the beginnings of inconsistencies in LTE_{σ} . Again, at pass 13,134 there was a slight drop in the EG-N-J-II-24 strain reading corresponding to the realignment of track L2, but no similar change in EG-N-J-II-22.

Figure 39(a) and (b) show the strain trends for gear track L2, for keyed joints on the south test item. Figure 39(a) shows an apparent drop in the strain on the loaded side of joint S 4-10 at 13,314 passes, corresponding to the change in track L2. Figure 39(b) shows an increase in strain on the loaded side of joint S 5-11 at 17,292 passes, corresponding to the appearance of a corner break on Slab J11S. However, for S 5-11 there was no obvious response to the change in track L2 in the strain gage readings.

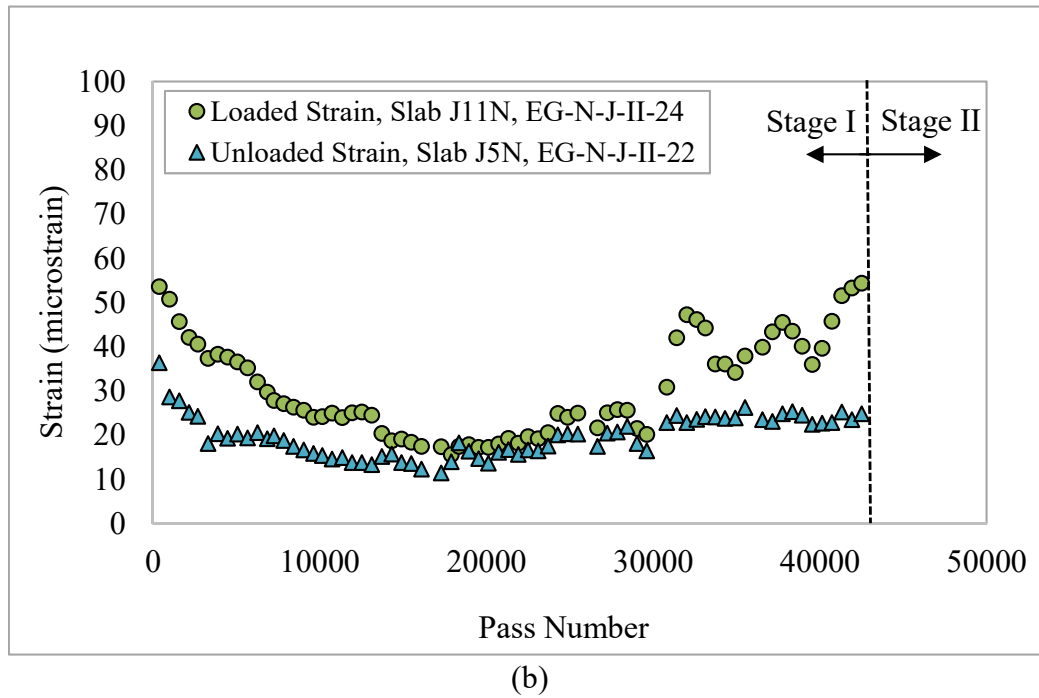
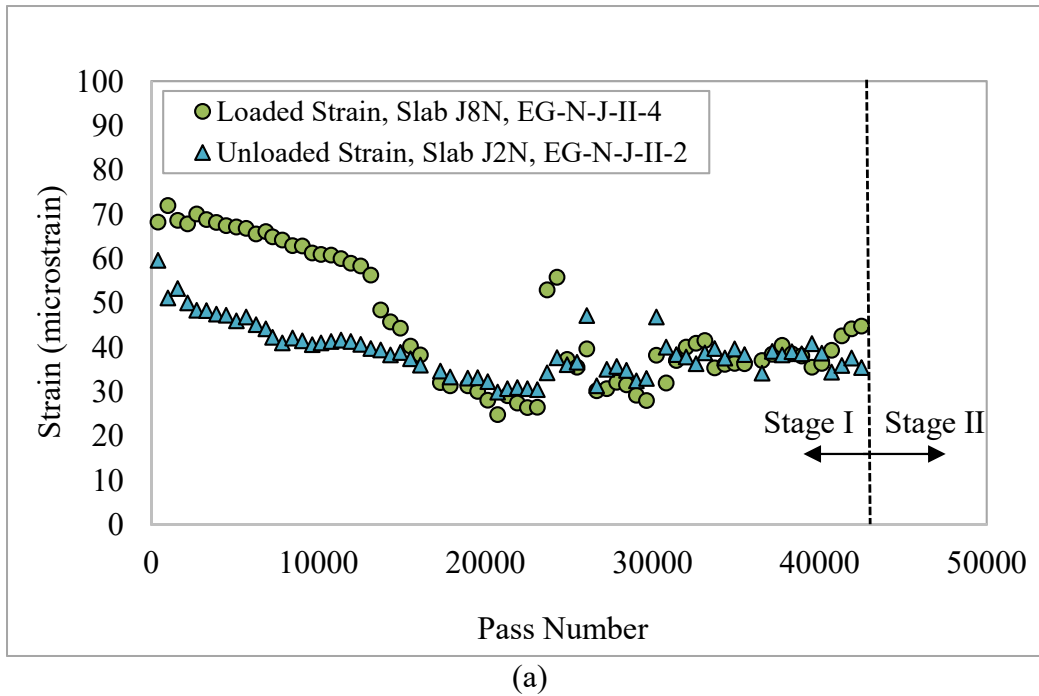
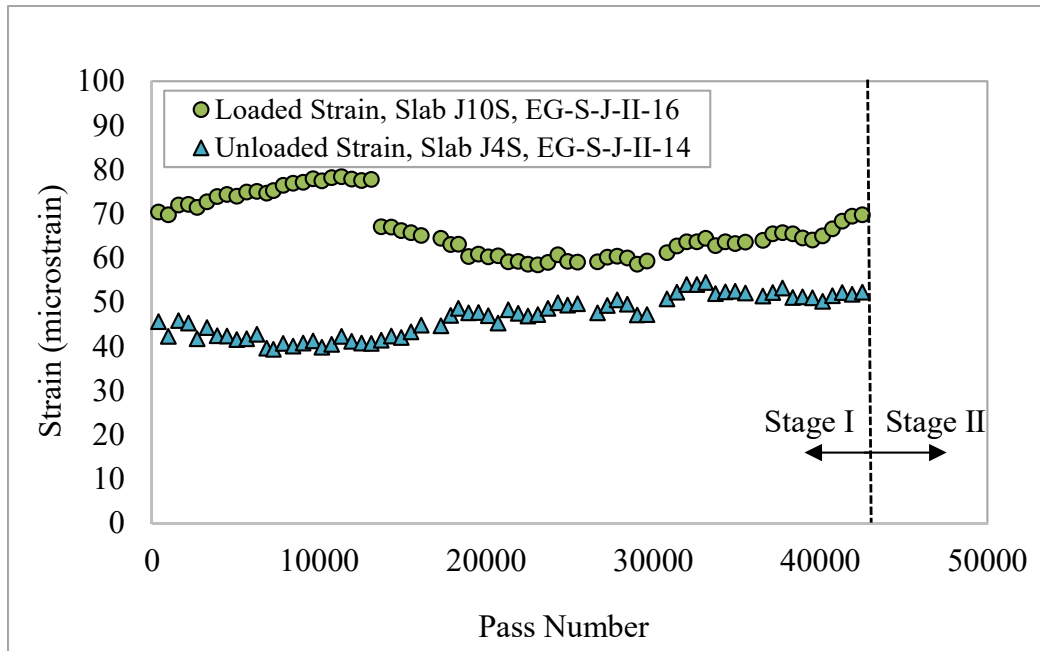
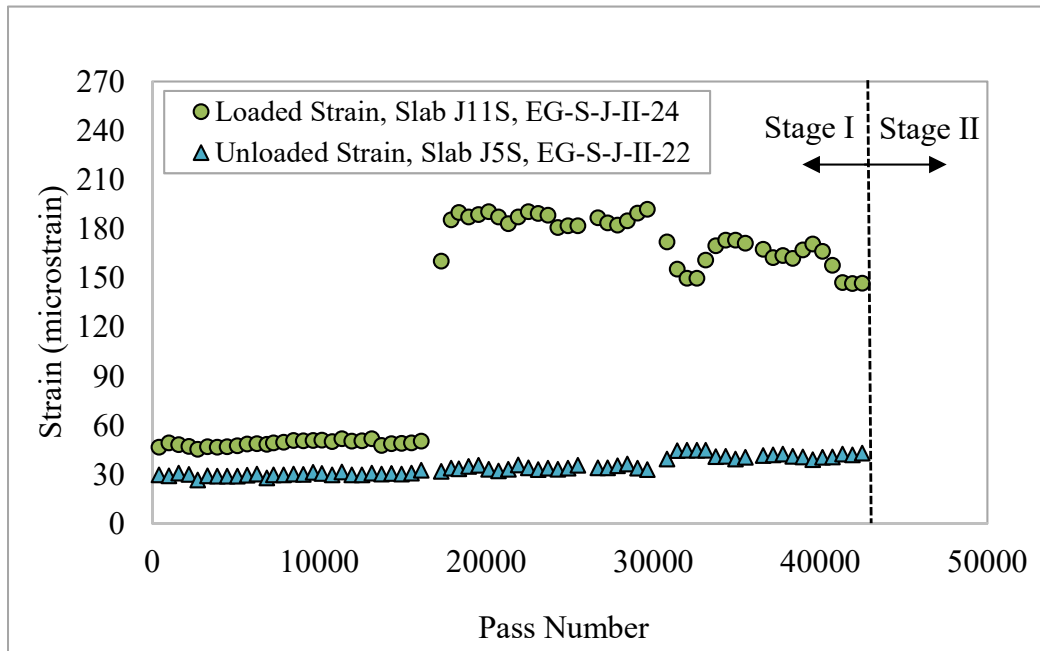


Figure 38. Loaded and Unloaded Strains (Track L2) used to Determine LTE_{σ} of Longitudinal Joints on the North Side: (a) Joint N 2-8, (b) Joint N 5-11



(a)



(b)

Figure 39. Loaded and Unloaded Strains (Track L2) used to Determine LTE_{σ} of Longitudinal Joints on the South Side: (a) Joint S 4-10, (b) Joint S 5-11

Stress-based Load Transfer (LT_σ)

Stress-based LT_σ was evaluated daily during trafficking. Figure 40(a) and (b) show LT_σ trends for doweled and keyed longitudinal joints, respectively. In Figure 40(a) (doweled joints), all evaluated joints maintained LT_σ greater than the 25% FAARFIELD assumption. Similarly, in Figure 40(b) (keyed joints), LT_σ for all joints stayed at approximately 40% for the first 17,000 passes. The rapid drop in LT_σ for joint S 5-11 to a value below 25% was associated with the occurrence of a corner break on slab J11S at 17,292 passes. At the end of Stage I, the average values of LT_σ for doweled and keyway joints were 35.6% and 36.2 %, respectively. In other words, after experiencing identical traffic, the overall edge stress transfer capability for both joint types was similar.

During Stage II, additional 3D traffic on the south test item caused the LT_σ for keyed joints in the SE slab subgroup (dummy transverse joints) to drop rapidly below 25%. The keyed joints in the SW subgroup (doweled transverse joints) remained above 25% throughout Stage II.

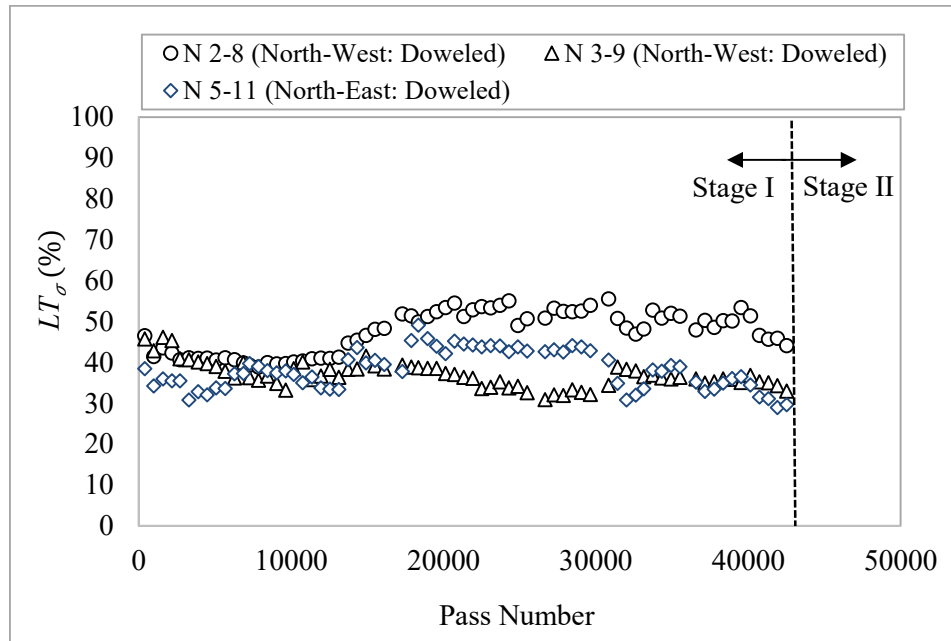
6.1.1.3 KEY FINDINGS

Transverse Joints

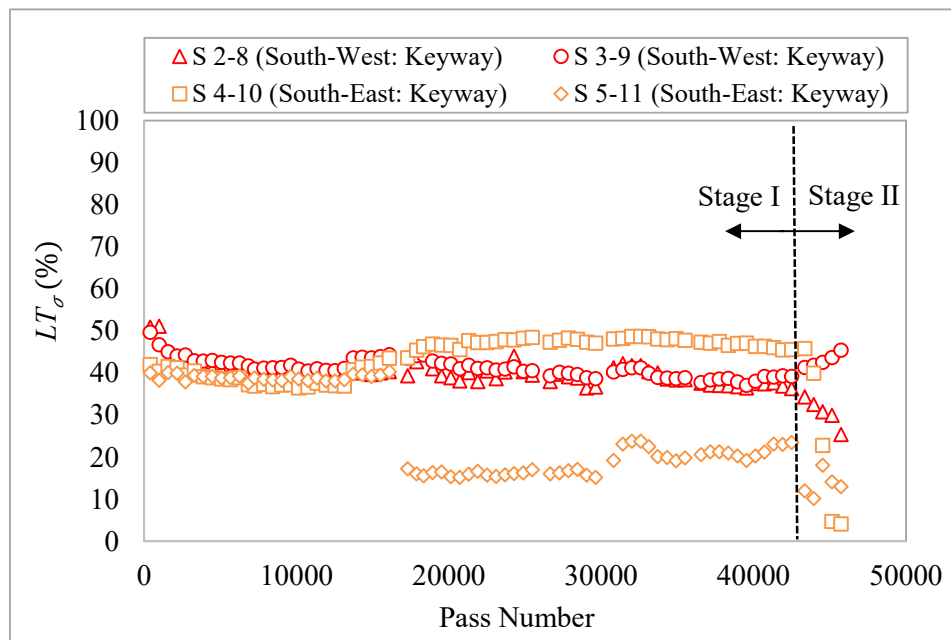
- Stress-based LT_σ across doweled contraction joints remained nearly constant under traffic with D gears.
- For undoweled transverse joints, LT_σ gradually was primarily a function of aggregate interlock related to slab temperature.
- After the traffic was changed to 3D, the doweled joints exhibited a gradual decrease in LT_σ . For undoweled joints, LT_σ dropped below 25%. This drop was attributed to the combined effect of lower slab temperatures and the occurrence of a corner break.
- Stress-based LT_σ across doweled contraction joints remained close to or above 30% regardless of gear configuration (D or 3D).

Longitudinal Joints

- Stress-based LT_σ was comparable for doweled and sinusoidal keyed construction joints.
- Under traffic with D gears, LT_σ values remained at or above 30% provided the load transfer mechanism was not compromised by distress.
- Under traffic with heavy 3D gears, LT_σ degraded rapidly along keyed joints to under 25% (with one exception – S 3-9).
- Unusual increases in LT_σ were observed in both joint types, attributed to local damage or cracks at the bottom of the loaded slab affecting the strain gage. All joints should be inspected during the post-traffic investigation.



(a)



(b)

Figure 40. LT_{σ} of Longitudinal Joints from Instrumentation Data Calculated by Sensor Pair Method: (a) Doweled, and (b) Keyway

6.1.2 HWD DEFLECTION DATA

6.1.2.1 TRANSVERSE JOINTS

Deflection-based Load Transfer Efficiency (LTE_δ)

Deflection-based LTE_δ was evaluated for transverse and longitudinal joints as described in Section 5.1.2. Figure 41(a) through (d) plot LTE_δ for transverse joints as a function of pass number, for each of the four subgroups. From Figure 41(a) and (b), LTE_δ for subgroups with doweled contraction joints remained essentially constant throughout Stage I. After the start of Stage II traffic on the south test items, there was a large drop in LTE_δ for transverse on the inner lane of the SW slab group (but not the outer lane). The LTE_δ for doweled transverse joints remained at 79% or above.

Figure 41(c) and (d) plot LTE_δ for subgroups with undoweled transverse joints. Initially, LTE_δ values for these joints ranged from 33% - 90%. Joints N 5-6, N 11-12, S 5-6, and S 11-12, all located near the east end of their respective slab groups, had high initial LTE_δ compared to the joints to the west. Referring to figure 2, the line of slabs consisting of J6N, J12N, J6S, and J12S was joined to Transition 3 by dowels. It is speculated that this doweled connection had a restraining effect on these slabs, leading to the high initial LTE_δ values observed. The relatively high LTE_δ values for joints N 5-6 and S 5-6 (inner lane) dropped rapidly after the start of Stage I traffic. As expected, LTE_δ for undoweled joints correlated well with slab temperature changes (Figure 35). In cold temperatures, the LTE_δ for undoweled transverse joints was as low as 16.5%. The end of Stage I saw slab temperatures over 80°F, and LTE_δ for all undoweled transverse joints climbed above 80% due to much higher aggregate interlock. In Stage II, the LTE_δ again dropped, due to the lower temperature, combined with slab damage under higher 3D gear loads.

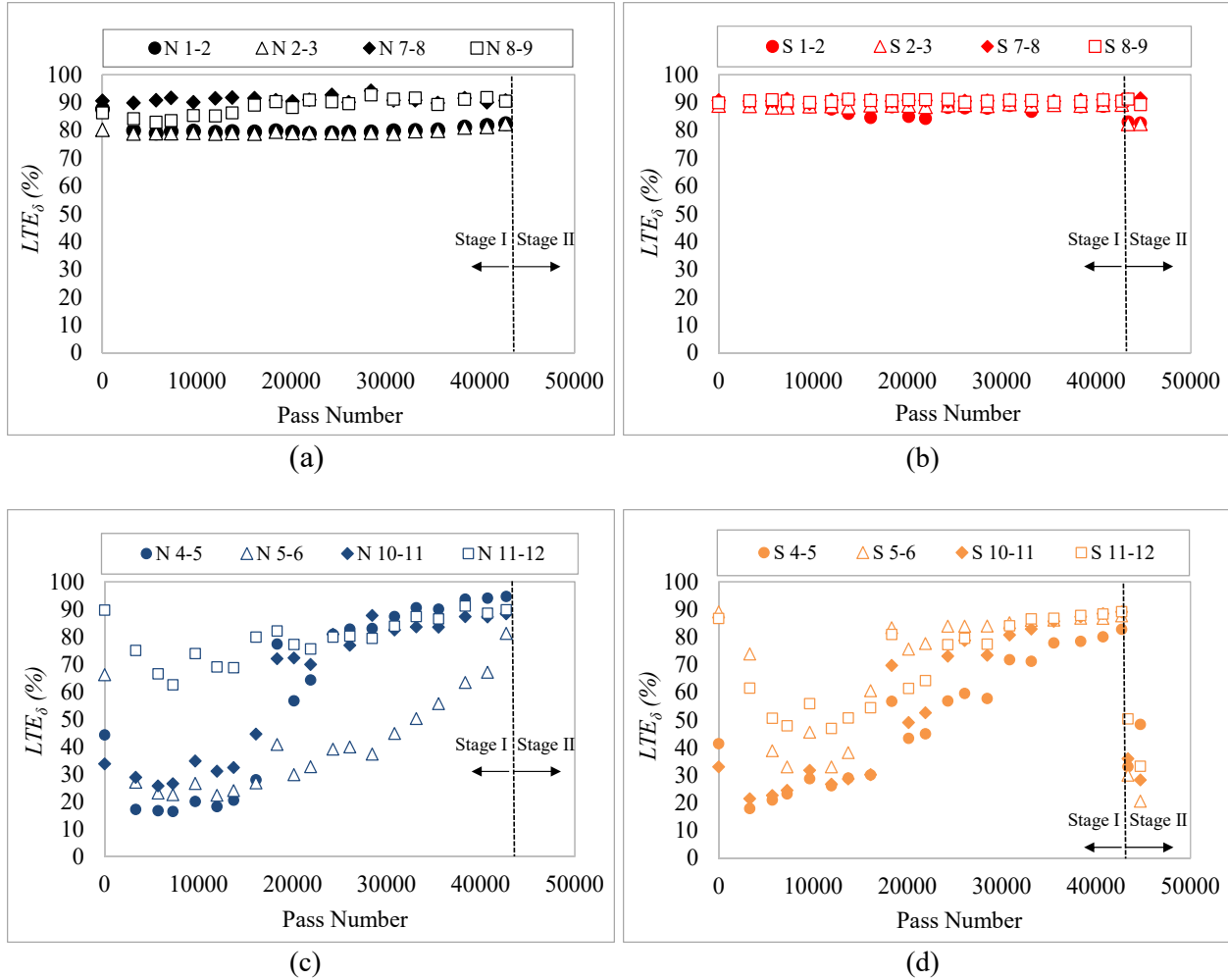
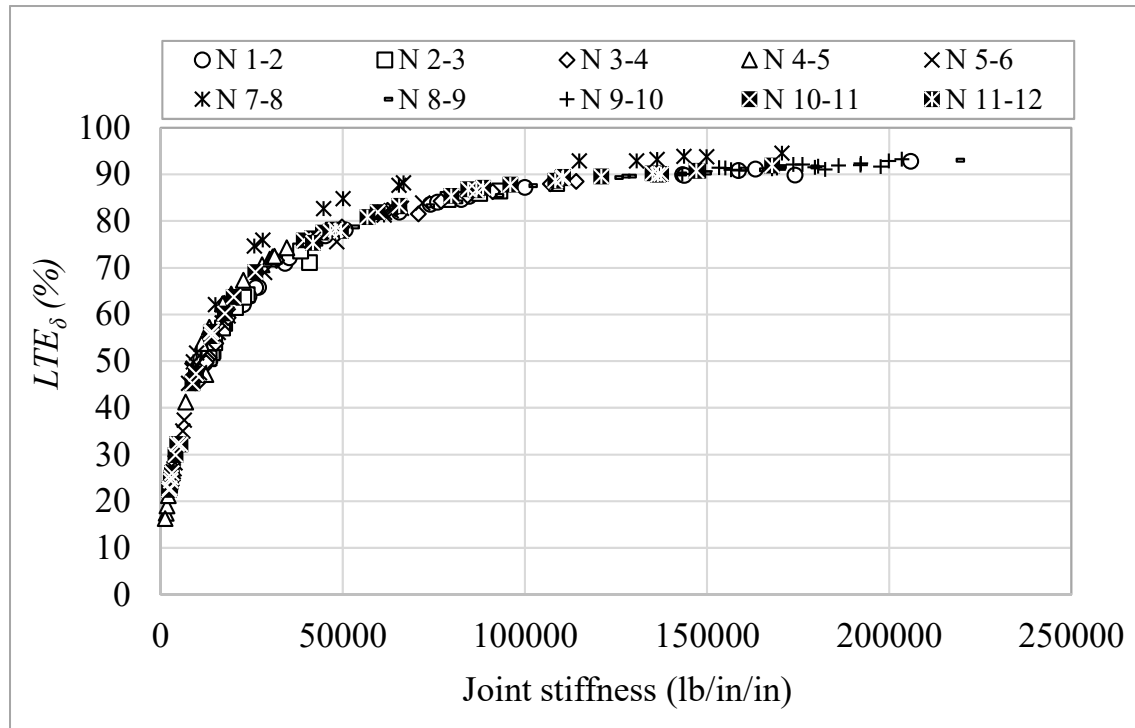


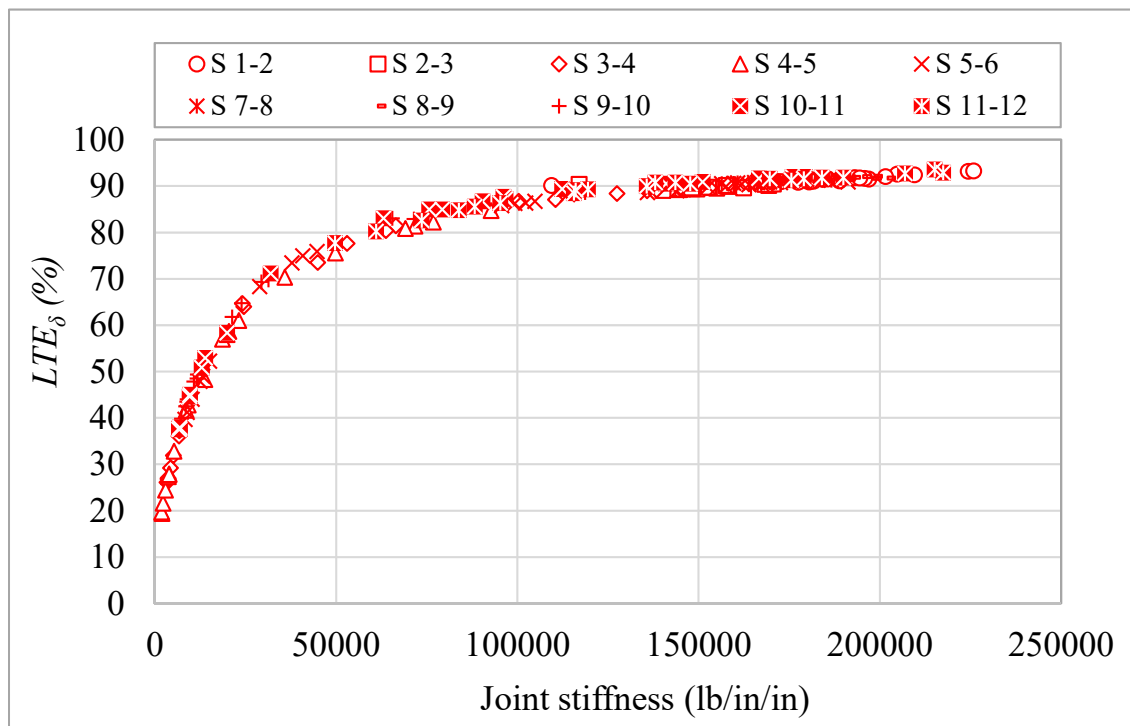
Figure 41. Change in Deflection-Based LTE_{δ} for Transverse Joints: (a) NW - Doweled, (b) SW - Doweled, (c) NE - Undoweled, (d) SE - Undoweled

Joint Stiffness (k_J)

Transverse joint stiffness (k_J) was calculated both directly from HWD deflection data and inferred from deflection-based LTE_{δ} (see Section 5.1.3). Figure 42(a) and (b) show the correlation between k_J and LTE_{δ} for the north and south test pavements, respectively. These figures include data from 10 transverse joints on each test pavement. Figure 42(a) (north) covers Stage I data only, while Figure 42(b) (south) includes data from both stages. The observed trends were similar. At k_J values below 50,000 lb/in/in, transverse LTE_{δ} is highly sensitive to changes in joint stiffness. Over $k_J = 50,000$ lb/in/in, the sensitivity of LTE_{δ} to joint stiffness is significantly less. Above $k_J = 150,000$ lb/in/in, there is almost no variation in LTE_{δ} . In Figure 43(a) - (d), the data from Figure 42 are separated by slab group. All slab groups followed a similar trend. However, the data for undoweled joints (Figure 43(c)-(d)) are spread over a much wider k_J range than the data for doweled joints in (Figure 43(a) - (b)).



(a)



(b)

Figure 42. Correlation between LTE_{δ} and k_J for Transverse Joints: (a) North, (b) South

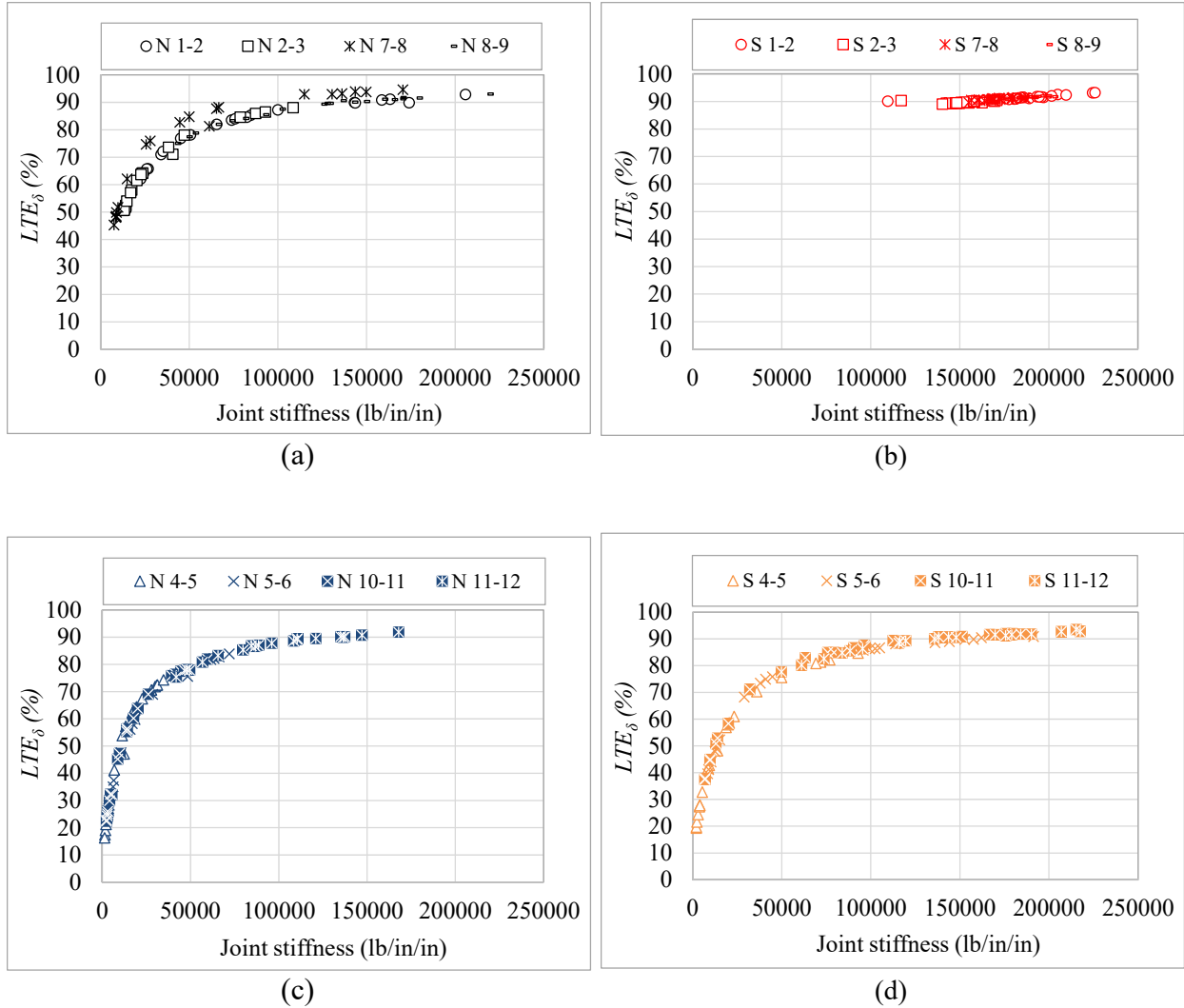


Figure 43. Correlation between LTE_{δ} and k_J for Transverse Joints: (a) NW - Doweled, (b) SW - Doweled, (c) NE - Undoweled, (d) SE - Undoweled

6.1.2.2 LONGITUDINAL JOINTS

Deflection-based Load Transfer Efficiency (LTE_{δ})

Figure 44(a) through (d) show the evolution of LTE_{δ} with traffic for longitudinal construction joints. At the start of Stage I, LTE_{δ} values ranged from 72% - 89%. After exhibiting initial shakedown, the LTE_{δ} values deteriorated at a consistent rate throughout the traffic test. The trends were most consistent for doweled construction joints (Figure 44(a) and (b)). At the end of Stage I, doweled construction joints had slightly higher LTE_{δ} than keyed joints. During Stage II, keyed joint S 3-9 (figure 44(c)) initially increased to 45% before resuming a downward trend under 3D traffic. Keyed joints S 4-10 and S 5-11 (figure 44(d)) exhibited similar behavior.

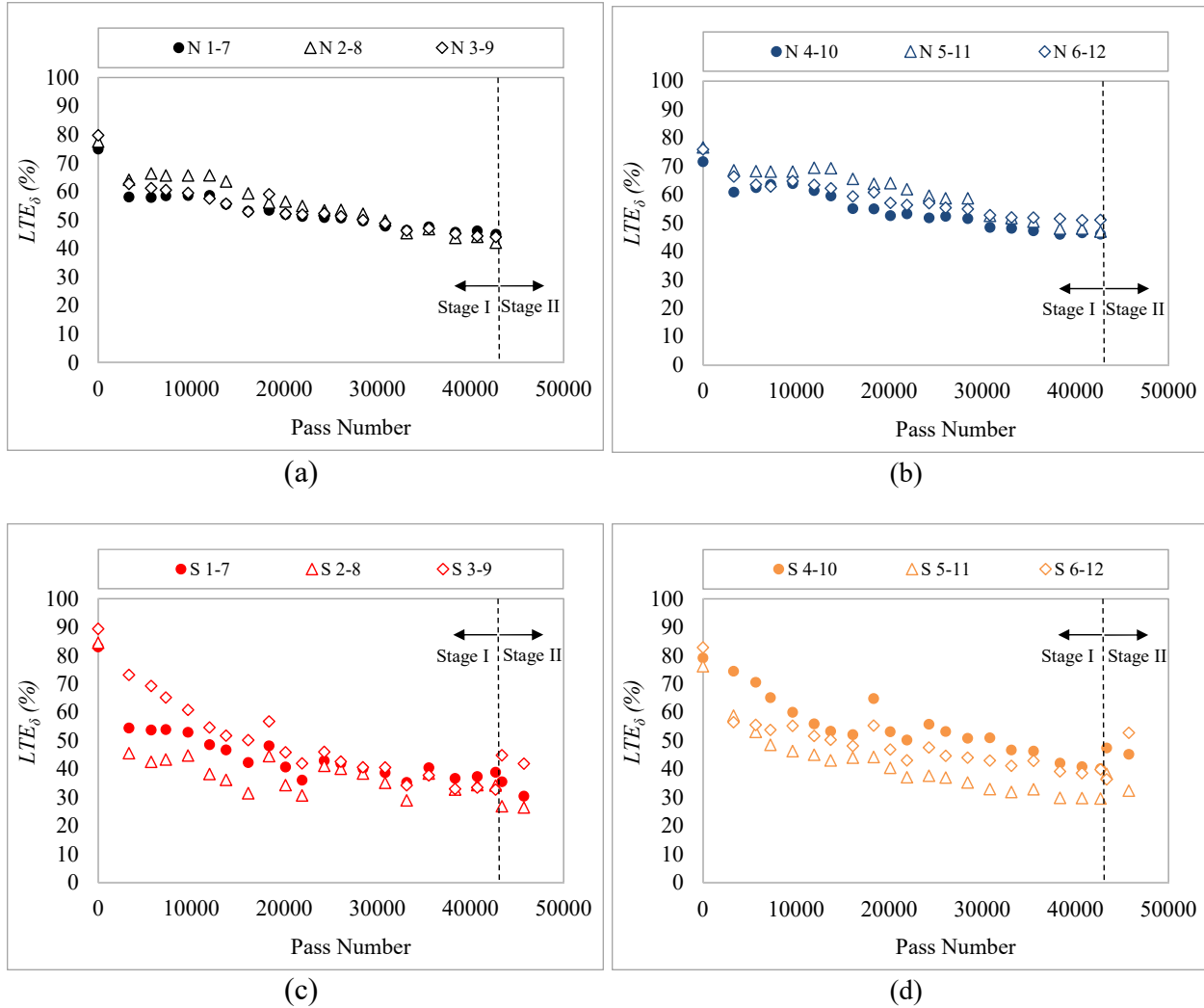
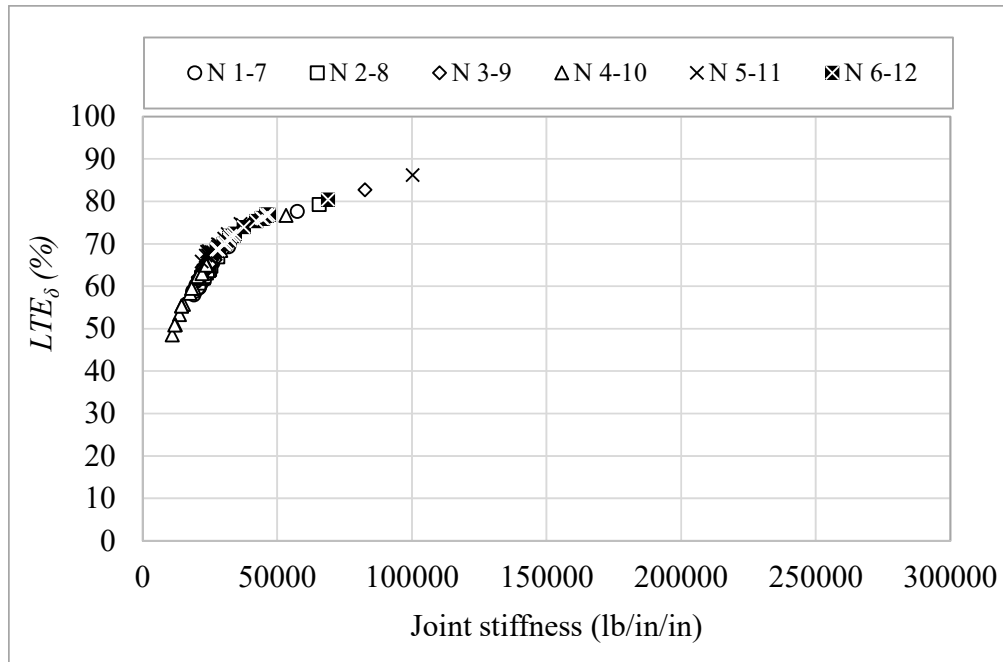


Figure 44. Change in Deflection-Based LTE_{δ} of Longitudinal Joints: (a) North-West: Doweled, (b) North-East: Doweled, (c) South-West: Keyway, (d) South-East: Keyway

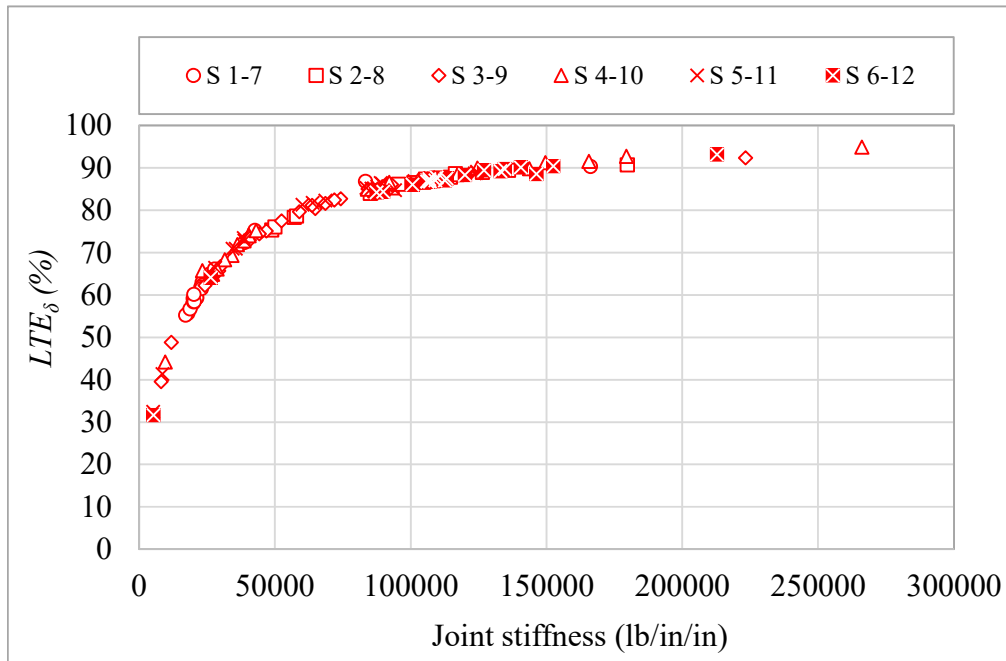
Joint Stiffness (k_J)

Longitudinal joint stiffness (k_J) was calculated both directly using HWD deflection data and indirectly from deflection-based LTE_{δ} , (see Section 5.1.3). Figure 45(a) and (b) show the correlation between k_J and LTE_{δ} for the north and south test pavements, respectively. These figures include data from 6 longitudinal joints on each test pavement.

In part due to the inclusion of Stage II data, the south test pavement (Figure 45) covered a wider range of LTE_{δ} and k_J values than the north (Figure 44). Nevertheless, the correlation between LTE_{δ} and k_J for the two test pavements was similar within the range $k_J = 10,000 - 100,000$ lbs./in./in. In Figure 46(a) through (d), the data from figure 45 are segregated by slab groups. In contrast to the similar plots for transverse joint stiffness (Figure 43), for longitudinal joints the lower ends of the curves, where significant variations in LTE_{δ} correspond to slight variations in k_J , were absent.



(a)



(b)

Figure 45. Correlation between LTE_{δ} and k_J for Longitudinal Joints: (a) North, (b) South

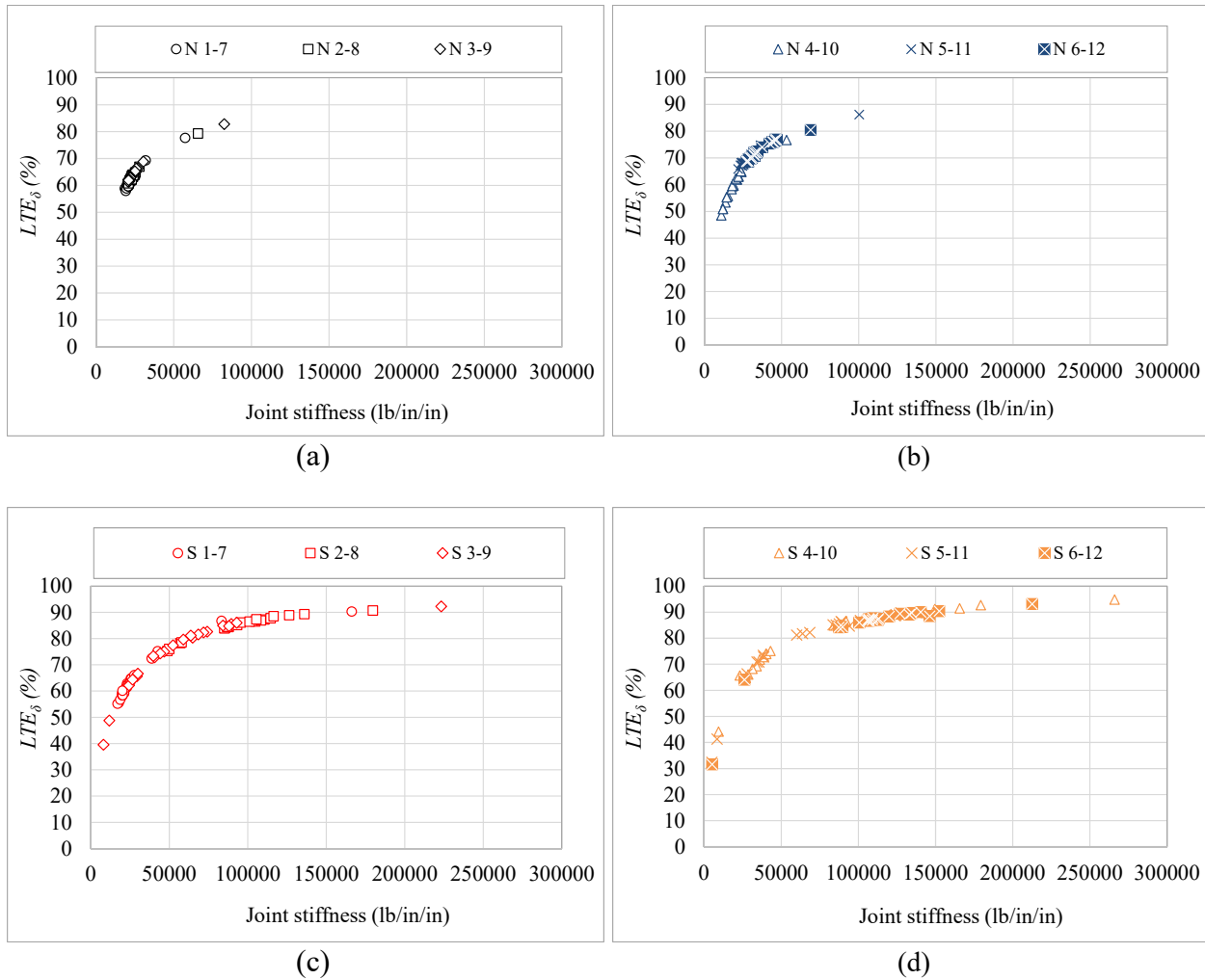


Figure 46. Correlation between LTE_{δ} and k_J for Longitudinal Joints: (a) NW - Doweled, (b) NE - Doweled, (c) SW - Sinusoidal Keyed, (d) SE - Sinusoidal Keyed

6.1.2.3 KEY FINDINGS

Transverse Joints

- The value of LTE_{δ} for doweled contraction joints remained above 79% for the duration of the test, regardless of gear configuration. No temperature effects were observed for this joint type.
- During Stage I, undoweled contraction joints had generally lower LTE_{δ} than doweled contraction joints.
- For undoweled joints, LTE_{δ} was highly temperature dependent.
- Above a threshold LTE_{δ} value of 90% (corresponding to approximately $k_J=150,000$ lbs./in./in.), changes in joint stiffness did not significantly affect LTE_{δ} .

Longitudinal Joints

- Post-construction (new) LTE_{δ} values for keyed construction joints were higher than those for doweled construction joints.
- After initial shakedown under Stage I traffic, LTE_{δ} deteriorated at a slightly higher rate for keyed construction joints than for doweled construction joints. Doweled construction joints retained somewhat higher LTE_{δ} at the end of the test than keyed longitudinal joints.
- During Stage II, inconsistencies were observed in the rate of LTE_{δ} change in both the SW and SE slab groups.
- For doweled construction joints, k_J varied within a relatively narrow range of 10,000 to 100,000 lbs./in./in., corresponding to $LTE_{\delta} = 50\% - 85\%$. For sinusoidal keyed joints, k_J varied in a much wider range.

6.2 SLAB DETERIORATION

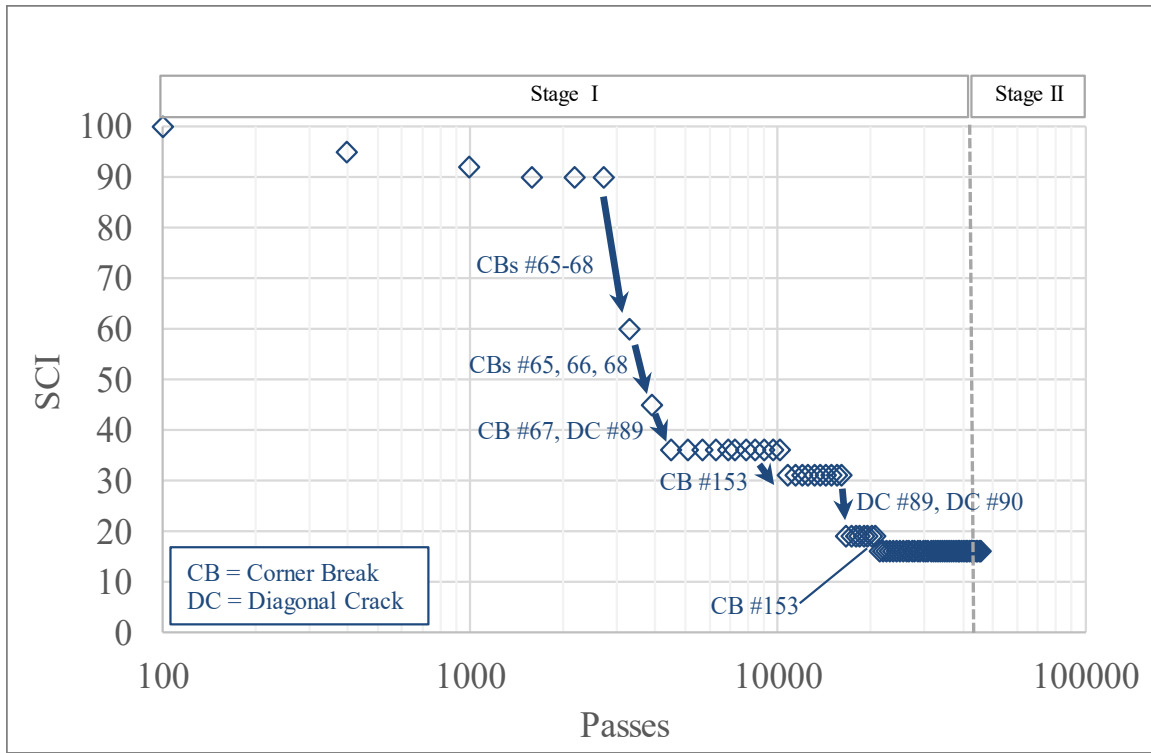
6.2.1 RIGID PAVEMENT DISTRESSES

Terminal SCI values for Stage I were: 16, 16, 13, and 79 for subgroups NW, NE, SW, and SE, respectively (Section 5.2.2, Figure 29). Compared to the other subgroups, the terminal structural condition of the SE subgroup was significantly higher. In Stage II, heavy 3D gear loading increased the rate of SCI deterioration in both the SW and SE subgroups. The terminal SCI values for Stage II were 2 (SW) and 41 (SE).

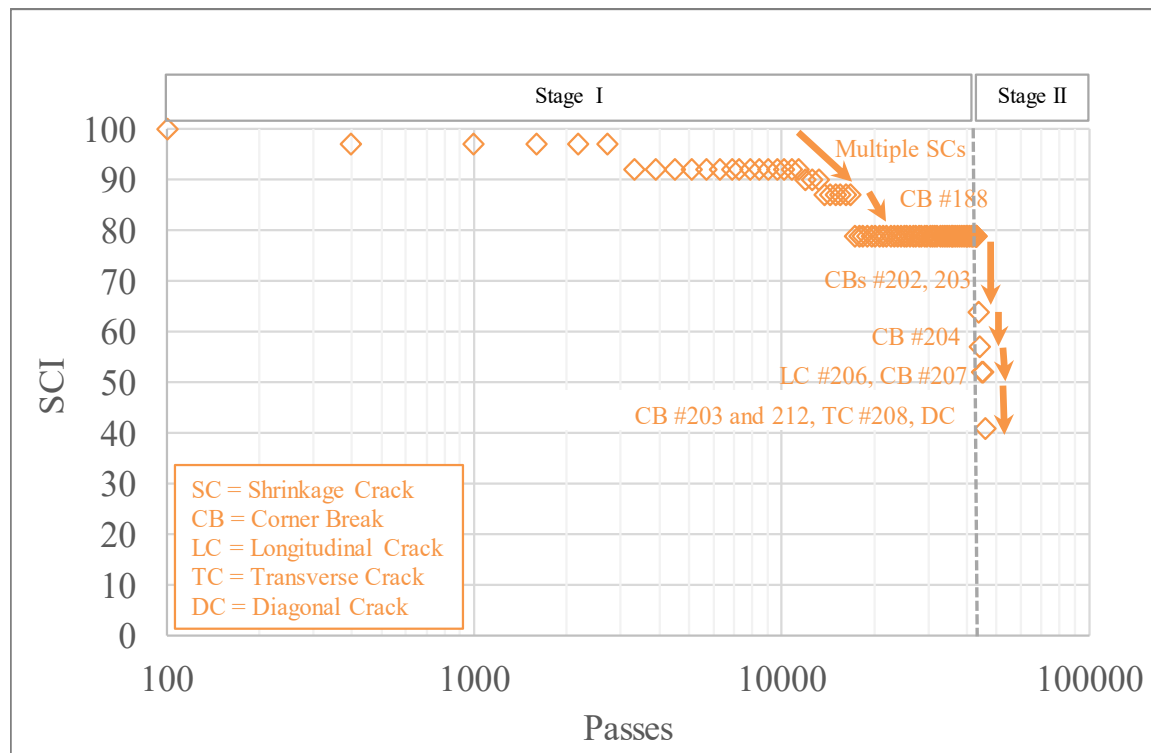
Average CD values were also calculated for each slab subgroup (Section 5.2.3, Figure 31). Terminal CD values for Stage I were: 6.7, 10.4, 3.8, and 1.4 for slab groups NW, NE, SW, and SE, respectively. Again, the SE subgroup had the least amount of cracking. At the end of Stage II, CD values for the SW and SE subgroups had increased to 6.4 and 6.0, respectively. Thus, the amount of cracking developed during Stage II was proportionately much higher on the SE subgroup than on the SW.

Figure 47(a) and (b) relate significant SCI reductions to particular slab distresses, for those slab groups with undoweled contraction joints. Figure 47(a) shows that corner breaks, followed by diagonal cracks, were the dominant distresses causing rapid loss of SCI in the NE subgroup. The PCI system heavily penalizes corner breaks. In the SE subgroup (Figure 47(b)), only one corner break occurred during Stage I. However, five additional corner breaks developed on the in the SE subgroup during Stage II, driving the later reduction in SCI during Phase II.

Figure 48(a) and (b) relate significant SCI reductions to particular slab distresses, for those slab groups with doweled contraction joints. For both subgroups, corner breaks, followed by longitudinal and transverse cracks were the dominant distress types driving the pavement condition reduction. Although initial damage occurred earlier in the SW subgroup than in the NW subgroup, the deterioration trends and terminal conditions for the two groups were similar. Three corner breaks occurred on the NW group, versus two on the SW (in Stage I). Two more corner breaks occurred on the SW subgroup in Stage II.

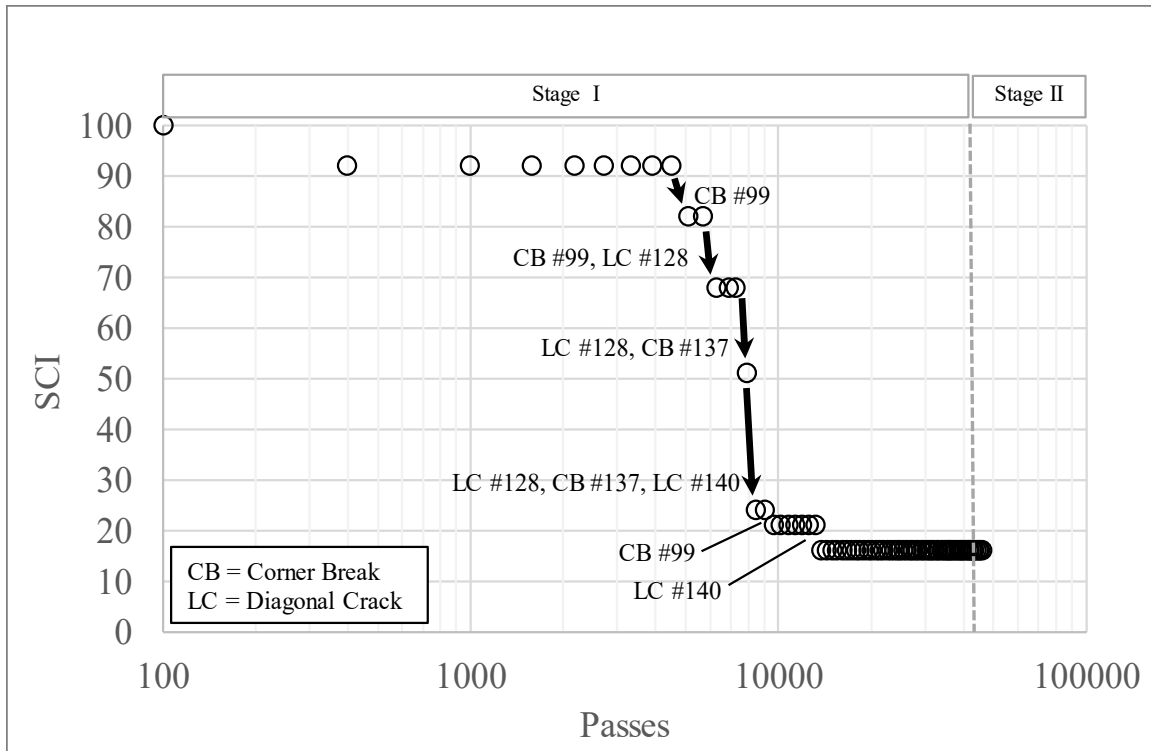


(a)

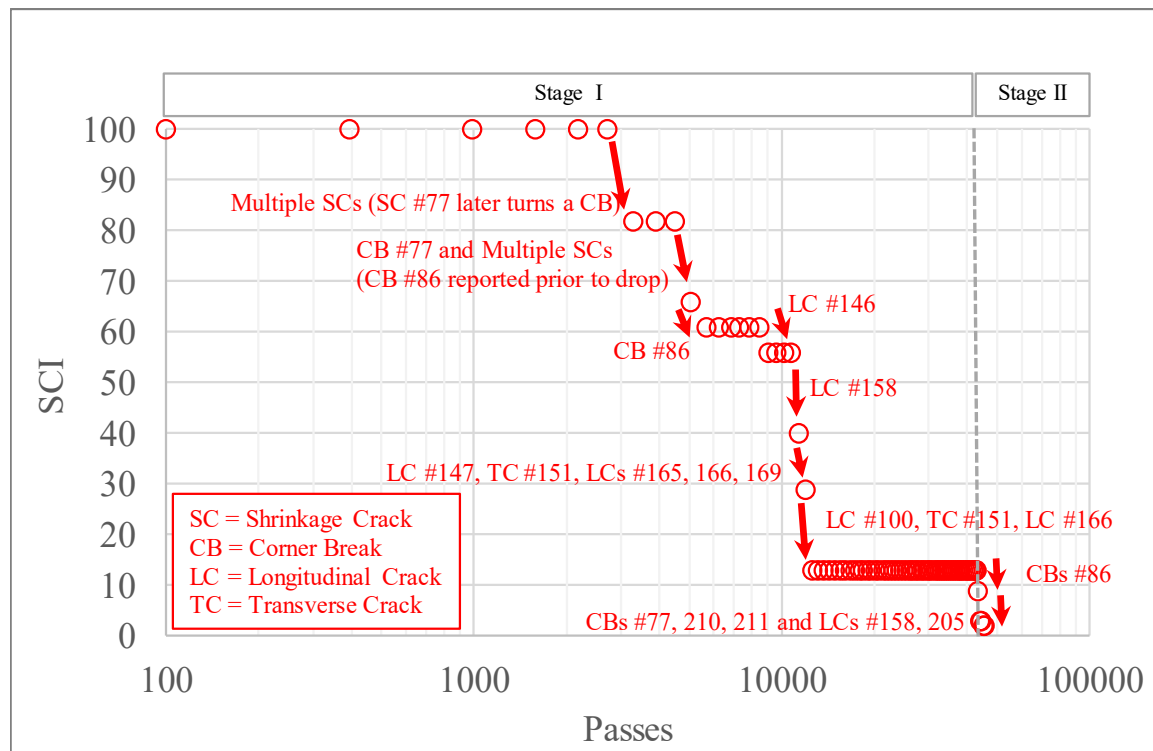


(b)

Figure 47. Distresses Associated With Major SCI Changes in Slab Groups with Undoweled Contraction Joints: (a) NE, (b) SE



(a)



(b)

Figure 48. Distresses Associated With Major SCI Changes in Slab Groups with Doweled Contraction Joints: (a) NW, (b) SW

Figure 49 and Figure 50 map the distresses at the end of Stage I and Stage II, respectively. Corner breaks and all other major distresses on the NE subgroup were distributed over five of six slabs. On the SE subgroup, only one corner break occurred in slab J11S. In subgroups NW and SW, all major distresses were isolated to slabs J1N, J7N, J1S, and J7S, adjacent to the transition. At least some of the major damage observed in the NW and SW subgroups can be attributed to the influence of Transition 2 at the west end of the Phase 3 test pavement. If the slabs in question (J1N, J7N, J1S, and J7S) are removed from the analysis, then it is not possible to evaluate the relative benefit of keyed versus doweled joints based on slab condition, since the remaining slabs in both subgroups had minimal structural damage.

Figure 50 shows that Stage II traffic accelerated the structural damage to the SW and SE subgroups. On the SE subgroup (undoweled), structural cracks extended to five of six slabs. Most of the damage on the SW subgroup (doweled) continued to be confined to slabs J1S and J7S adjacent to the transition, except for one new corner break in slab J9S. The latter corner break was on the east end of slab J9S, where the transition to the SE subgroup was undoweled. These observations confirm that the slab groups with doweled contraction joints generally exhibited better structural performance than those with undoweled contraction joints, especially under the heavy 3D gear loads.

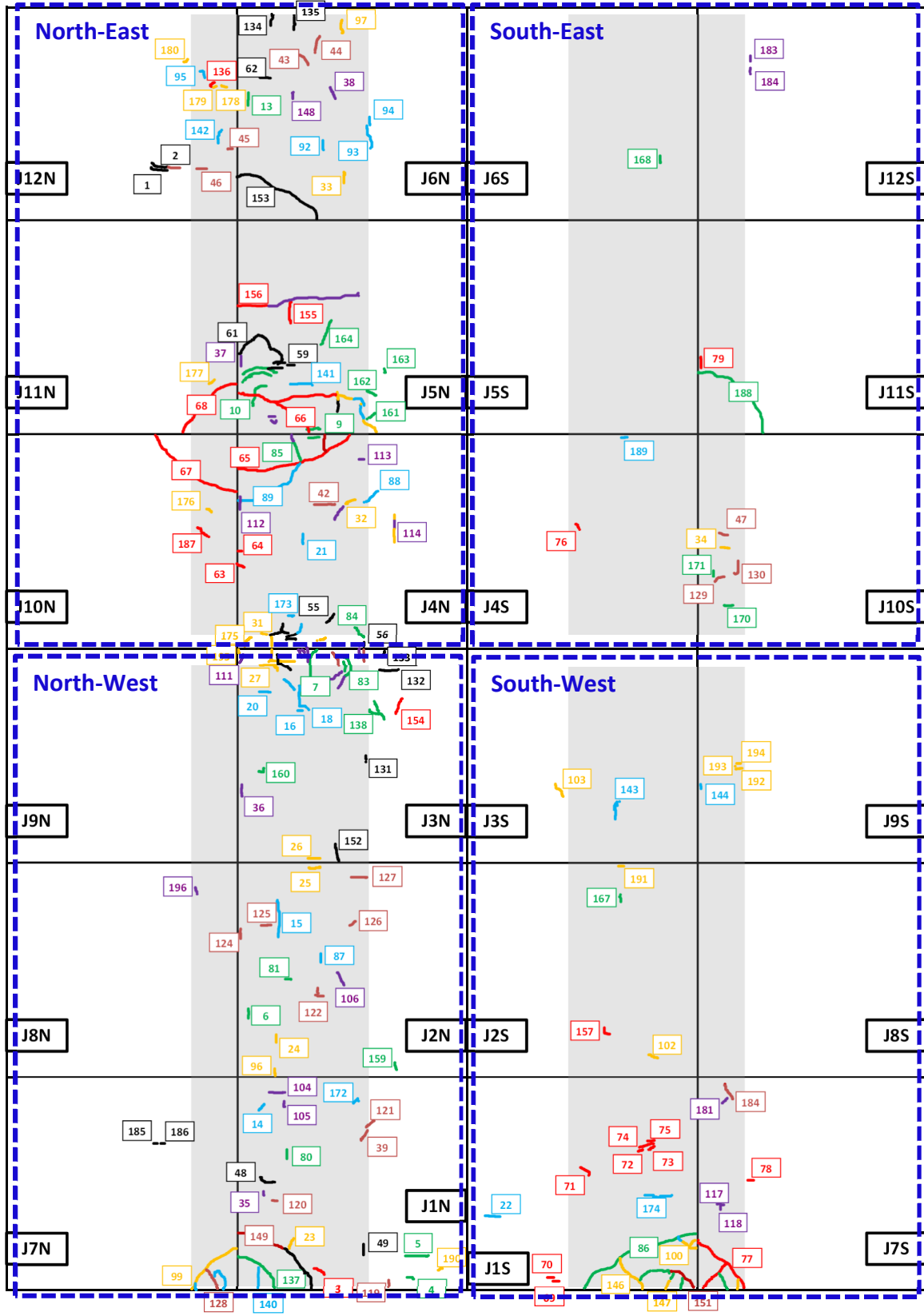


Figure 49. Distress Mapping at End of Stage I (D Gear at 65,000 lb. Wheel Load)

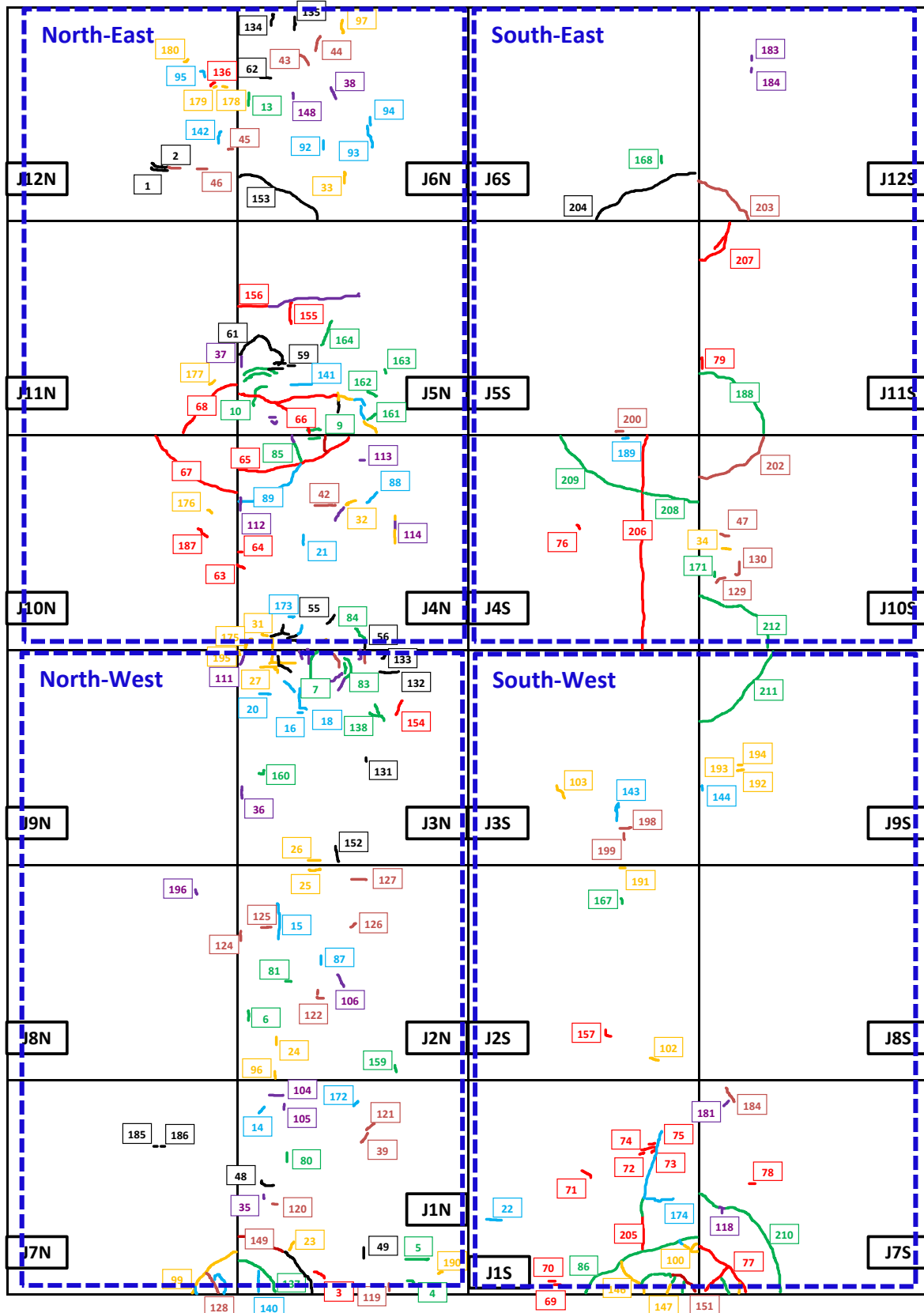


Figure 50. Distress Mapping at End of Stage II (3D Gear at 70,000 lb. Wheel Load)

6.2.2 DETERIORATION BASED ON HWD DEFLECTION

6.2.2.1 SLAB INTERIOR DETERIORATION

Deflection Basin

HWD tests were conducted on both north and south test lanes at the centers of all 24 slabs. Figure 51 through Figure 54 show deflection basins corresponding to 36,000-lb. HWD drops, grouped by slab subgroups. For all subgroups, slabs on the inner lanes (right side of figures) exhibited significant changes in the deflection basin over the course of trafficking, while no significant deflection basin changes were observed for outer lane slabs (left side). The SW and SE subgroups exhibited rapid increases in HWD deflections during Stage II (after August 9, 2018), consistent with the increased number of visible distresses in Stage II.

Impulse Stiffness Modulus (ISM)

Impulse Stiffness Modulus (ISM) is the ratio of HWD test load (P) to the maximum deflection (δ_{max}) at the center of the load plate. ISM was calculated for $P = 36,000$ pounds:

$$ISM = \frac{P}{\delta_{max}} \quad (11)$$

Figure 55 and Figure 56 plot ISM as a function of the pass number for slabs on the north and south test pavements, respectively. Both north and south test pavements exhibited a small, gradual decrease in ISM with Stage I traffic, followed by a leveling off after about 20,000 passes. For the NW subgroup (Figure 55(a)), ISM values remained above 3900 kip/in, with little variability. For the NE slab group (Figure 55(b)), where there was greater variability of transverse load transfer and more visible structural distress, the ISM variability was also greater. From Figure 56(a) and (b), both SW and SE subgroups had ISM values above 4,000 kips/in at the end of Stage I. During Stage II, the ISM on both subgroups dropped. The terminal ISM values on the SE group were higher than those on the SW group, consistent with the terminal SCI and CD values reported in Section 6.2.1.

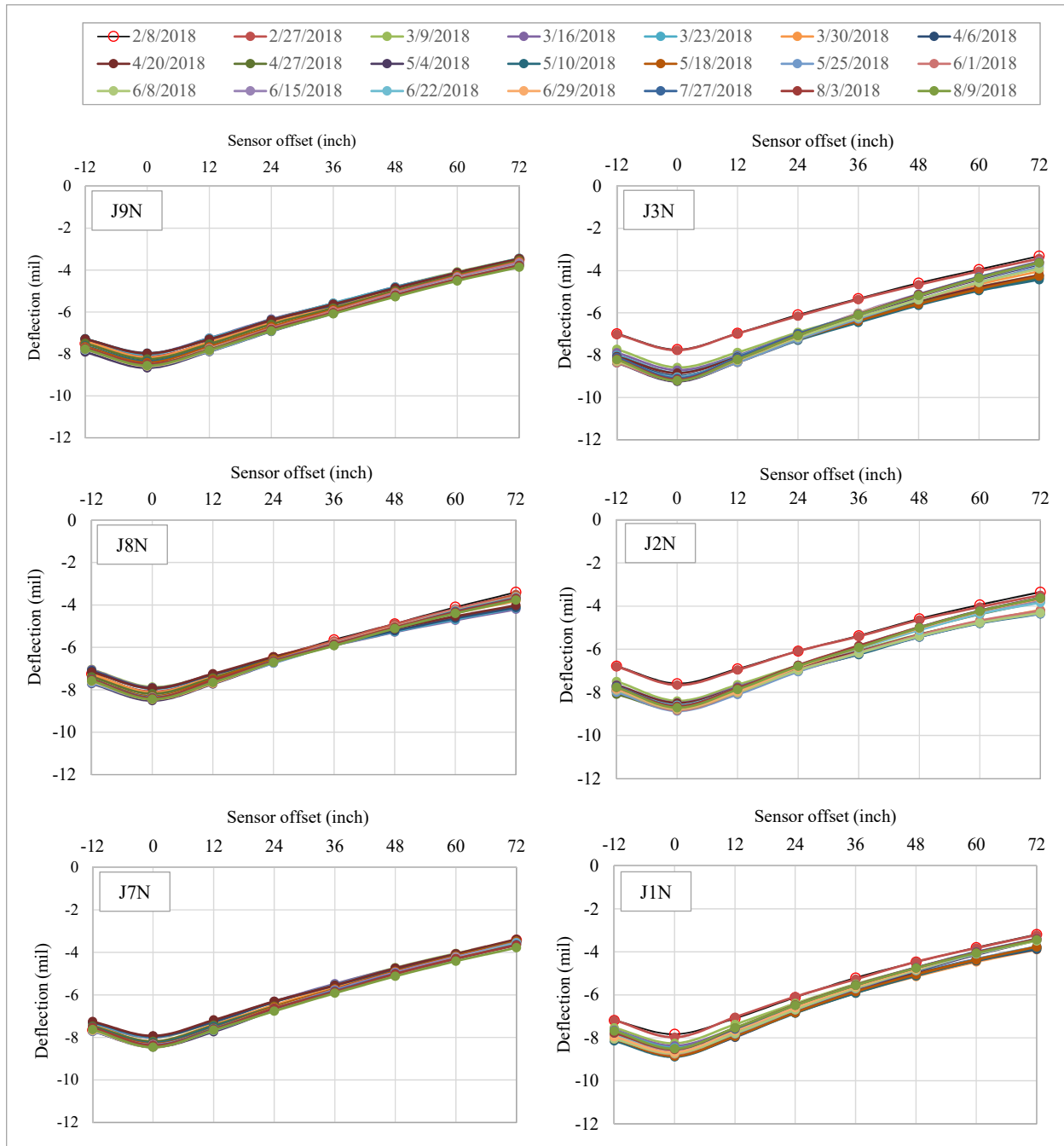


Figure 51. Slab Center Deflection Basins, North-West Slab Group

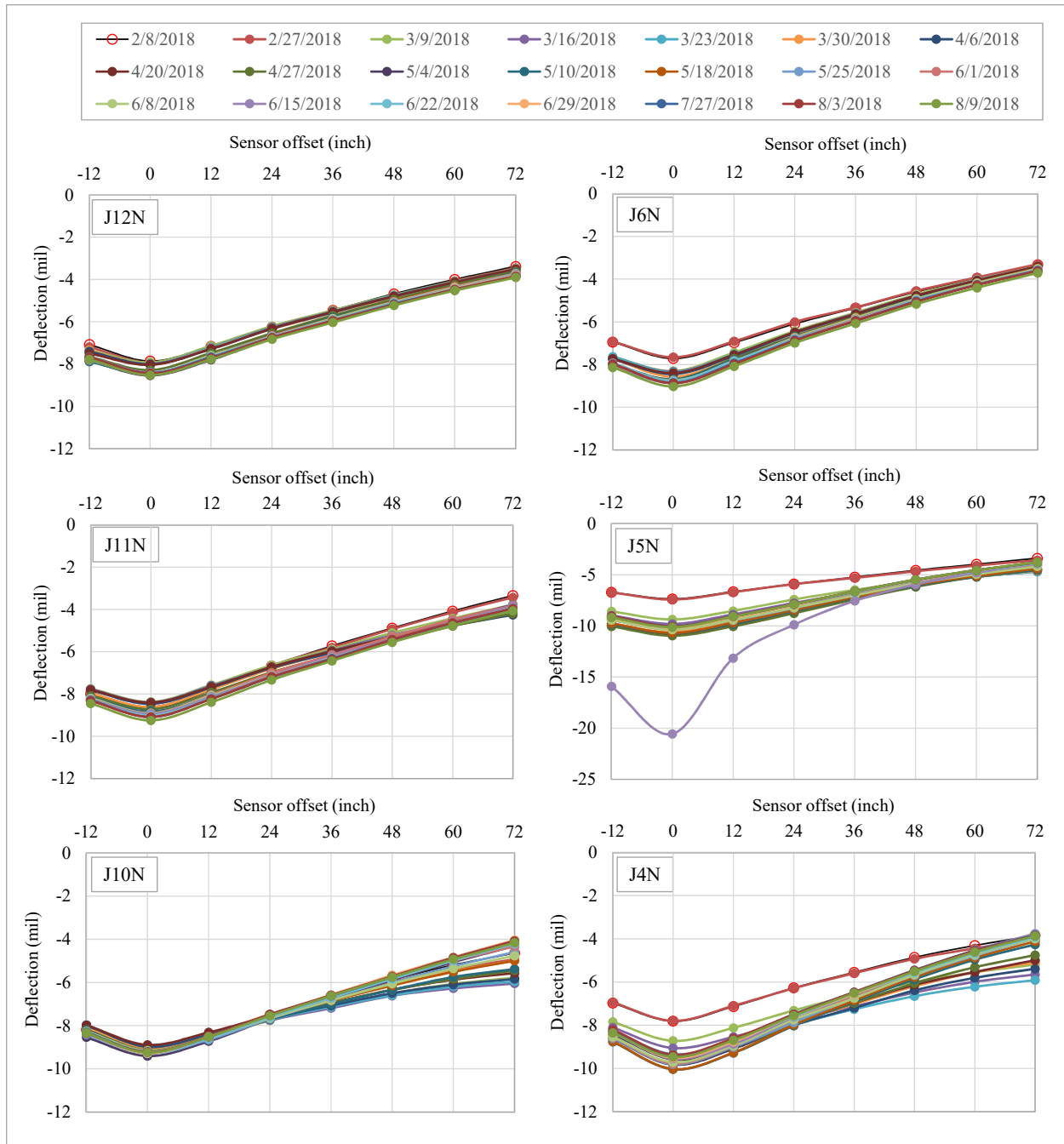


Figure 52. Slab Center Deflection Basins, North-East Slab Group

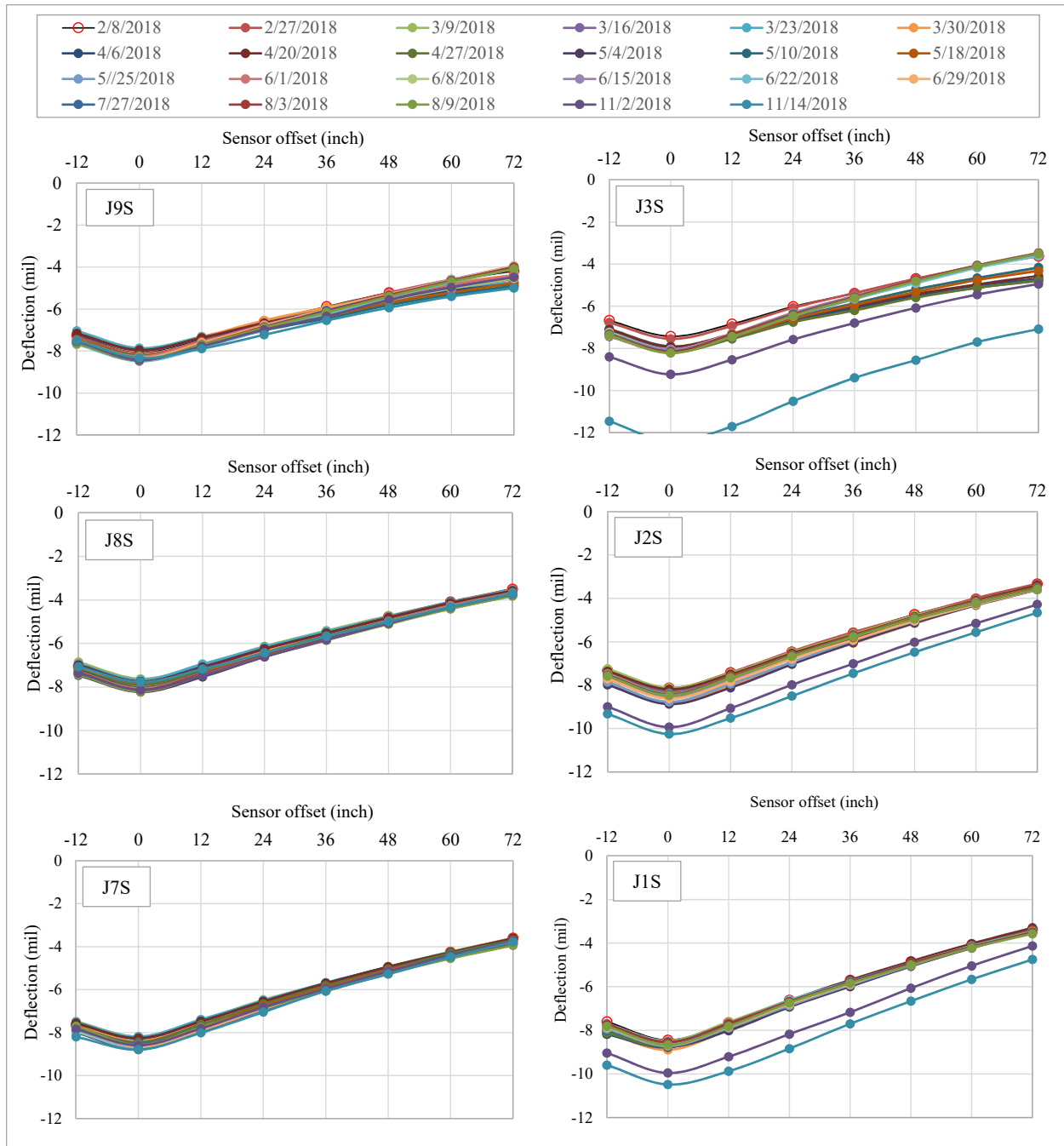


Figure 53. Slab Center Deflection Basins, South-West Slab Group

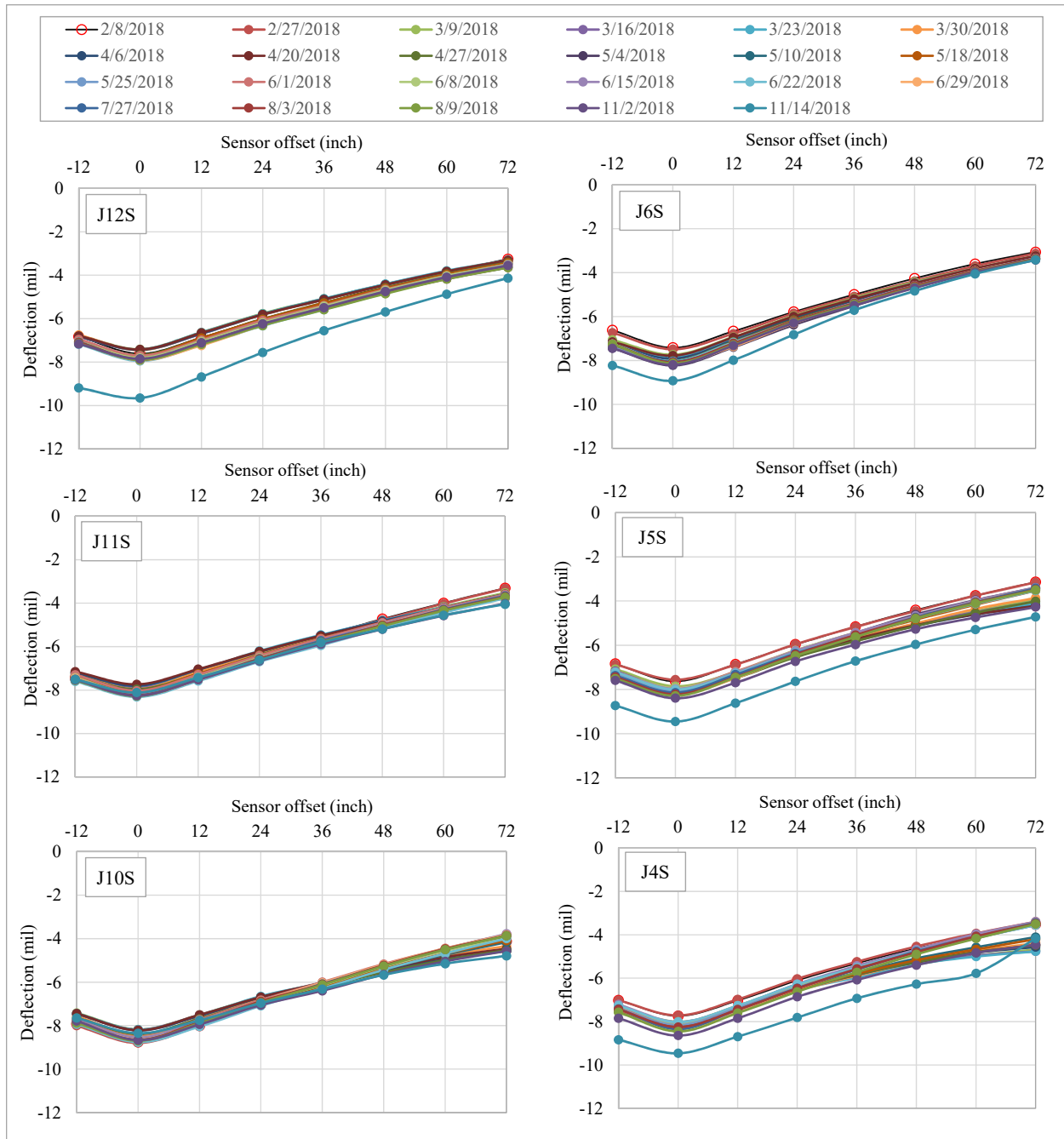
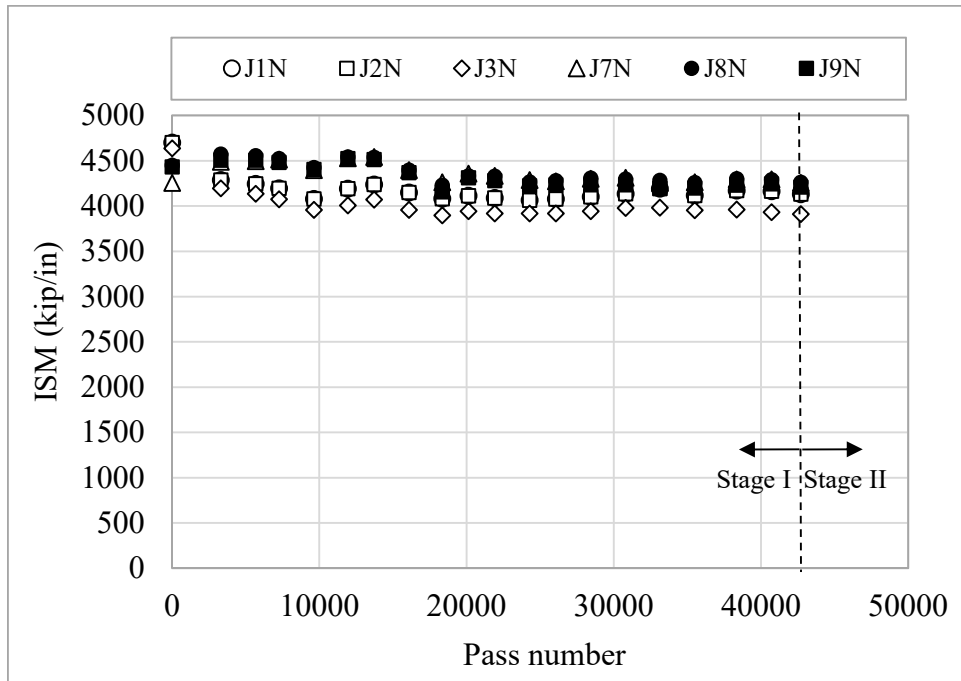
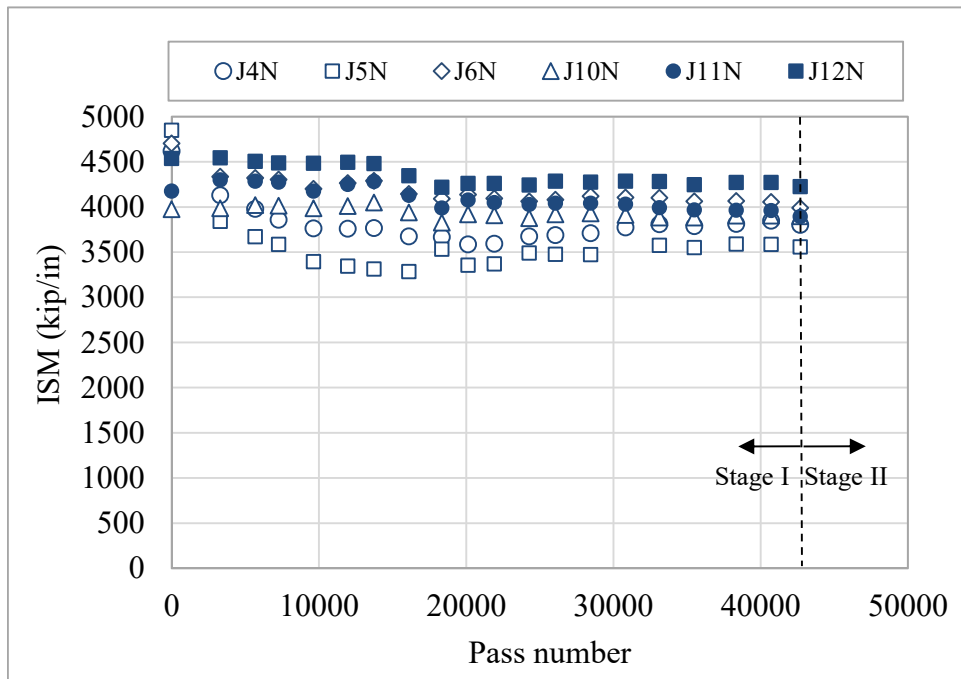


Figure 54. Slab Center Deflection Basins, South-East Slab Group

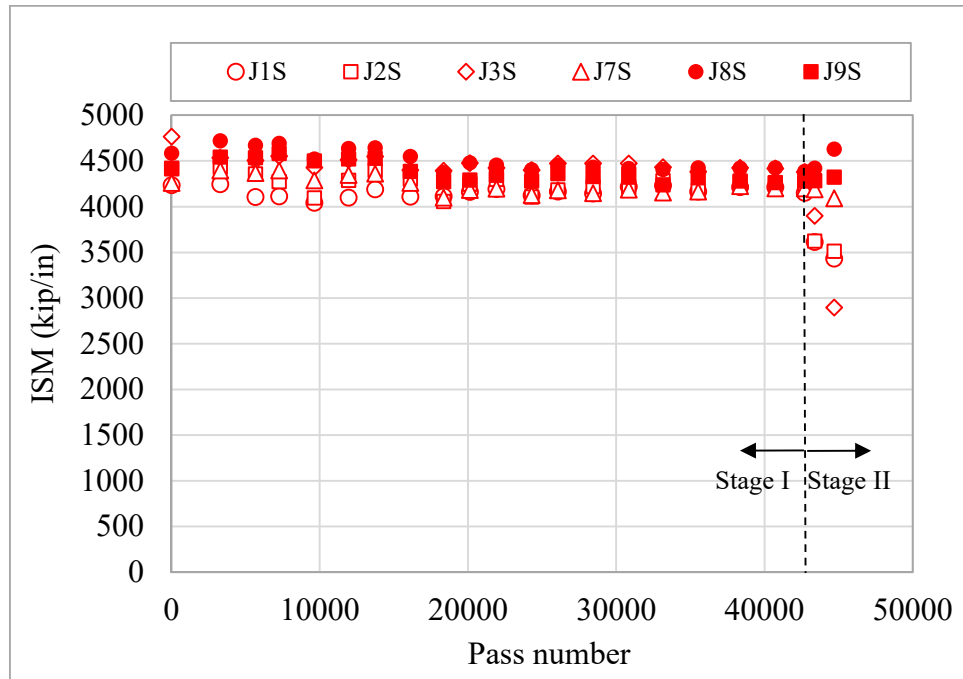


(a)

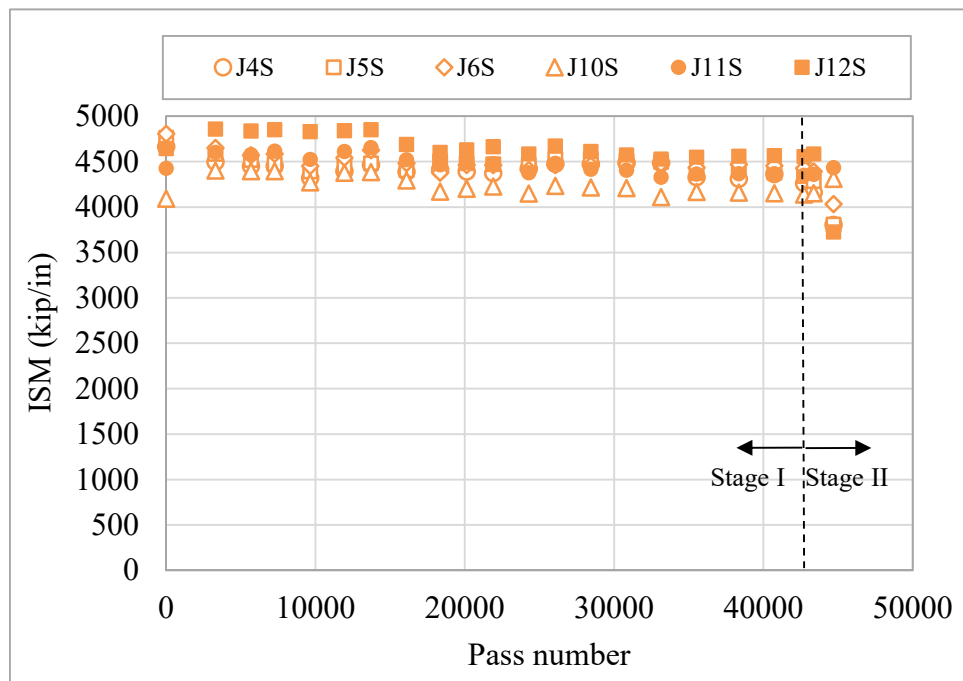


(b)

Figure 55. Change in ISM Over the Course of Traffic: (a) North-West Slab Group, (b) North-East Slab Group



(a)



(b)

Figure 56. Change in ISM Over the Course of Traffic: (a) South-West Slab Group, (b) South-East Slab Group

Backcalculation of Layer Moduli

ISM represents the combined stiffness of a pavement section but does not provide information on the structural integrity of individual structural layers. Layer moduli were backcalculated from slab center deflection basins using BAKFAA software. Table 12 lists the pavement structure and material properties used for backcalculation. The subbase and subgrade seed moduli are FAARFIELD default values. For the purpose of backcalculation, the slab-base and base-subbase interfaces were represented as fully unbonded (Interface condition: 0), while the interface between subbase and subgrade was considered fully bonded (Interface condition: 1).

Table 12. Pavement Structure and Material Properties Used for Backcalculation

Layer	Seed Modulus (ksi)	Poisson's Ratio	Interface Condition	Thickness (in)
P-501MR	4000	0.15	0.0 ¹	12
P-306MR	2000	0.2		6
P-154M	20.24	0.35	0.0 ¹	14
P-152M	11.74	0.4	1.0 ²	-

¹ fully-bonded

² unbonded

Representative layer moduli for each subgroup were determined by averaging the values for individual slabs within the group. Figure 57(a) - (d) show the changes in backcalculated modulus as a function of traffic passes for the PCC slab, base, subbase, and subgrade. After approximately 22,000 vehicle passes, the moduli of the P-501MR and P-306MR layers stabilized. There was no significant variation in P-154M subbase and P-152M subgrade moduli during Stage I traffic. However, in Stage II there was a drop in the subgrade modulus. In Figure 57(a), PCC moduli for the south test pavements were higher than the north. Figure 57(b) and (c) show no clear differences in moduli among four subgroups with regard to the base and subbase layers. Figure 57(d) shows that the subgrade was relatively weak in the NW subgroup, and that the other subgroups all had similar subgrade moduli.

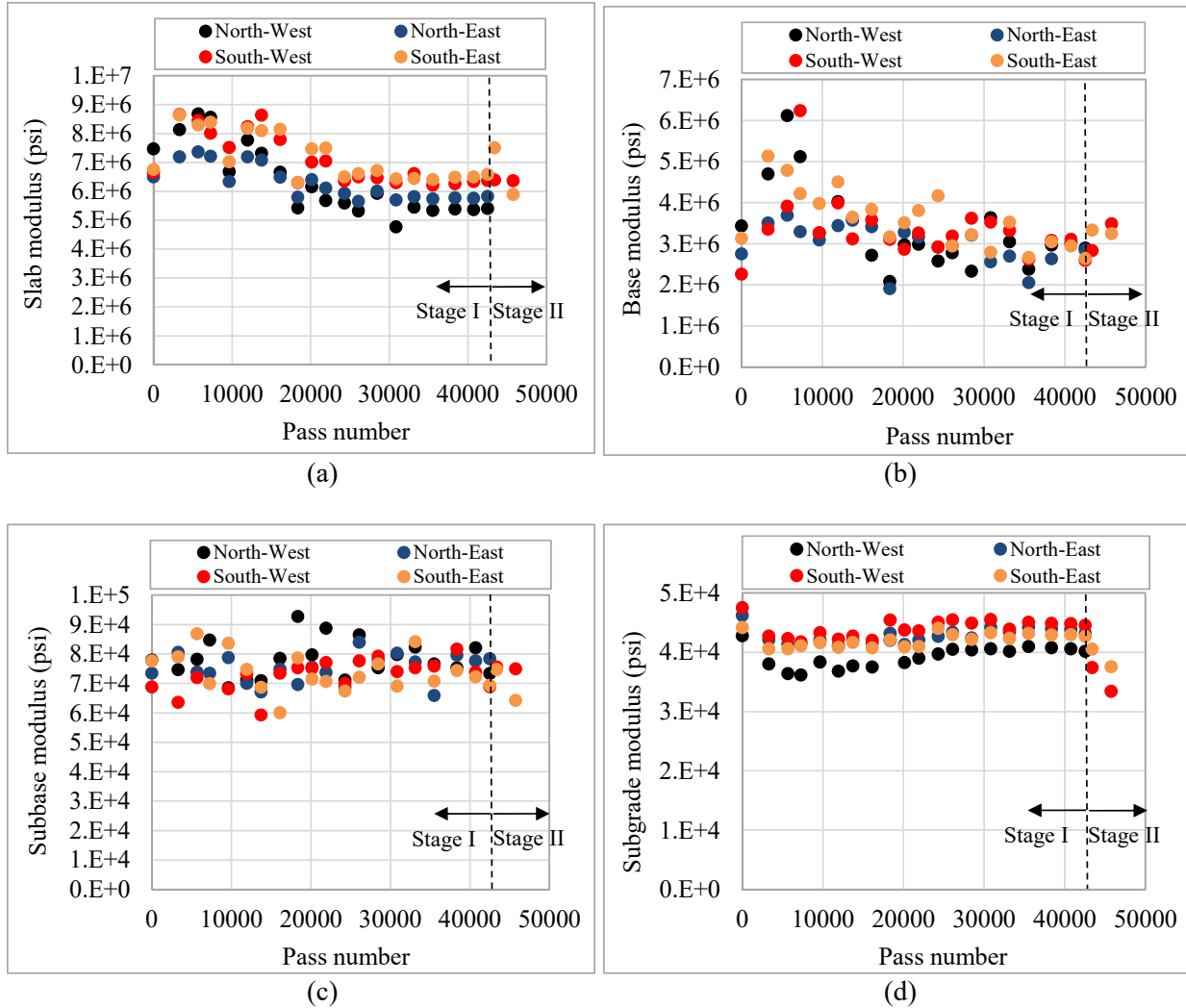


Figure 57. Backcalculated Moduli of Pavement Layers as a Function of Traffic: (a) P-501MR Concrete, (b) P-306MR Base, (c) P-154M Subbase, (d) P-152M Subgrade

6.2.2.2 CORNER DETERIORATION

Corner to Center Deflection Ratio

HWD tests were conducted weekly at the locations shown in Figure 10 (Section 3.2.2). For certain slabs, both center and corner locations were tested, and corner-to-center deflection ratios corresponding to the heaviest load (36,000 pounds) were calculated. Corners were assigned a three-character designation, as follows:

1st Character: Slab Identification Number

2nd Character: Test Pavement (N or S)

3rd Character: Corner Orientation (E or W)

For example, 2NE corresponds to the east corner of Slab 2 on the north side. The following corners were evaluated: 2NE, 3NW, 4NE, 5NW, 8NE, 9NW, 10NE, and 11NW (North); 2SE, 3SW, 4SE, 5SW, 8SE, 9SW, 10SE, and 11SW (South).

Figure 58(a)-(d) plot corner-to-center deflection ratios as a function of pass number for all four subgroups. As expected, the slabs with doweled contraction joints (NW and SW subgroups) generally exhibited lower corner-to-center deflection ratios than those with undoweled contraction joints (NE and SE subgroups). Furthermore, slabs in the NE and SE subgroups generally exhibited higher corner-to-center deflection ratios within the first 16,000 passes. Above 16,000 passes, corner-to-center deflection ratios decreased, presumably due to greater aggregate interlock caused by increasing temperatures.

At the end of Stage I, corner-to-center deflection ratios for the SE group ranged from 1.9 to 2.6 and from 1.4 to 1.8 on the NE group. Corner breaks occurred in all evaluated corners in the NE subgroup after only 3,300 passes. The severity of these corner breaks increased throughout the test. In the SE subgroup, only one low-severity (hairline) corner break was observed after approximately 17,800 passes. The crack density in slabs J4N, J5N, J10N, and J11N (i.e., slabs corner-to-center deflection ratios were reported for in the NE group) at the end of Stage I was 19%, 16%, 6% and 3%, respectively (table 9). For slabs J4S, J5S, J10S, and J11S (i.e., slabs corner-to-center deflection ratios were reported for in the SE group), the crack density at the end of Stage I was 1%, 0%, 3% and 4%, respectively (table 10). The terminal condition of these slabs as quantified by crack density was in agreement with the distress map shown in figure 49. Before the occurrence of corner break, slab corner moves up or down due to slab curling or warping triggered by slab temperature and moisture variation. After the occurrence of corner breaks, slab corner is no more a continuous part of a slab and thus, it is not supposed to move accordingly assuming that the structural integrity of foundation underneath slab corner remains unchanged. It indicates that temperature and moisture effect should be evident on SE slabs with least amount of corner breaks, while this effect should not be significant on NE slabs with broken corners. Therefore, the lower range of terminal corner-to-center deflection ratios for the NE subgroup compared to SE was consistent with the distresses in Stage I.

During Stage II, the corner-to-center deflection ratios increased in the SW and SE subgroups. A significant increase in the corner-to-center deflection ratios for SE corresponded to the appearance of two new corner breaks (on slabs J4S and J10S) and a decrease in the slab temperature of about

22 °F. In the SW subgroup, the corner-to-center deflection ratios were less than in the SE group, which is attributed to the higher restraint provided by doweled contraction joints.

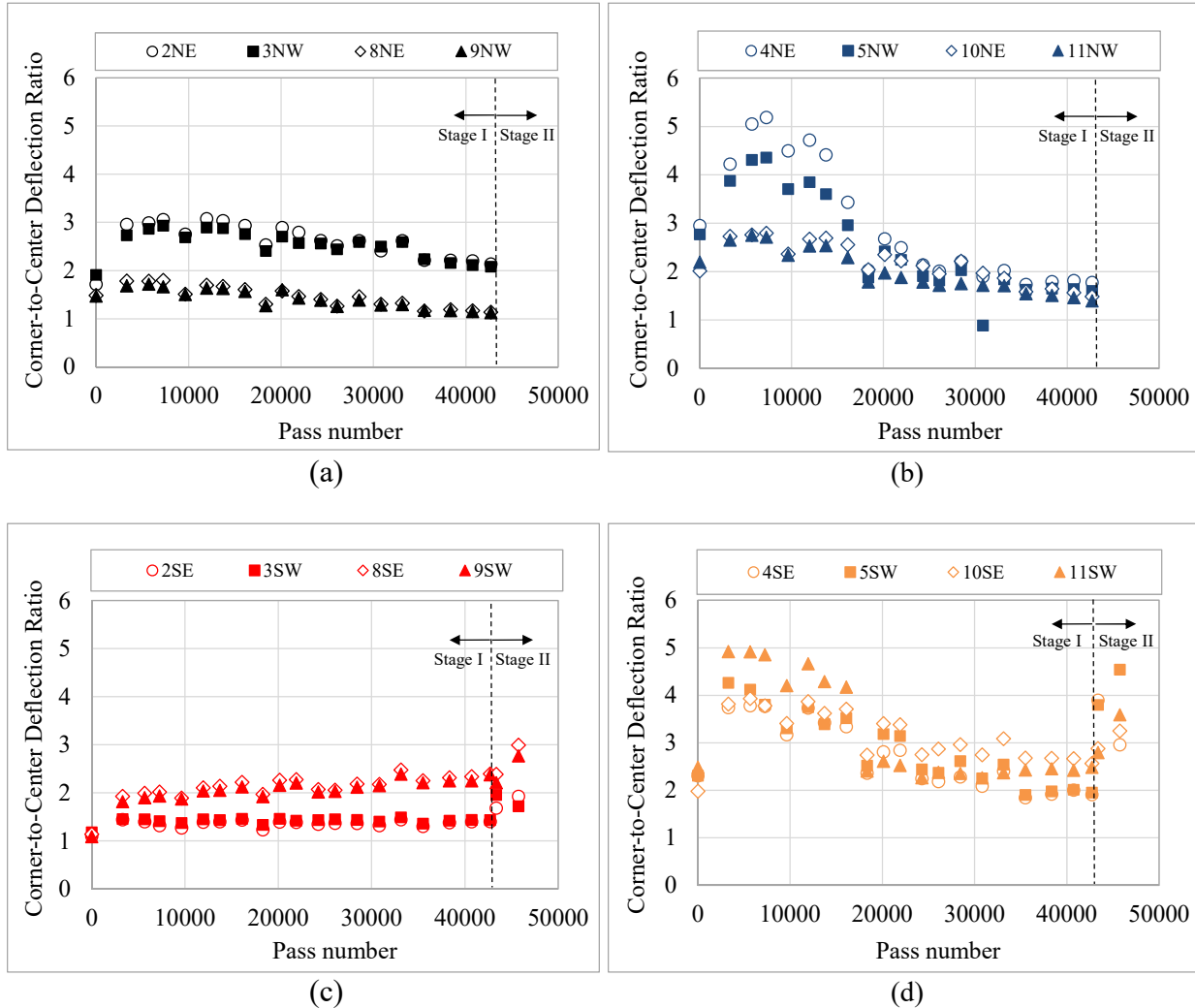


Figure 58. Corner-to-Center Deflection Ratios as a Function of Pass Number: (a) NW, (b) NE, (c) SW, (d) SE

Void Detection

Slab support conditions are often the key to the performance of rigid pavements. The occurrence of surface distresses such as corner breaks, joint faulting, and slab cracking can result from loss of support. Figure 59 shows an example of a plot of maximum corner deflection (D_0) versus HWD drop load, from corner 2NE in slab J2N. Intercept values greater than zero indicate the possible presence of voids.

Figure 60(a)-(d) show the intercept values (i.e., theoretical deflections at zero load) obtained from plots similar to figure 59 as a function of pass number for all four subgroups. The slab groups with undoweled contraction joints (NE and SE) had higher intercept values than the slab groups with doweled contraction joints (NW and SW). The loss of base support indicated by high intercept

values made these slab groups susceptible to corner breaks. Indeed, corner breaks developed in the majority of slabs in these two groups (i.e., J4N, J5N, J10N, and J11N in the NE subgroup and J4S, J10S, and J11S in the SE). Stage II saw an increase in deflection intercept values for both the SW and SE slab groups. Under heavy loads, the pavement foundation layers may have undergone permanent deformation, increasing the potential for voids (i.e., increasing intercept values). However, no corner breaks were observed in any slabs with doweled contraction joints.

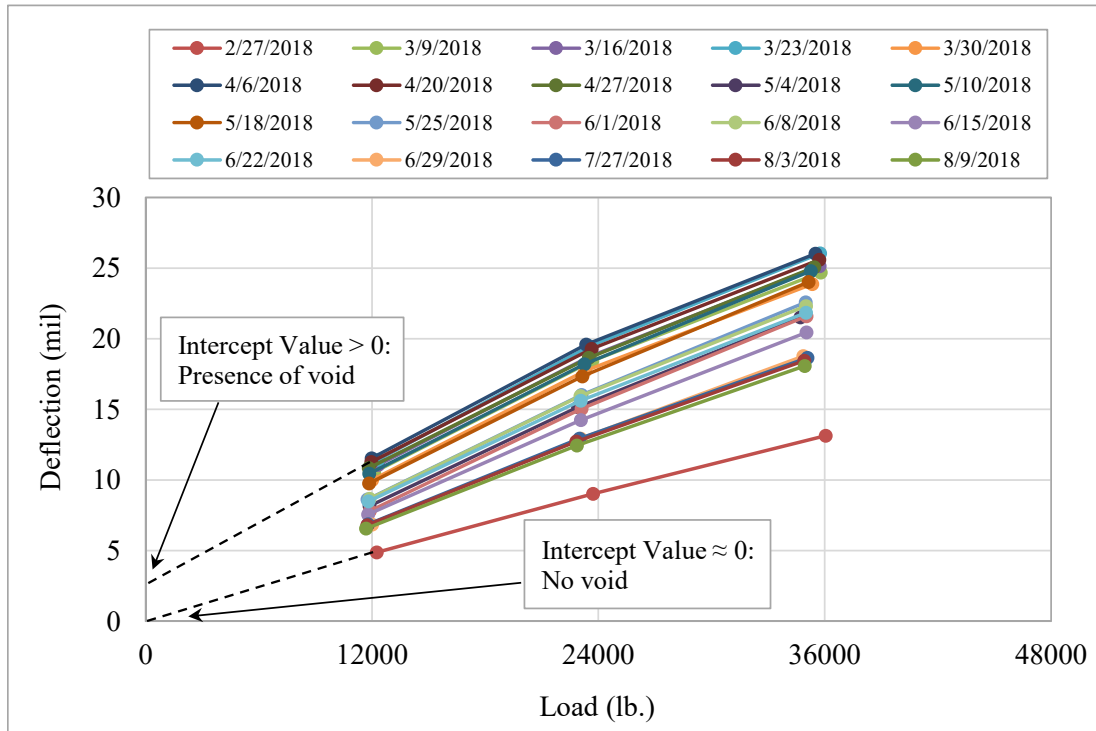


Figure 59. Example of Void Detection in Corner 2NE of Slab J2N

6.2.2.3 KEY FINDINGS

- The SE subgroup had the highest average ISM, and the NE subgroup the lowest. The low average ISM for NE corresponded to the high incidence of corner breaks in that subgroup.
- HWD backcalculation found higher values of PCC modulus for slab groups SW and SE, compared to NW and NE. PCC slabs on the south traffic lane generally had a higher backcalculated modulus than those on the north.
- Slabs in the NW and SW subgroups (those with doweled contraction joints) exhibited generally lower corner-to-center deflection ratios compared to slab groups with undoweled contraction joints. This result was expected due to the higher corner restraint provided by the dowel bar.
- Void detection analysis showed less loss of support at the slab corners for the NW and SW groups, compared to the NE and SE groups. Again, this result is attributed to the higher restraint provided by doweled transverse joints, reducing susceptibility to corner breaks.

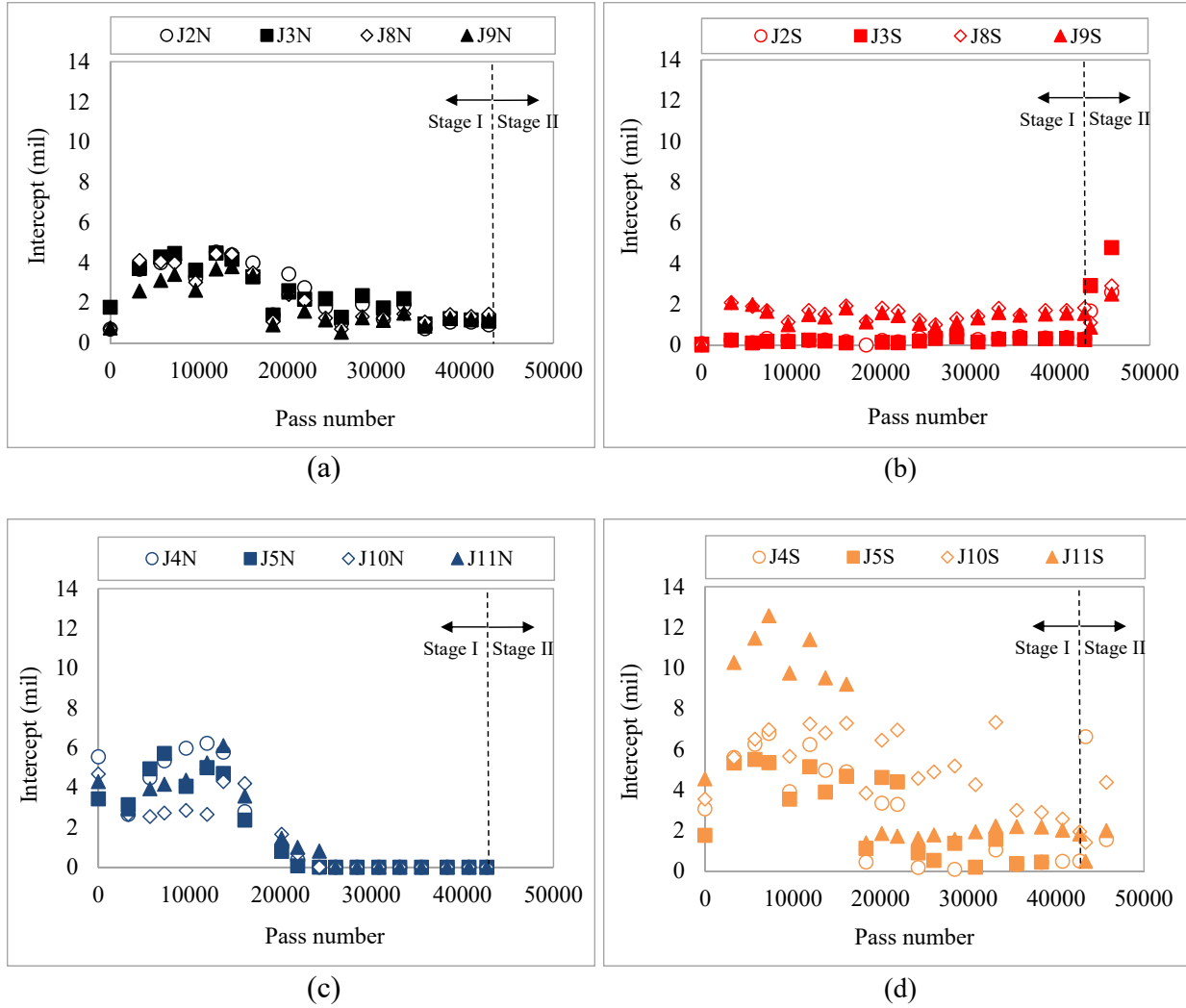


Figure 60. Intercept Values for Slab Groups as a Function of Pass Number: (a) NW, (b) SW, (c) NE, (d) SE

7. ADVANCED DATA ANALYSIS

7.1 FAILURE MECHANISM

The concrete distress types observed in the JCT included shrinkage cracks, corner breaks, and longitudinal cracks. Among these distress types, shrinkage cracking is a special case because it is non-structural and construction-related. Therefore, shrinkage cracks are excluded from the following discussion. In fact, corner breaks were the dominant structural distress in the JCT. Distress maps for Stage I and Stage II (figures 49-50) show a preponderance of corner breaks (and some diagonal cracks) in the NE and SE subgroups, in addition to one longitudinal crack on slab J4S. Typically, corner breaks initiate from the surface due to high surface tensile stress distributions acting at a distance from the wheel load. For top-down cracking, it is important to analyze the strain responses along both transverse and longitudinal joints, measured by the EGs at the top of the slab.

EGs near the slab surface at contraction joints experienced the highest tensile stresses when the wheel load was passing at a lateral offset from the EG location. This is in contrast to tensile stresses at the bottom gage, which are always maximum when the wheel is directly over the gage. Figure 61(a)-(d) show the strain distribution over gear tracks for all four slab groups. From Figure 61, Tracks (-4) and (+4) produced the maximum top tensile strains on the north and south test pavements, respectively. Figure 62(a)-(d) show the tensile strain distribution for EGs installed at the top of the slab along longitudinal construction joints. The maximum tensile strains in the NW and NE slab groups correspond to Tracks (0) and (-4), and the maximum tensile strains in the SW and SE slab groups correspond to Tracks (0) and (+4). The high top-of-slab tensile strains for track 0 (wheel directly on gage) are due to the strain reversal characteristic of longitudinal strains under moving loads.

Table 13 shows that maximum tensile strains at the slab surface along undoweled contraction joints (NE, SE) were higher than those along doweled contraction joints (NW, SW). Likewise, for construction joints, the tensile strains in groups with undoweled contraction joints (NE, SE) were higher than those in the groups with doweled contraction joints (NW, SW). This suggests higher susceptibility to corner breaks in slabs with undoweled contraction joints. Table 13 also reveals that surface tensile strains along keyed construction joints were small relative to doweled construction joints.

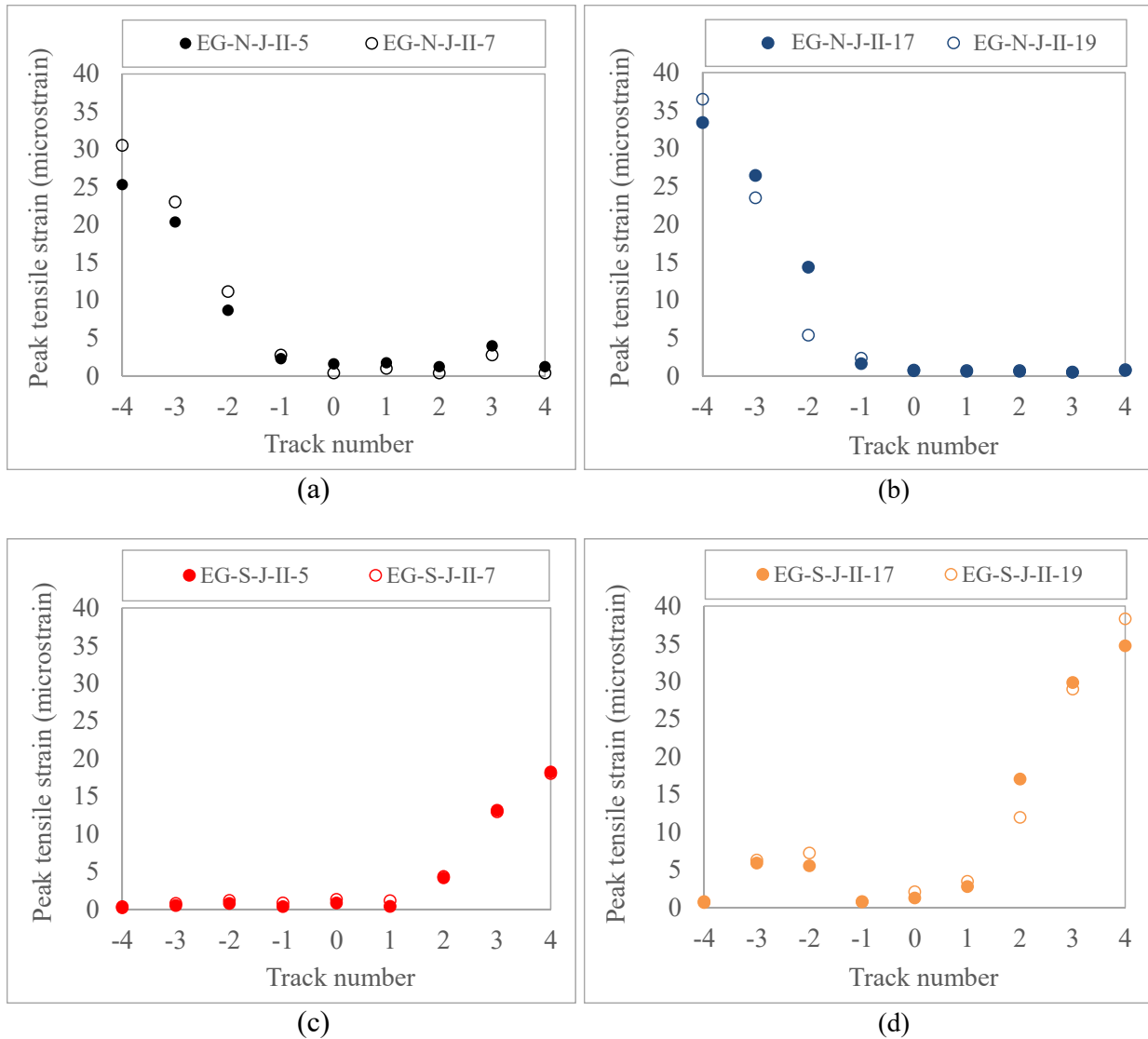


Figure 61. Peak Surface Tensile Strain as a Function of Gear Track Number, Transverse Contraction Joint (March 1, 2018): (a) NW, (b) NE, (c) SW, (d) SE

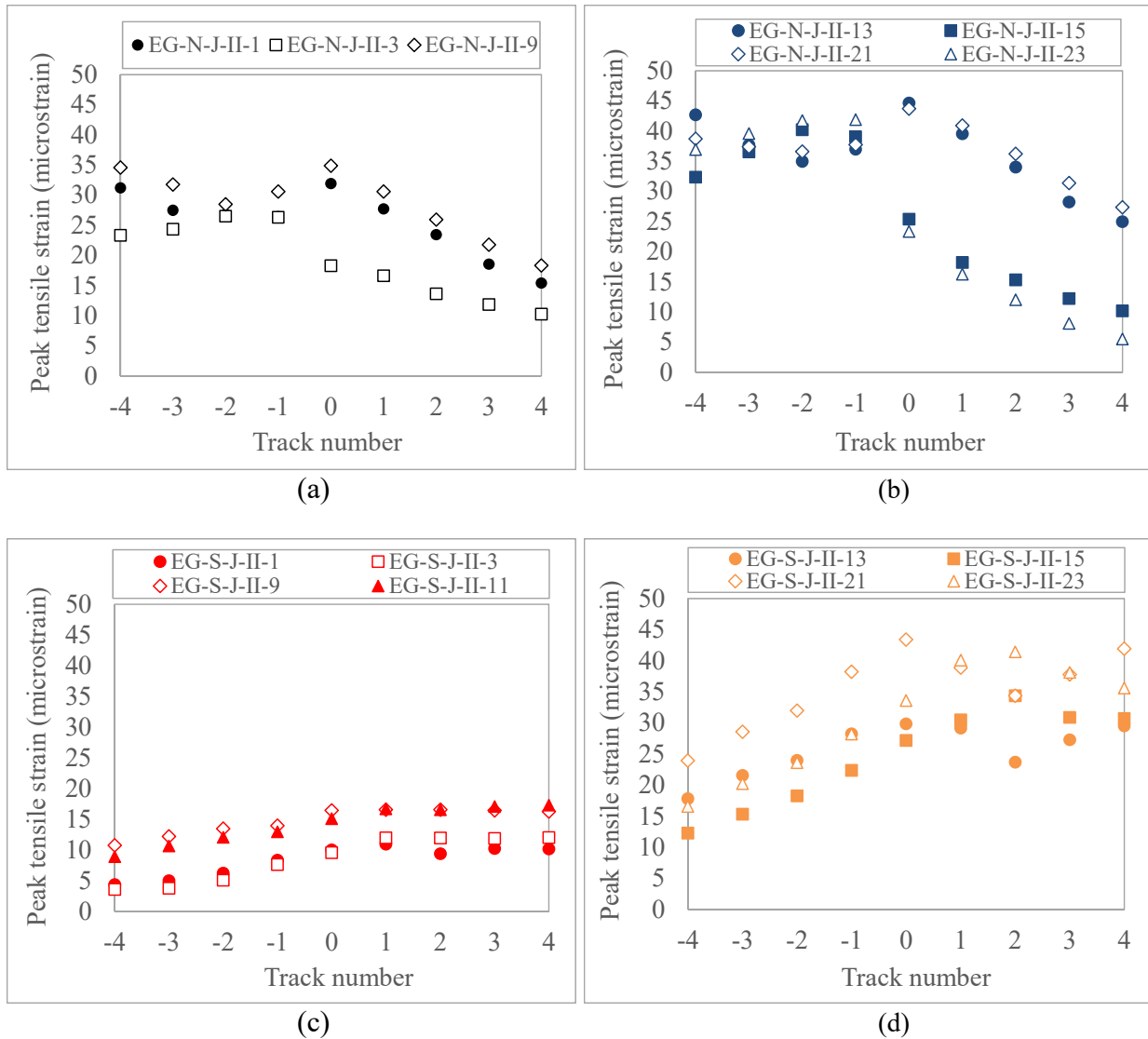


Figure 62. Peak Surface Tensile Strain as a Function of Gear Track Number, Longitudinal Construction Joint (March 1, 2018): (a) NW, (b) NE, (c) SW, (d) SE

Table 13. Summary of Maximum Surface Tensile Strains during the First Wander Sequence

Slab Group	Joint Type	Slab Pair	Sensor ID	Strain (microstrain)
North-West	Transverse	J2N-J3N	EG-N-J-II-5	25
			EG-N-J-II-7	31
North-East	Transverse	J4N-J5N	EG-N-J-II-17	33
			EG-N-J-II-19	36
South-West	Transverse	J2S-J3S	EG-S-J-II-5	18
			EG-S-J-II-7	18
South-East	Transverse	J4S-J5S	EG-S-J-II-17	35
			EG-S-J-II-19	38
North-West	Longitudinal	J2N-J8N	EG-N-J-II-1	32
			EG-N-J-II-3	27
		J3N-J9N	EG-N-J-II-9	35
			EG-N-J-II-11	-
North-East	Longitudinal	J4N-J10N	EG-N-J-II-13	45
			EG-N-J-II-15	40
		J5N-J11N	EG-N-J-II-21	44
			EG-N-J-II-23	42
South-West	Longitudinal	J2S-J8S	EG-S-J-II-1	10
			EG-S-J-II-3	12
		J3S-J9S	EG-S-J-II-9	16
			EG-S-J-II-11	17
South-East	Longitudinal	J4S-J10S	EG-S-J-II-13	30
			EG-S-J-II-15	34
		J5S-J11S	EG-S-J-II-21	43
			EG-S-J-II-23	41

Figure 63(a)-(d) show changes with traffic in the measured maximum tensile strains along contraction joints. During Stage I, there was no significant change on the SW subgroup, and relatively minor variations in the measured strain up to 30,000 passes on the NW subgroup. Stage II saw a significant increase in the strain in the SW subgroup due to increased loads. For the NE subgroup, which saw early corner breaks after 3,300 vehicle passes, there was a steep drop in maximum tensile strains (Figure 63(c)), which continued as the corner breaks increased in severity. For the SE subgroup, the consistency of the tensile strains in up to 30,000 passes (Figure 63(d)) is consistent with the absence of corner breaks. When corner breaks did develop in the SE slab group during Stage II, they probably were related to the sharp increase in tensile strains at the slab surface as seen in (Figure 63(d)).

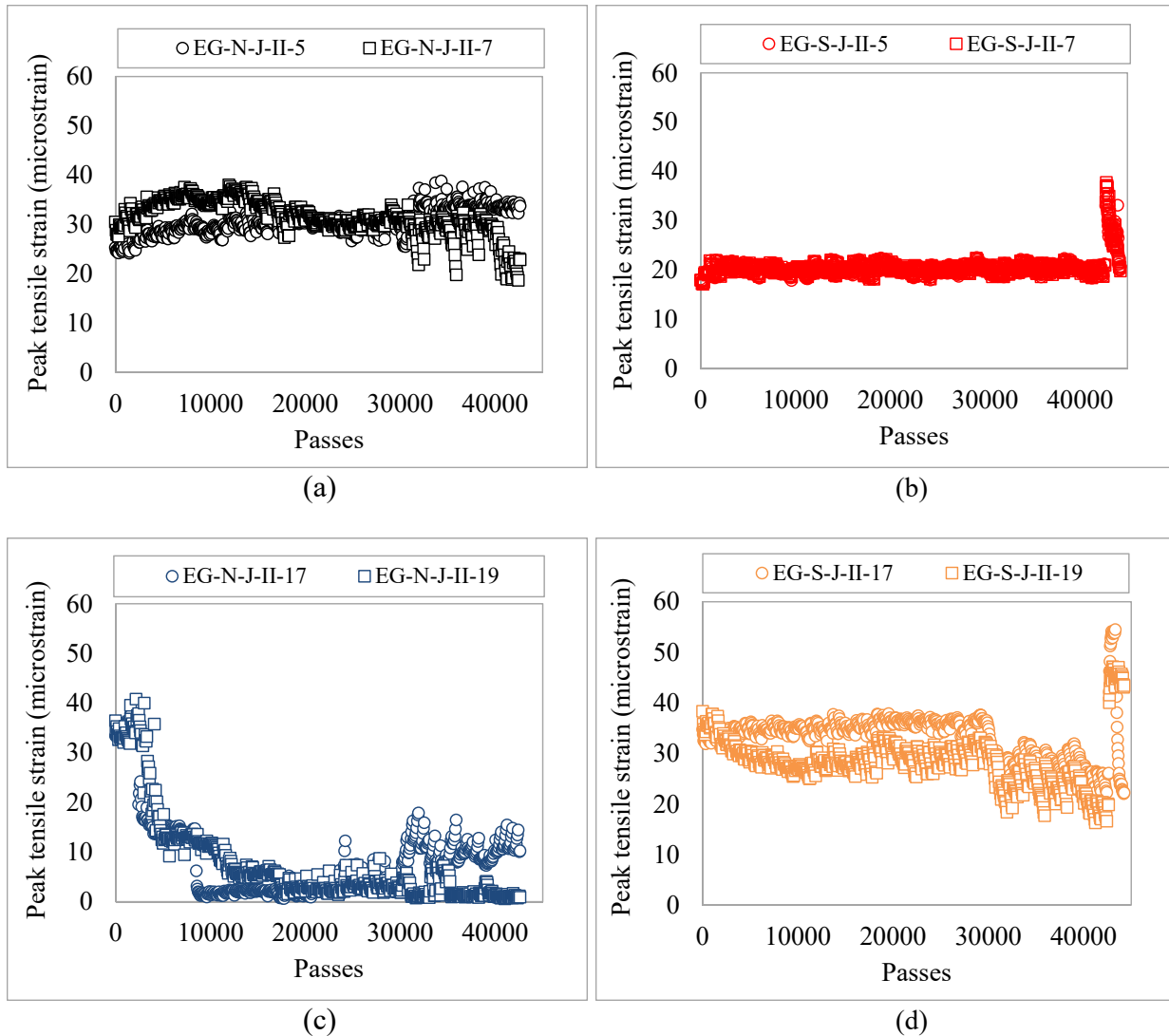


Figure 63. Maximum Surface Tensile Strain at Contraction Joints as a Function of Pass Number:
(a) NW, (b) SW, (c) NE, (d) SE

Most of the corner breaks were observed on undoweled contraction joints in the NE and SE subgroups. Therefore, these two subgroups were the focus of the analysis of tensile strains at the longitudinal joint. Figure 64(a)-(d) show changes with traffic in the measured maximum tensile strains along construction joints N 4-10, N 5-11, S 4-10, and S 5-11. Figure 64(a) and (b) indicate abrupt changes in measured tensile strain at approximately 3300 passes, clearly linked to the appearance of corner breaks in slabs J4N, J5N, J10N, and J11N (NE). In the SE subgroup, corner breaks were observed in slabs J4S and J10S during Stage II. The large increase in tensile strains along joint S 4-10 after pass 43,000 in Figure 64(c) reflects the appearance of corner breaks. Similarly, Figure 64(d) shows a sharp decrease in EG-S-J-II-23 maximum strain after approximately 16,700 passes. This was consistent with the appearance of a corner break in slab J11S.

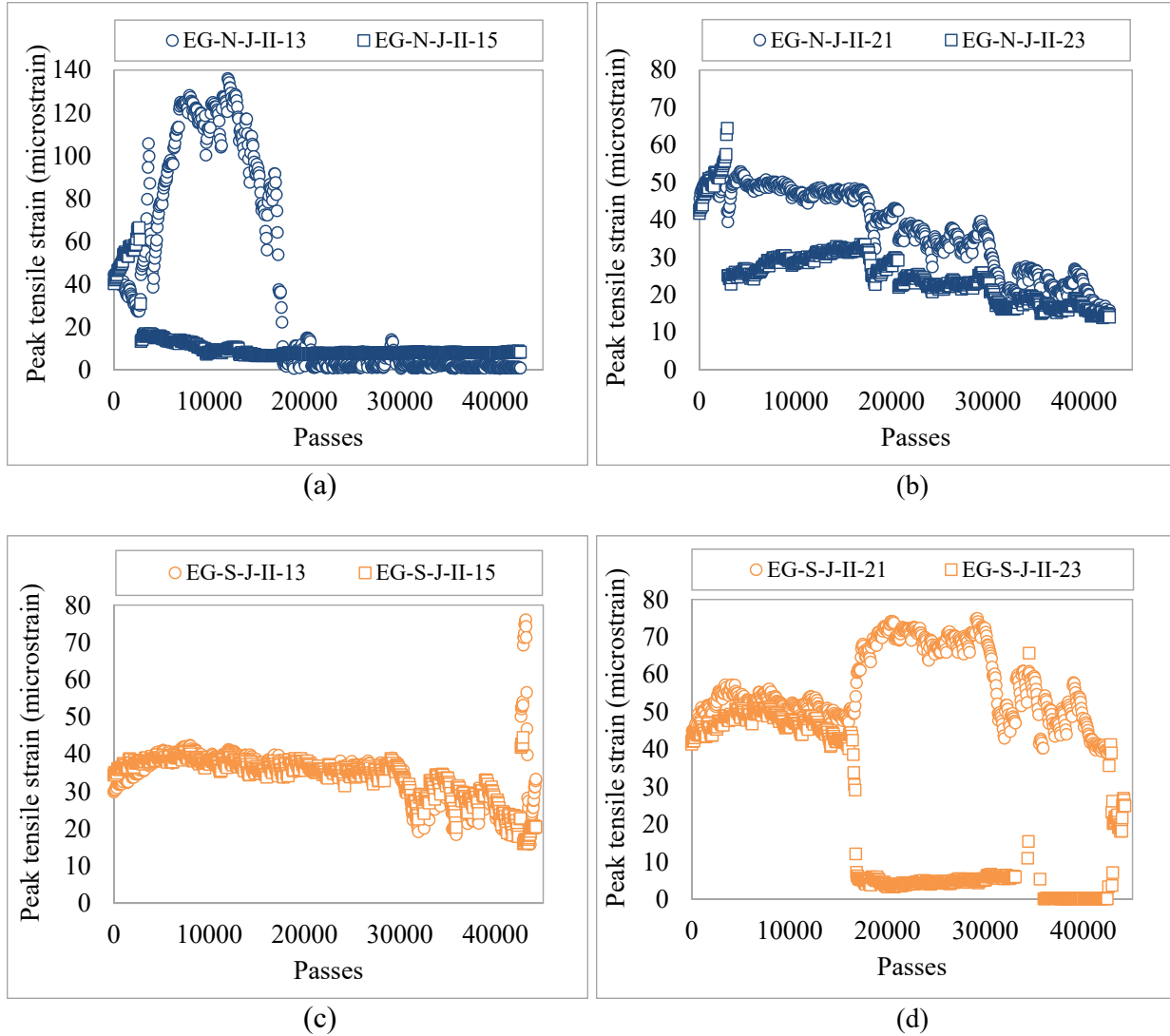


Figure 64. Change in Surface Tensile Strain With Traffic along Construction Joints: (a) N 4-10, NE, (b) N 5-11, NE, (c) S 4-10, SE, (d) S 5-11, SE

ECS (section 2.3) measured slab corner deflections relative to the base. A large deflection under the load usually indicates a gap or void under the corner, which can contribute to corner breaks. Figure 65(a)-(d) show the change in maximum ECS deflections for all four slab groups. The monitored corners of slabs J2N and J9N (NW) and slabs J2S and J9S (SW) exhibited little vertical movement compared to slabs J5N and J10N (NE) and J5S and J10S (SE), and any loss of slab support was minimal. Referring to Figure 65(c) and (d), the NE and SE slab corners exhibited higher absolute vertical movement, and higher variability of maximum deflection, than did the NW and SW groups. In Figure 65(c) after approximately 3,300 passes, the maximum corner deflection under load dropped to nearly zero, which was consistent with the appearance of corner breaks on Slabs J5N and J10N.

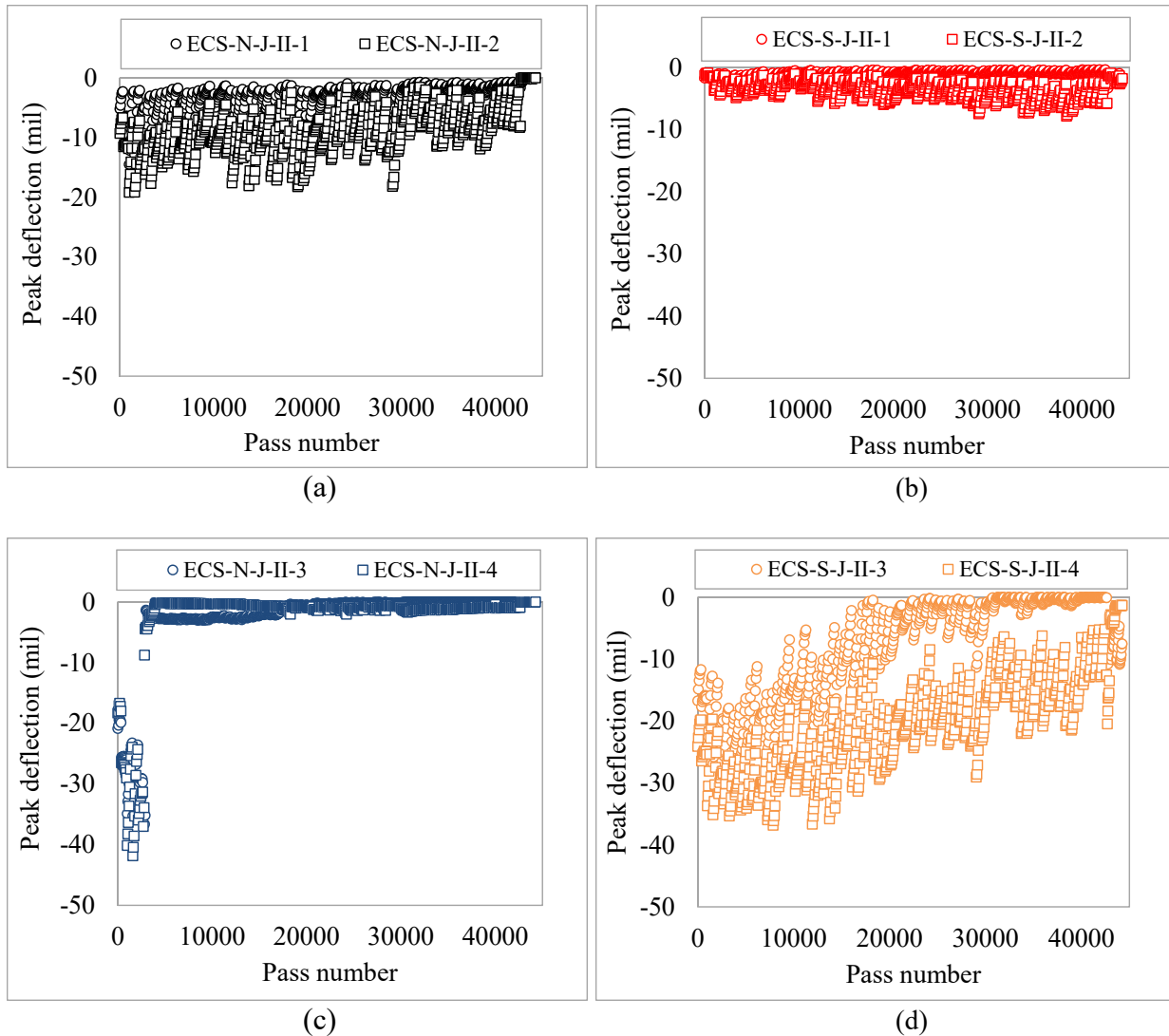


Figure 65. ECS Deflections: (a) NW, (b) SW, (c) NE, (d) SE

7.2 DESIGN CONSIDERATIONS

7.2.1 PAVEMENT DETERIORATION VERSUS JOINT PERFORMANCE

Brill and Yin (2018) analyzed the Cumulative Damage Factor (CDF) for a traffic test at the NAPTF, where the total traffic consisted of various wheel loads and gear configurations (12). For such a case, it is necessary to convert the number of vehicle passes or coverages under each gear type/wheel load combination to an equivalent number coverages at a reference gear type and load level. Applying this method to the JCT, the number of Stage II coverages (3D gear, 70,000 lbs. wheel load) was converted to a reference condition corresponding to Stage I (D gear, 65,000 lbs. wheel load). The conversion procedure can be found in reference (13). Figure 66 plots the SCI against the number of (actual) coverages for all four subgroups. Figure 67 plots SCI for the SW and SE slab subgroups against the actual and equivalent (adjusted to the reference condition) number of coverages for Stage II.

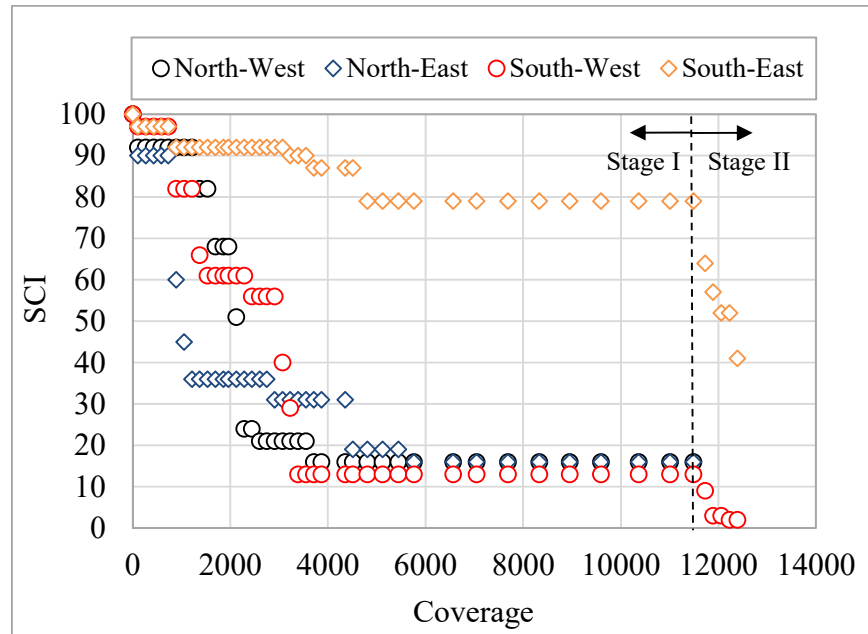


Figure 66. SCI Versus Coverages (unadjusted)

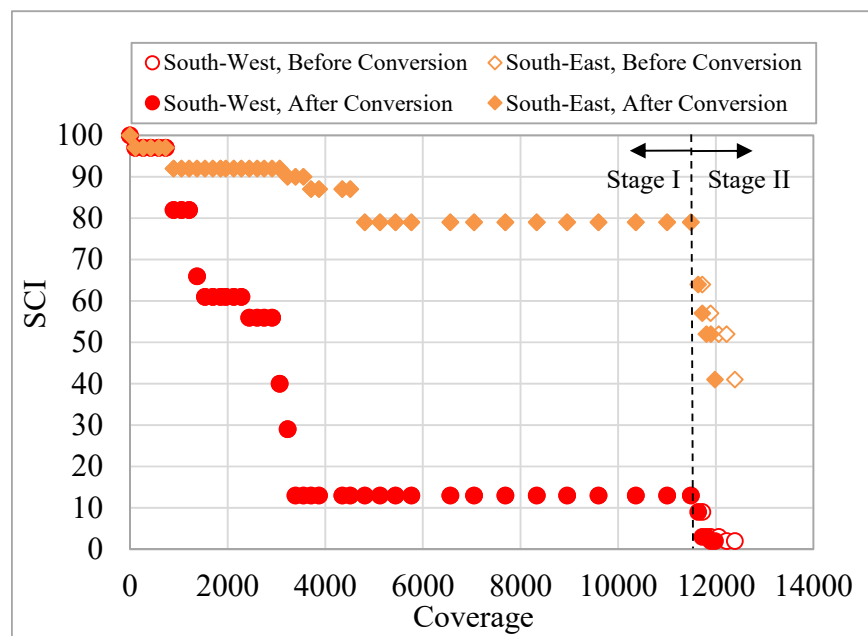


Figure 67. SCI Versus Coverages (South Traffic Lane, Stage II Data Adjusted to Reference Conditions)

Figure 68 regresses the SCI over the number of equivalent coverages (adjusted to the reference condition) to compare the fatigue performance of four slab groups. Based on Figure 68 data, the following parameters were determined and summarized in Table 14: (a) number of coverages to first appearance of thorough crack on the pavement surface, C_0 ; (b) number of coverages to failure,

C_F , which corresponds to $SCI = 80$; and (c) SCI deterioration rate. These parameters are as defined originally by Rollings in 1988 (14).

Table 14. Summary of Fatigue Data for Four Slab Groups

Slab Group	C_0	C_F	SCI Deterioration Rate
NW	386	753	-30
SW	435	840	-30
NE	138	351	-21
SE	673	5012	-10

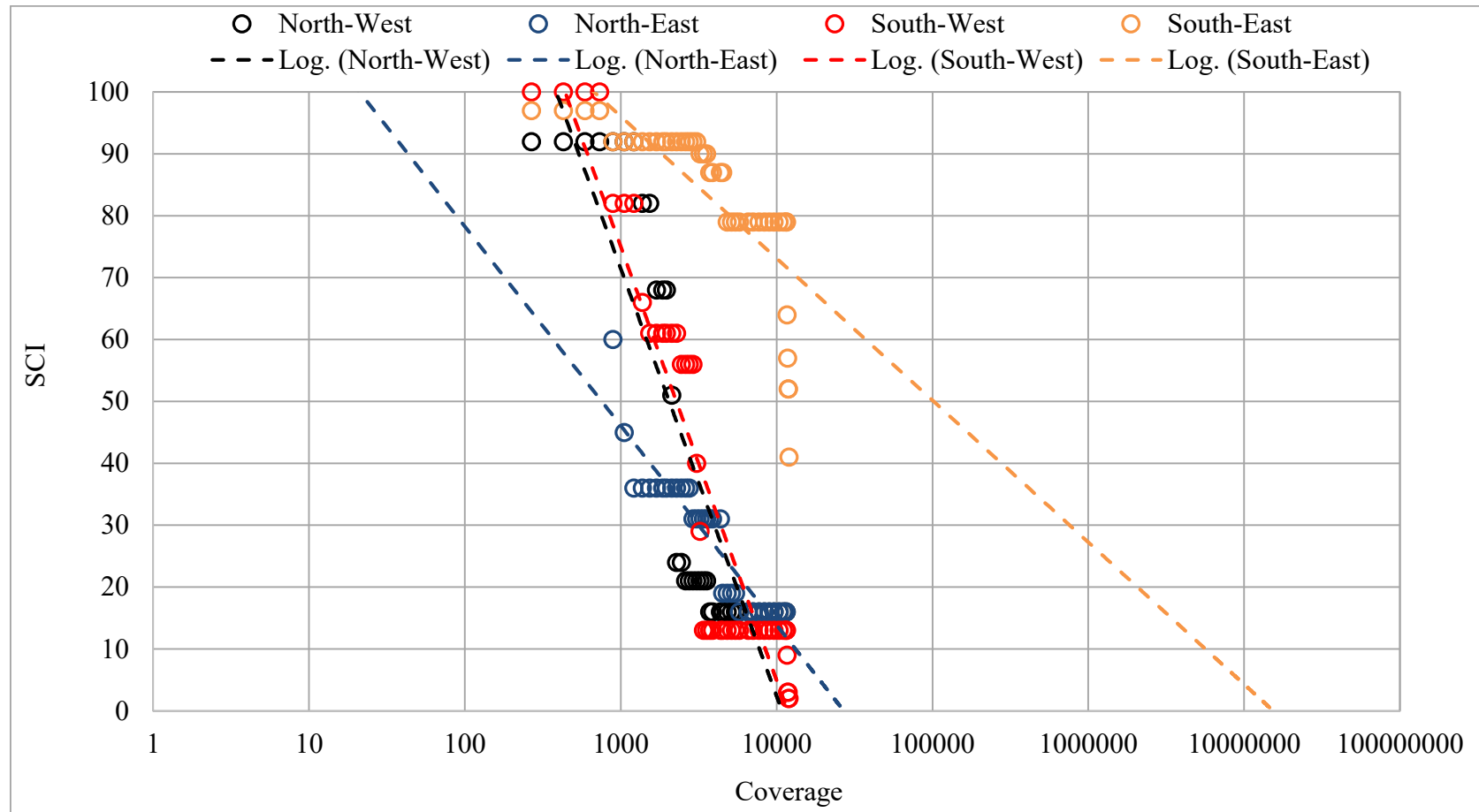


Figure 68. Comparison of Fatigue Life Among Slab Groups

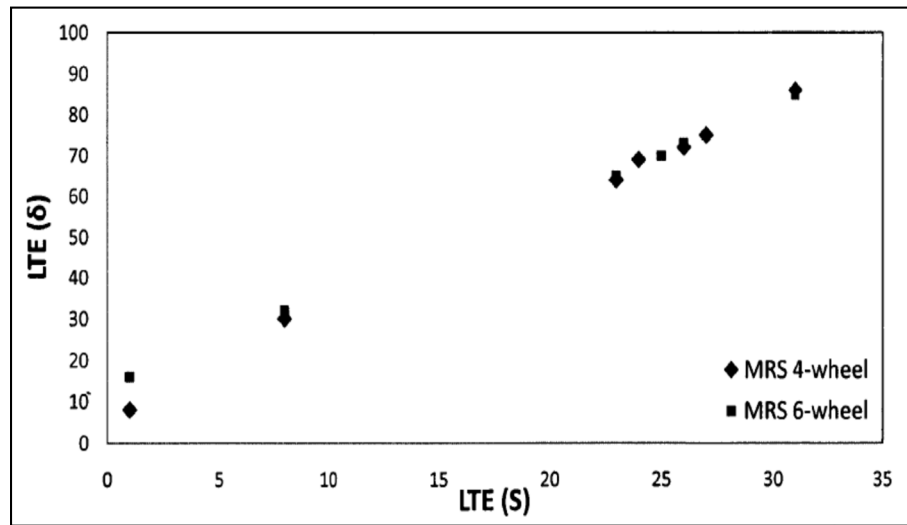
7.2.2 JOINT PERFORMANCE INDICATORS

7.2.2.1 LOAD TRANSFER (LT) - LOAD TRANSFER EFFICIENCY (LTE) CORRELATION

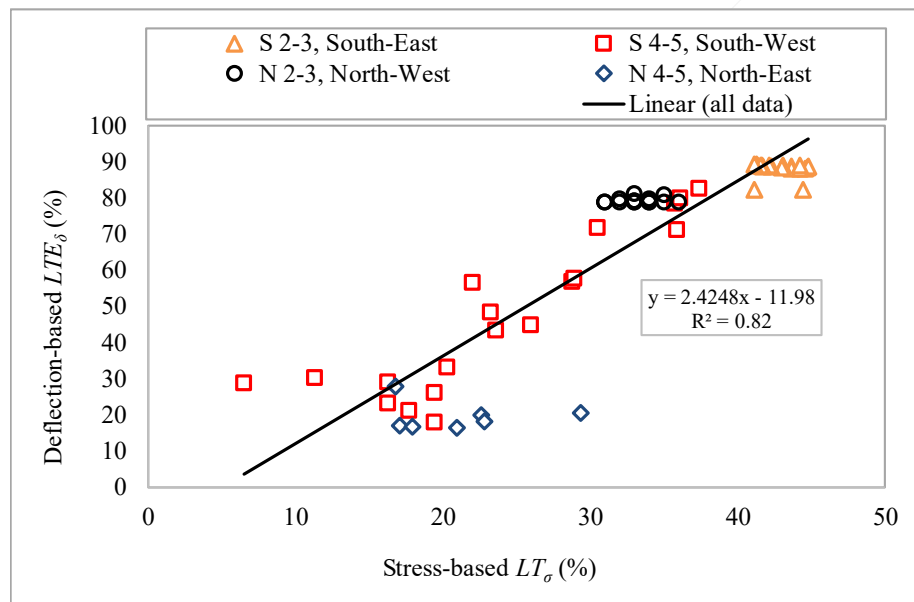
In this study, values of LT_{σ} were derived from EG responses, which are rarely available in the field. It is of interest to investigate possible correlations between LTE_{δ} and LT_{σ} so that load transfer values based on the actual joint performance can be estimated for design purposes.

In 2010, Wadkar conducted a study on the load transfer capacity of joints based on data from the NAPTF CC2 full-scale test (15). A 2D Finite Element (FE) model of the CC2 pavement was developed using the JSLAB software. The model was used to simulate pavement responses under 2D and 3D gear loads. Both LTE_{δ} and LTE_{σ} were estimated from the simulated responses. Figure 69(a) shows the correlation between LTE_{δ} and LTE_{σ} reported by Wadkar (15). Under both gear configurations, the correlation between LTE_{δ} and LTE_{σ} was positive. In Figure 69(b), CC8 JCT data was used to generate a similar correlation for the D gear. Both data sets show a similar positive correlation. Differences between the two figures are attributed to the following factors:

- The pavements cross-sections were different in CC2 and CC8.
- All contraction and construction joints in the CC2 test pavement were doweled, while four different types of contraction and construction joints were used in CC8.
- The CC2 simulation assumed equal PCC moduli for both loaded and unloaded slabs (15). For CC8, the calculation uses individual field PCC moduli of loaded and unloaded slabs derived from PSPA data.
- The gear configuration was different in CC2 and CC8. In CC2 the test pavements were trafficked with 2D and 3D gears. In CC8, a D gear was used for Stage I, and 3D for Stage-II on the south pavement only.
- Linear elasticity of PCC slabs was assumed for the CC2 simulation (15). However, the surface distresses observed in CC8 near the EG locations may have introduced non-linearity in the computation of stress-based LT_{σ} .



(a)



(b)

Figure 69. Correlation between LTE_{δ} and LTE_{σ} : (a) Wadkar, 2010 (15), (b) CC8 Phase II Joint Comparison Data

7.2.2.2 CORRELATION OF LOAD TRANSFER AND JOINT STIFFNESS

Joint Stiffness (k_j) can be determined for contraction and construction joints by empirical correlations with measured LTE_δ . In FAARFIELD, a value of $LT_\sigma = 25\%$ based on free edge stress is the design value. An effort was made to find a robust correlation between LT_σ and k_j that can be implemented in the rigid pavement design procedure.

Deflection-based LTE_δ and Joint Stiffness

Equation (4) is practical for estimating k_j from HWD tests but cannot be adopted directly to the development of a correlation between LT_σ and k_j . Equations (5) – (7) in Section 5.1.3 were evaluated as potential models, by comparing measured with predicted LTE_δ values from all three equations. The inputs for Equations (5) – (7) include modulus of subgrade reaction (k), wheel load radius, and radius of relative stiffness (l). A field-measured average value of $k=175$ pci was assumed for CC8. Figure 70 shows the comparisons for contraction (figure 70(a)) and construction joints (figure 70(b)). Figure 70(c) plots the LTE_δ values from contraction and construction joints on one chart. No significant differences were observed between transverse and longitudinal joints. Therefore, the subsequent analysis combined the data from transverse and longitudinal joints.

Stress-based LT_σ and Joint Stiffness

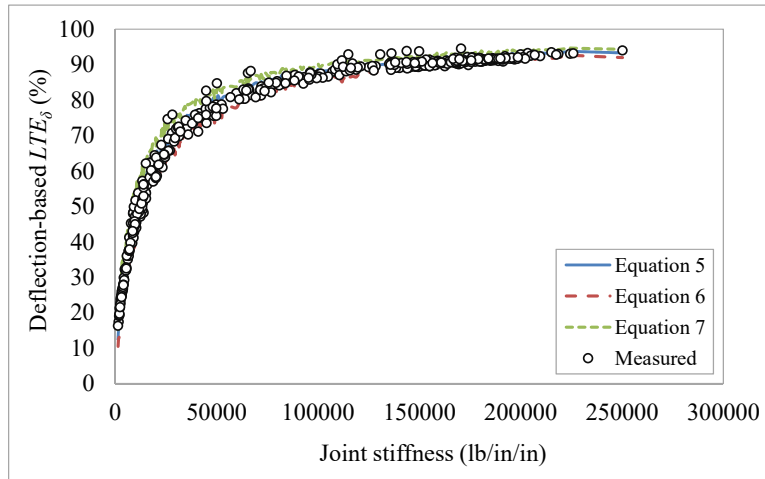
The first step in developing the correlation between LT_σ and k_j , was to identify and remove abnormal EG readings from the data set, in particular those associated with local slab damage. For example, Figure 71 shows the EG data used to determine the LT_σ across longitudinal joint S 5-11. As marked by the dashed red line, there was a large increase in peak strain on the loaded slab after approximately 17,000 passes, which clearly corresponded to the appearance of a corner break near the sensor location. Therefore, all data beyond 17,000 passes were considered unreliable and excluded from the analysis. The same data exclusion principle was followed for every joint.

Equations (5) to (7) were reformulated in terms of stress-based load transfer. Equations (12) to (14) are similar to Equations (5) to (7), except that the LTE_δ variable has been replaced by LT_σ , and the models are presented in a generalized form (i.e., no values are assigned to regression constants a , b , and c).

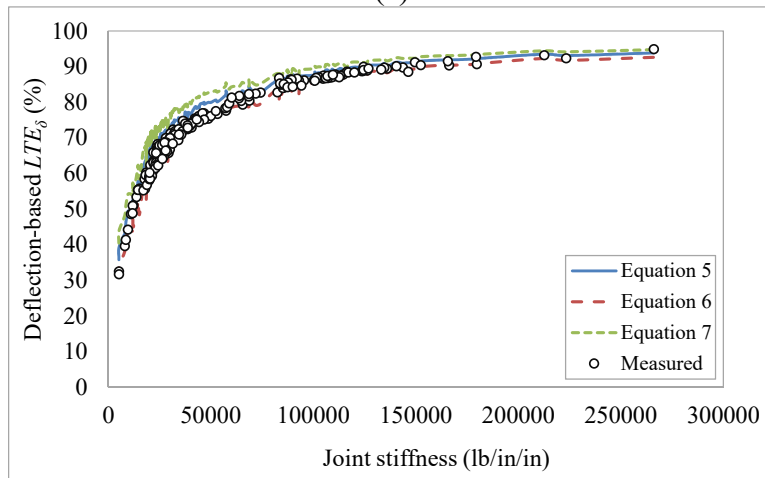
$$LT_\sigma = \frac{1}{1 + \log^{-1} \left[\frac{a - b \left(\frac{\epsilon}{\ell} \right) - \log(f)}{c} \right]} \quad (12)$$

$$\log(f) = \left[a \left(\frac{\epsilon}{\ell} \right) - b \right] \log \left(\frac{1}{LT_\sigma} - 1 \right) + c \quad (13)$$

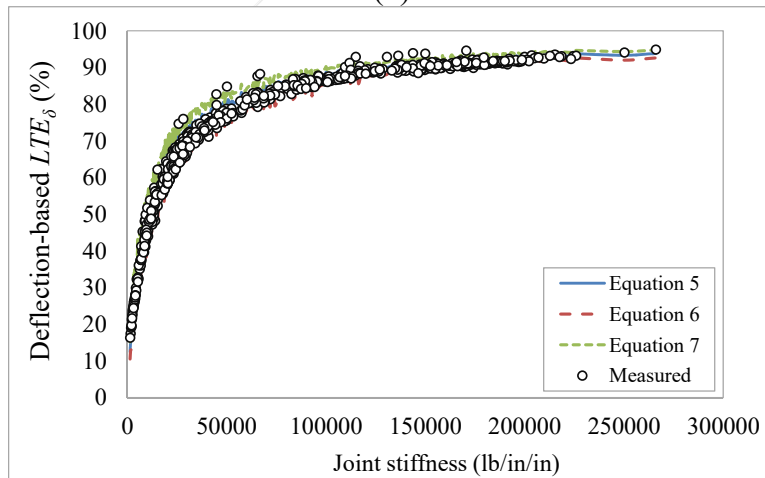
$$LT_\sigma = \frac{100\%}{1 + a \left(\frac{AGG_{tot}}{k\ell} \right)^{-b}} \quad (14)$$



(a)



(b)



(c)

Figure 70. Comparison between Measured and Predicted LTE_{δ} : (a) Contraction Joints Only, (a) Construction Joints Only, (c) Contraction and Construction Joints

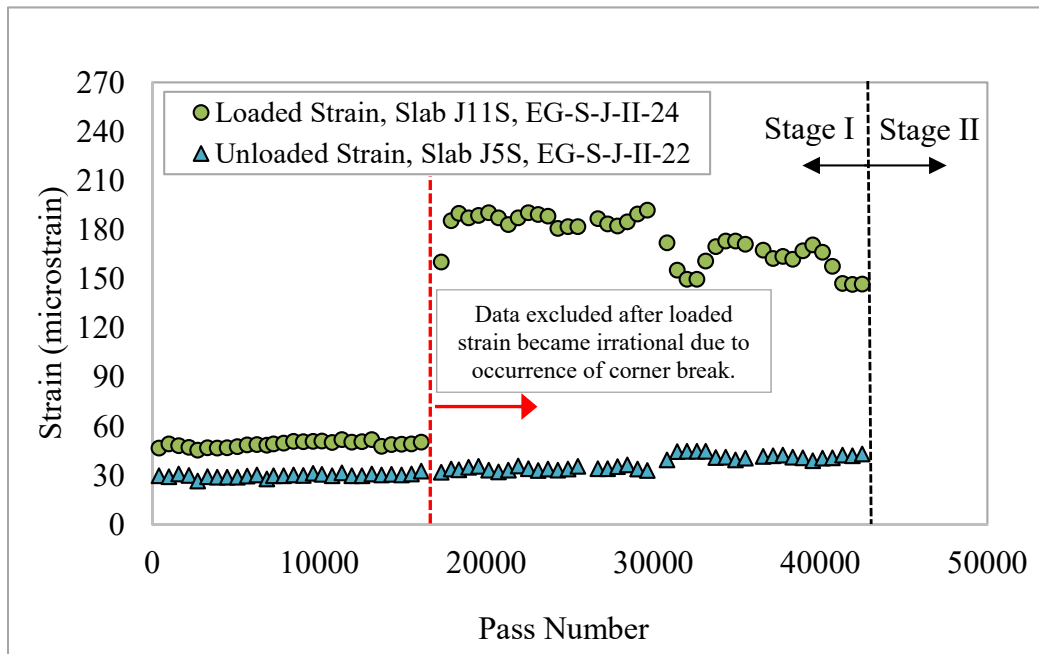


Figure 71. Loaded and Unloaded Strains used to Determine LT_{σ} of Longitudinal Joint S 5-11

where,

$$f = q_0 / k\ell;$$

q_0 = joint stiffness, lbs./in./in;

ε = wheel load radius, inches;

ℓ = radius of relative stiffness, inches;

k = modulus of subgrade reaction, pci; and

AGG_{tot} = total joint stiffness, lbs./in./in.

Table 15 summarizes the regression constants for each equation. In Figure 722, the predicted LT_{σ} values using Equations (13) and (14) matched the measured values reasonably well, and Equation (12) less so. Equation (14) was chosen for subsequent analysis due to its relative simplicity (only two regression constants).

Table 15. Regression Constants for Equation 11, 12, and 13

Constant	Equation 11	Equation 12	Equation 13
a	0.34	6	3.4
b	-13	4.5	-0.29
c	6	1.8	---

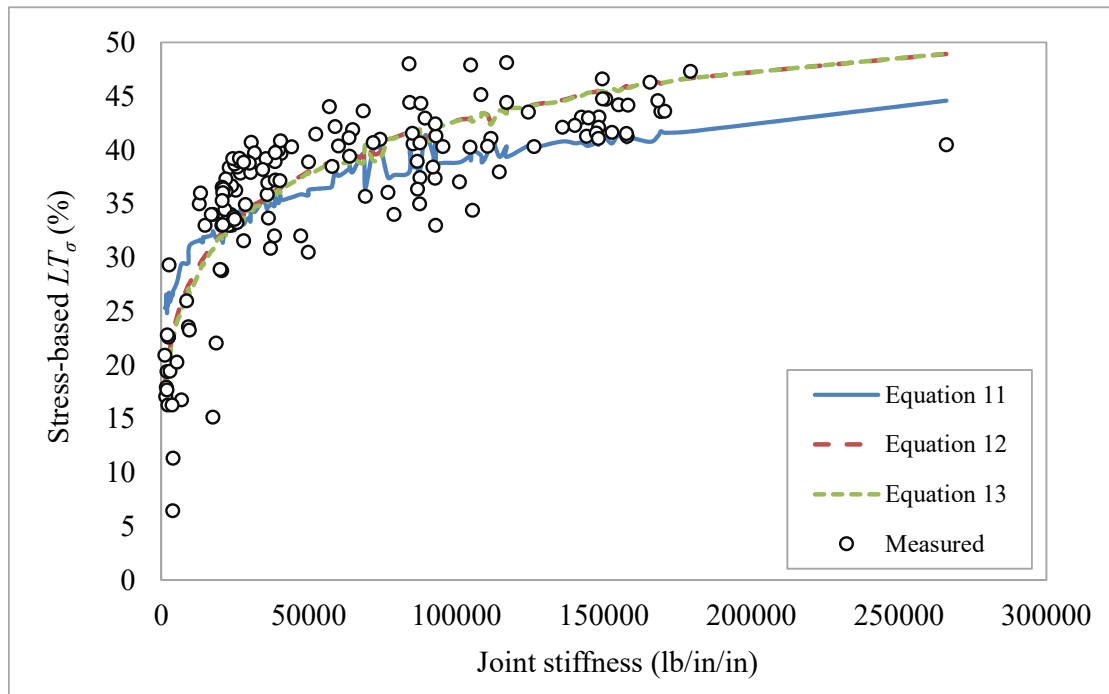
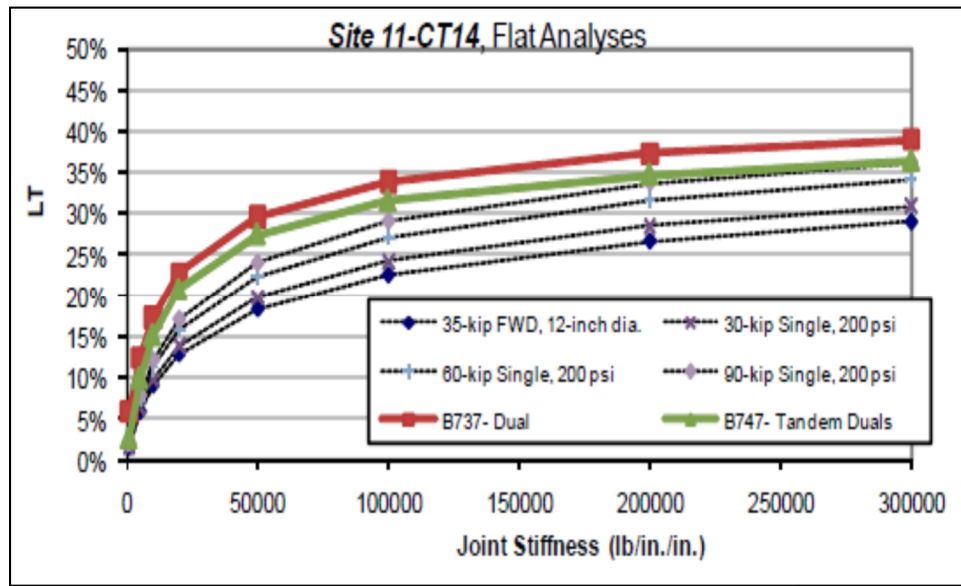


Figure 72. Stress-based LT_{σ} Predictive Models as Function of Joint Stiffness

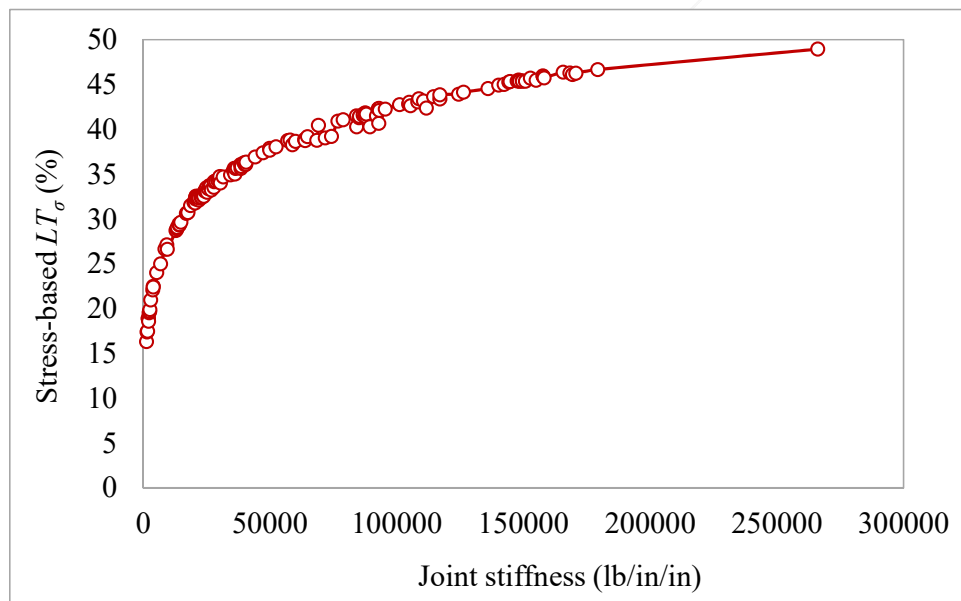
In 2011, Byrum et al. proposed a series of correlations between LT_{σ} and k_j (5). A selected pavement section of Denver International Airport was modeled using the ILSL2-Finite Element computer program developed by Ioannides and Khazanovich in 1998 (16). In this model, a 25 feet long slab with a modulus $E=4,900$ ksi was placed on top of a subgrade with $k=200$ pci. A series of simulations were conducted under various load levels and gear configurations to determine pavement responses. These responses were then used to determine LT_{σ} and k_j . Figure 73(a) shows the correlations between LT_{σ} and k_j reported by Byrum et al. Figure 73(b) shows the correlation between LT_{σ} and k_j using instrumentation data from CC8 JCT (the model corresponding to Equation 13 in Figure 72). Similar to the correlations reported by Byrum et al., a nonlinear trend is observed with an LT_{σ} value up to 50% corresponding to a maximum k_j of 266,072 lbs./in/in.

Comparison between Joint Types

The previous section correlated LT_{σ} to k_j by combining the measured values from all four joint types. Figure 74 shows trends of measured LT_{σ} vs. k_j for each of the four joint types: doweled contraction, undoweled contraction, doweled construction, and sinusoidal keyed construction joints.



(a)



(b)

Figure 73. Correlation between LT_{σ} and k_j : (a) Byrum et al., 2011 (5), (b) Proposed from CC8 Phase II Joint Comparison Test

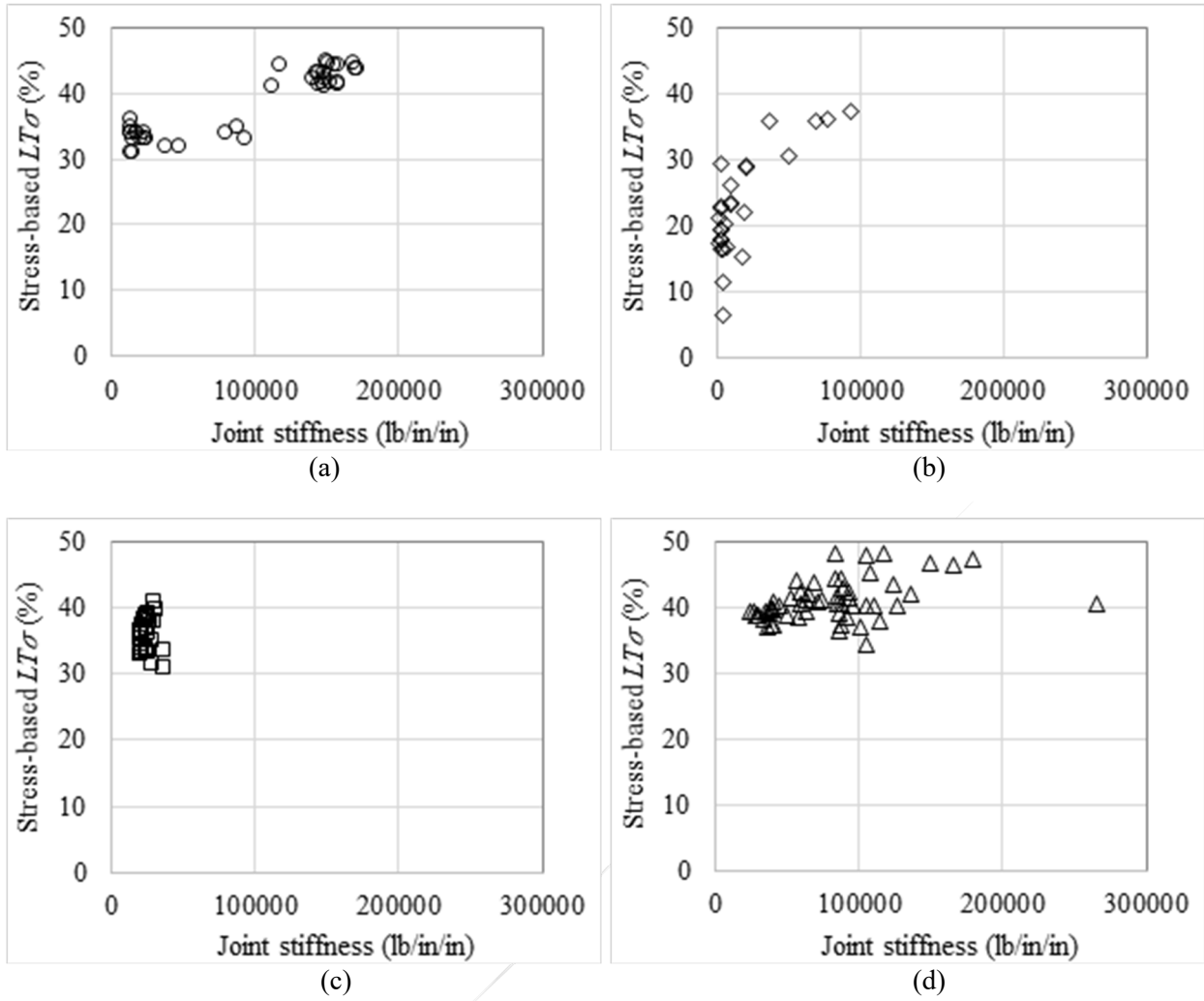


Figure 74. Trends of $LT\sigma$ vs. k_j for four joint types: (a) Doweled contraction joint, (b) Undoweled contraction joint, (c) Doweled construction joint, (d) Sinusoidal keyed construction joint

8. CONCLUSIONS AND RECOMMENDATIONS

8.1 CONCLUSIONS

8.1.1 PAVEMENT STRUCTURAL PERFORMANCE

- Corner breaks were the major structural distress type for the JCT. Most corner breaks developed at undoweled contraction joints.
- The NE slab subgroup (combination of undoweled contraction and doweled construction joints) exhibited the poorest structural performance among all slab groups.
- As measured by fatigue life, the SE slab subgroup (combination of undoweled contraction and sinusoidal keyed construction joints) outperformed the other three subgroups.
- Neither of the two tested construction joint types (sinusoidal keyed or doweled) demonstrated a clear structural performance benefit.

8.1.2 RELATION BETWEEN PAVEMENT CONDITION AND JOINT PERFORMANCE

- Doweled contraction joints exhibited no significant change in load transfer capacity over the course of the traffic test. An increase in apparent load transfer capacity for undoweled contraction joints was associated with enhanced aggregate interlock due to changes in slab temperature.
- Doweled and sinusoidal keyed longitudinal keyed construction joints exhibited generally equivalent performance. The load transfer capacity of both doweled and keyed construction joints degraded over the course of traffic. Doweled construction joints exhibited somewhat slower rates of deterioration and higher terminal LTE_{δ} values than did sinusoidal keyed joints.
- Subgroups with doweled contraction joints (NW and SW) exhibited generally better performance than the subgroups with dummy joints (NE and SE). Within the former subgroup, it was not possible to determine which of the two tested joint combinations – doweled contraction/doweled construction or doweled contraction/keyed construction - performed better.
- No definite correlation could be established between the performance of contraction joints and pavement structural condition (SCI). Doweled contraction joints can sustain good performance at SCI values less than 80. The performance of undoweled contraction joints was most sensitive to slab temperature, regardless of pavement condition.
- In contrast to contraction joints, construction joint performance degraded with SCI, but at a slow rate.

8.1.3 DESIGN CONSIDERATIONS

- CC8 test data indicated that load transfer was 30% or above for doweled contraction joints, and for doweled and sinusoidal keyed construction joints. This is significant because it assumes 25% edge stress transfer for design. Undoweled contraction joints were more variable, and exhibited edge stress transfer values less than 20% at low slab temperatures.

- It is possible to estimate in-situ edge stress transfer from HWD deflection data. Deflection-based LTE_{δ} was found to be reasonably well-correlated to stress-based LT_{σ} for contraction joints.
- Correlations between LTE_{δ} and k_j for both contraction and construction joints show that above $LTE_{\delta} = 90\%$ there is little variation of LTE_{δ} with respect to increases in joint stiffness. The 90% LTE_{δ} threshold value corresponds approximately to $k_j = 150,000$ lbs./in/in.
- Existing correlations in the literature between deflection-based LTE_{δ} and k_j were reformulated to develop a new stress-based $LT_{\sigma} - k_j$ correlation. The proposed correlation has potential to be implemented in the future rigid pavement design procedure.

8.2 RECOMMENDATIONS

- Further efforts should be directed to investigate the three-way interrelation of edge stress transfer, deflection-based load transfer efficiency, and joint stiffness.
- Post-traffic investigations should look for evidence of possible local damage that did not manifest at the pavement surface during the test phase.
- Considering the possible interference of Transition 2 with JCT subgroups SW and NW, it is recommended that future NAPTF rigid pavement tests should have longer transition areas.

9. REFERENCES

1. Federal Aviation Administration. AC 150/5320-6F, Airport Pavement Design and Evaluation, 2016.
2. Federal Aviation Administration. AC 150/5320-6E, Airport Pavement Design and Evaluation, 2009.
3. Brill, D. R. Field Verification of a 3D Finite Element Rigid Airport Pavement Model, Galaxy scientific Corporation, Grant No. DTFA030-95-D-00019, 2000.
4. Byrum C.R. et al. Joint Load Transfer in Concrete Airfield Pavements: Final Report. Innovative Pavement Research Foundation (IPRF) Project FAA-01-G-002-05-2, 2011.
5. Ioannides, A. M. and M. I. Hammons. (1996). Westergaard-Type Solution for Edge Load Transfer Problem. Transportation Research Record: Journal of the Transportation Research Board, 1996. 1525: 28-34.
6. Croveti, J.A. Design and Evaluation of Jointed Concrete Pavement Systems Incorporating Open-Graded Permeable Bases. Dissertation. University of Illinois at Urbana-Champaign, Champaign, IL, 1994.
7. ASTM. "Standard Test Method for Airport Pavement Condition Index Surveys," D5340-12, American Standard for Test and Materials, West Conshohocken, PA, 2012.

8. Stoffels, S., D. Morian, A. Ioannides, S. Wu, S. Sadasivam, L. Yeh and H. Yin, Improved Overlay Design Parameters for Concrete Airfield Pavements, Baseline Experiment Final Report, Innovative Pavement Research Foundation (IPRF) Project FAA-01-G-002-04-02, 2008.
9. Stoffels, S., D. Morian, A. Ioannides, L. Yeh, J. Reiter and S. Wu, Improved Overlay Design Parameters for Concrete Airfield Pavements—SCI Validation Study Research Report, Innovative Pavement Research Foundation (IPRF) Project FAA-01-G-002-06-03, 2010.
10. Lin, Y. Modified Mechanistic-Empirical Airfield Unbonded Concrete Overlay Traffic Prediction Model. Dissertation. The Pennsylvania State University, State College, PA, 2011.
11. Cary, C., M. Ahmed and H. Yin. Construction Cycle 8 Phase II Test Report. Gemini Technologies, Inc., Delivery Order 005: NAPTF Support, 2018.
12. Brill, D. R., and Yin, H. Full-Scale Tests of Aircraft Overloads on Airport Flexible Pavements. ASCE International Conference on Transportation and Development, 2018.
13. Yin, H. Construction Cycle 8 Test Report – Phase I. Gemini Technologies, Inc., Delivery Order 005: NAPTF Support, 2016.
14. Rollings, R.S., Design of Overlays for Rigid Airport Pavements, Report No. DOT/FAA/PM87/19, Federal Aviation Administration, Washington, D.C., 1988.
15. Wadkar, A. Study of Load Transfer Efficiency of Airfield Rigid Pavement Joints based on Stresses and Deflections. M.S. Thesis. The Rowan University, Glassboro, NJ, 2010.
16. Ioannides, A. M., and Khazanovich, L. Nonlinear Temperature Effects on Multi-Layered Concrete Pavements. Journal of Transportation Engineering, ASCE, 124(2), 128-136, 1998.